DOCTORAL THESIS

Development of CAE tools for fluid-structure interaction and erosion in turbomachinery virtual prototyping

Author:
Alessio CASTORRINI

Supervisor:
Prof. Alessandro CORSINI

Co-Supervisor:
Prof. Franco RISPOLI

*A thesis submitted in fulfillment of the requirements
for the degree of Doctor of Philosophy*

in

Industrial Production Engineering

February 21, 2017

"Alles, was tief ist, liebt die Maske"

Friedrich Nietzsche

SAPIENZA UNIVERSITY OF ROME

Abstract

Faculty of Civil and Industrial Engineering
Department of Mechanical and Aerospace Engineering

Doctor of Philosophy

Development of CAE tools for fluid-structure interaction and erosion in turbomachinery virtual prototyping

by Alessio CASTORRINI

The work presented in this thesis is based on the development of advanced computer aided engineering tools dedicated to multi-physics coupled problems. Starting from the state of the art of numerical tools used in virtual prototyping and testing of turbomachinery systems, we found two interesting and actual possible developments focused on the improved implementation of fluid-structure interaction and material wearing solvers. For both the topics we will present a brief overview with the contextualization on the industrial and research state of the art, the detailed description of mathematical models (Chapter 2), discretized (FEM) stabilized formulations, time integration schemes and coupling algorithms used in the implementation (Chapter 3). The second part of the thesis (Chapter 4-7) will report some application of the developed tools on some latest challenges in turbomachinery field as rain erosion and load control in wind turbines and non-linear aeroelasticity in large axial fans.

Acknowledgements

Contents

xii

List of Figures

List of Tables

List of Abbreviations

ALE	Arbitrary Lagrange-Euler
URANS	Unsteady Reynolds Averaged Navier-Stokes
DRD	Diffusion for Reaction Dominated Problem
DRDJ	Diffusion for Reaction Dominated Problem with Jump Factor
FE	Finite Element
FSI	Fluid Structure Interaction
GLS	Galerkin/least-squares
PCT	Particle cloud tracking
PDF	Probability density function
PSPG	Pressure-stabilizing/Petrov-Galerkin
SUPG	Streamline upwind/Petrov-Galerkin
TI	Turbulence intensity

Subscripts

f	Fluid
s	Solid
e	Element
n	Node number
sd	Spatial dimensions

Superscripts

h	Discretization characteristic length
n	Time step number

List of Symbols

Roman

a	Distance
$\mathbf{a}_c$	Particle cloud acceleration
c	Section cord
c_m	Rayleigh wave velocity
c_w	Speed of sound in water
C	Stiffness tensor
$C_{\varepsilon 1}$	$k - \varepsilon$ model constant
$C_{\varepsilon 2}$	$k - \varepsilon$ model constant
C_μ	$k - \varepsilon$ model constant
C_D	Particle drag coefficient
d_p, d_w	Particle and rain droplet diameter
D_t	Isotropic dissipation at wall ($k - \varepsilon$ model)
D	Damage per unit surface
E_t	Additional source term ($k - \varepsilon$ model)
E	Young's modulus
e	Erosion per unit mass
f_i	Components of Reynolds averaged volume force in N-S momentum equation
f_1	$k - \varepsilon$ model constant
f_2	$k - \varepsilon$ model constant
$\mathbf{f}_f$	Volume forces term in the URANSE momentum equation
$\mathbf{F}, \mathbf{F}_D$	Force and drag force on particle
F_i, F_d	General and minimum impact force to have damage
F_{iI}	Component of the deformation gradient
$\mathbf{g}$	Gravity acceleration vector
$\mathbf{h}$	Traction vector at FSI interface
$H()$	Heaviside function
$\mathbf{I}$	Identity matrix
J	Jacobian determinant
k	Turbulent kinetic energy
k_M, k_{Mv}, k_{Ma}	Generalized-α method constant
K_m	Fracture toughness
K_1, K_2, K_3	Tabakoff model empirical constants
$\mathbf{K}_{[]}$	FEM stiffness matrix
m_p, m_w	Particle and droplet mass

$\mathbf{M}, \mathbf{M}_{ab}$	FEM mass matrix
$\mathbf{n}_s$	Normal vector at the solid surface
$\mathbf{n}_f$	Normal vector at the fluid-solid interface
n_{en}, n_{el}	Node at element and element number in the FEM discretization
N_n	Shape function at node n
$\bar{P}$	Production term $k - \varepsilon$ model
P_k	Production term $k - \varepsilon$ model
P	Power
Pe	Peclet number
$\tilde{p}$	Non-dimensional static pressure
p_{inf}	Free stream static pressure
p	Pressure
$\bar{p}$	Reynolds averaged fluid pressure
$q_{[]}$	Trial scalar function defined in the [] domain
r	Local radius
r_k, r_ε	Reaction number
R	Rotor radius
Re_x	Reynolds number ($Re = Vx/v$)
Re_T	Turbulent Reynolds number
Re_p	Particle Reynolds number
R_T	Tangential restitution factor
S	Cascade pitch
S_k	Source term ($k - \varepsilon$ model)
S_ε	Source term ($k - \varepsilon$ model)
T	Simulation period
$\bar{U}_i$	Reynolds averaged flow velocity components
u'_i	Fluctuation velocity component for RANS equations
$\mathbf{u}_f$	Flow field average velocity
$\mathbf{u}_s$	Structure local displacement
$\mathbf{v}_s$	Structure local velocity
$\mathbf{u}_m$	Mesh velocity
$\mathbf{u}_{inf}, \mathbf{u}_{test}$	Undisturbed flow velocity at inlet
$\tilde{\mathbf{u}}_f$	Non-dimensional flow field average velocity
$\mathbf{U}_{[]}$	FEM nodal values vector
$\mathbf{v}_p, \mathbf{v}_c$	Particle and cloud velocity
V	Volume
$\mathbf{w}_{[]}$	Trial vector function defined in the [] domain
$\mathbf{x}_p, \mathbf{x}_c$	Particle and cloud position
$\hat{\mathbf{x}}$	Reference initial domain coordinates
$\mathbf{x}$	Current configuration coordinates
x_i	Spatial coordinates
y^+	Non dimensional wall distance ($y^+ = y_n u_\tau/v$)

Greek

α_F, α_M	Generalized-α method constant
α_P	Volume fraction of dispersed phase in multiphase flows
β	Generalized-α method constant
β_1, β_0	General and maximum erosion impact angle
γ	Generalized-α method constant
$\delta[]$	Variation of quantity []
Δt	Time step
Δn_w	Number of droplets impacting the surface in Δt
ε	Turbulent dissipation rate
$\varepsilon_{\mathbf{f}}$	Fluid strain rate tensor
$\varepsilon_{\mathbf{s}}$	Solid strain tensor
$\varepsilon_{\mathbf{m}}$	Solid extension strain tensor
ϕ	Vector trial function for $k - \varepsilon$ model
λ_1, λ_2	Lamé constants
κ_{DRDJ}	DRDJ diffusivity
μ	Dynamic viscosity
μ_t	Turbulent eddy viscosity
∇	Divergence operator
∇_x	Divergence operator with respect to the deformed domain
ν	Kinematic viscosity
ν_p	Poisson's ratio
ν_t	Turbulent kinematic viscosity
ω	Angular velocity
$\Omega_{[]}$	Solution domain
ψ	Vector test function for $k - \varepsilon$ model
ρ_f	Fluid density
ρ_s	Solid density
ρ_p	Particle density
ρ_w	Water density
$\boldsymbol{\sigma}_f$	Fluid stress tensor
$\boldsymbol{\sigma}_s$	Solid stress tensor
$\boldsymbol{\sigma}_m$	Solid extension stress tensor in mesh equivalent elasticity
σ	Standard deviation
τ_{ij}	Kirchhoff stress
τ_p	Particle response time
τ_e	Average time between particle inner collisions
τ_R	Particle relaxation time
τ_L	Lagrangian integral time scale
τ_{PSPG}, τ_{SUPG}	PSPG and SUPG stabilization factor
θ	Implicit integration scheme coupling constant
θ_p	Blade section local pitch angle

ξ Non-dimensional vorticity magnitude

To my family

Chapter 1

Research program overview and industrial context

1.1 Introduction

An operating turbomachinery implies a very complex system of phenomena involving the structural parts (rigid and elastic dynamics, thermodynamics, interactions, contacts and constraints), the fluid part (fluid and gas dynamics, thermodynamics, chemical reactions, phase changes), the auxiliary systems (controls), the particles part (eroded materials, water droplets, dusts and solid impurities) and the interaction of all of these aspects. Knowledge and comprehension of all these phenomena is crucial to obtain a good design.

In an industrial production process, the design part should be advanced enough to guarantee a minimum waste of resources and a minimum time to arrive to the final product. Considering the complex system described above, to reach an optimal new design, the procedure could be very long and could require several iterations on the prototype.

In order to reduce these iterations R & D engineers use the so-called CAE (computer-aided engineering) to obtain the first prototype in a virtual environment. Virtual prototyping allows designing, testing and, possibly, to change the product with a cost that is fairly lower than in the real prototyping. In theory, when we design a product using a CAE tool, the more the model implemented is accurate, the less will be the steps and the time necessary to complete the design (and the lower will be the design costs).

What is happening in practice is that, in parallel with the development of the perfect models for the CAE tools, engineers and R & D companies have to face the computational costs associated to very high-fidelity models. Therefore, we can observe a sort of time shift between the physical phenomena comprehension and the development of mathematical models, numerical techniques, research CAE tools model accuracy and industrial CAE tools model accuracy (which usually results in the lowest one). One of the motivations is that, at a certain level, the increasing in accuracy for CAE tools does not justify the increasing in computational costs, with respect to the cost saving obtainable using the upgraded model.

However, during the last decades, the computer technology has been demonstrating

an incessant rate of growth and development, giving the possibility to continuously extend the sizes of the numerical problems solvable by using medium price calculus resources. Following this trend, it is important to develop the models and the numerical techniques in order to increase the accuracy because, looking at the future, the technology will be such as to give to all the industries the possibility to use the best models and to reduce the design procedure in only two steps: a "one-shot" virtual prototyping followed by the final verification of the real product.

Looking at the turbomachinery virtual prototyping and testing, we will see that a promising and necessary development is to be able in analysing the interaction between the fluid and solid phases on the main process. This is what this project is working for, namely, the definition, development and testing of numerical fluid-solid interaction tools and methods, specialized on turbomachinery applications. In particular, we will develop a fluid-structure interaction (FSI) solver able to simulate three-dimensional aerodynamics and structure dynamics, with a strong and direct coupling. The second main coupling phenomena we are going to deal, is the erosion due to particle-laden flows. In this case, the interface algorithm will couple the particle dynamics with the flow field and, in a last development the change of geometry due to the erosion.

The actual strategy to study complex and multi-physical systems consists on subdividing the physics involved in consistent subsystems (for example the fluid and solid dynamics), using different dedicated models. Once the mathematical models has defined, the strategy to simplify the implementation and the computational complexity implies to define some scales and bands of interaction in such a way to can split every single problem in simpler sub-problems, avoiding, where possible, the direct coupling between different systems.

In most of the cases, the necessity in reducing the computational effort leads to use linearized and low order models. These models neglect the most part of the complex dynamics and coupling effects, which typically can be described with non-linear equations. For these cases, the numerical solution reduces its field of application to few situations, e.g. the steady condition at the main operating point. The prediction obtainable applying these models is affected with a certain grade of approximation and a certain range of usability, which must be taken into account in the design process.
The effect of making a design accepting these approximations and restrictions can be that a virtual prototype would show good performance only in few operating conditions (the ones considered in the simulations) while, it will have an unpredictable behaviour in off-design conditions. For this reason, an iterative optimization process on the prototype (and on the final product) will be necessary to arrive to the definitive object. Indeed, all of the engineering products had crossed in its

development a continuous revision relative to the experience of the response of it to those complex phenomena that were not taken into account during the first design. To be able in simulating also complex and coupled dynamics will reduce this design time.

The next session and chapter will report in detail the modelling and implementation adopted for the development of these numerical tools. An important aspect to underline here is that the choice of the modelling is always related to the target type of application. In industrial production of turbomachinery, representative applications in this topic come from wind turbine and large axial fan fields as will be discussed in the next sections.

1.2 Computational mechanics applied to turbomachinery problems (state of the art)

The purpose of this research is to continue the development of new CAE tools for numerical simulation and testing of turbomachinery. As already underlined, the actual commercial tools (which are the ones used in the industries), have not the possibility of dealing with strong coupling FSI and erosion phenomena, which represents the aspects developed here.

In any case, the first step is to prepare a solid base of knowledge on the actual technology used in computational physics, in order to choose and eventually develop the most suitable models needed to our dedicated tools. The choice has two main constraints to consider, we should use the most hi-fidelity model, but keeping the computational costs controlled to maintain the tool suitable for industrial production applications.

The applications of the computational physics to the turbomachinery field are innumerable because of the complexity and depth of the arguments involved. We will focus here on the main process, and in particular on the mechanics of the process fluid (not reacting) and of the main structures (rotors, stators, cases and hub).

In addition, in this case we can find a huge database of researches in which numerical models are applied to study the different dynamics. A brief recall of the state of the art in numerical simulation commonly applied in the turbomachinery industries and research is reported in the following lines.

- **Fluid-dynamics and aerodynamics**, The CAE tools used for the simulation of the aerodynamics are the so called CFD (Computational Fluid Dynamics) solvers. The development of CFD began several years ago and saw an incessant growth. To list all the model that could be used is far from the purpose of this thesis.

  Forgetting about the mono-dimensional, potential and low-Reynolds flow

models, a way to subdivide the models for CFD application is based on how and if they model the turbulence. At the actual stage, the most used and tested models for the solution of the aerodynamic field in turbomachinery applications are the RANS (Reynolds Averaged Navier Stokes) based models. The motivation of their success is related to a good ratio between accuracy of the three-dimensional solution and computational time. At this moment, it is possible to find a plenty of commercial and open source software which can solve the RANS problems (e.g. FLUENT, CFD++, OpenFOAM). The mostly used technique to discretize and numerically solve the equations is the finite volume method, especially for its light impact on the computational resources, considering the large amount of cells needed to solve turbulent high-Reynolds flows.

- **Structure dynamics**, For the simulation of the stress state and deformation of the structures, the mostly used approach is the Finite Element Method (FEM) technique which allows to solve complex and three-dimensional structures with high-fidelity models. The solution of the structure dynamics through the FEM followed a parallel development with respect to the CFD tools. We can find several commercial and open source software, which guarantee a very high level of accuracy both in case of simple (e.g. metallic) and complex (e.g. composites) materials (NASTRAN, ANSYS, FEMAP, ABAQUS).

- **Coupled systems**, when it is proven that two or more dynamics can be considered *one-way coupled* (which means that the mutual influence can be neglected), it will be possible to study the interaction through a quasi-static and weak coupled approach, using the tools presented at the beginning of this chapter in an open-loop systematic procedure.

All the introduced tools are very specialized and highly developed but they all presents the same limit if observed in the wider context of the virtual prototyping. Indeed, in a real machine all the dynamics are, in general, coupled and mutual influencing. Of course, the magnitude of the coupling effect on the global solution depends on the ratio between critical quantities, e.g. in a fluid-structure interaction problem, the mutual effect depends on the ratio between quantities like densities and main frequencies.

1.2.1   A background on fluid-structure interaction

In the past, the fluid-structure interaction was considered less important than other structural and aerodynamic problems, because, for metal blades with little aspect ratio (blade span vs blade chord), the blade response follows frequencies which are far from the main frequency of variation of the main aerodynamic fields. On the other hand, the blade stiffness is very high and the structural response becomes

important from a stress point of view, only for big variation in magnitude of the aerodynamic field, which, in low-Mach number flows, usually are related to low-frequency variation of the average field. In this frame, the application of the weak coupling procedure can be used to study the aeroelastic effect.

With the introduction of new materials and the refinement of the aerodynamic design of the blade (toward more slender and complex shapes) the aeroelastic problem acquires much more importance in the design phase. This is actually true in applications concerning wind turbines, but it becomes important also for large new fans. In the case of wind turbines, the mostly used tools are based on the BEM (Blade element momentum) theory coupled in a weak fashion, with a mono-dimensional beam model for the structure. These models usually keep into account the unsteadiness of the aerodynamic field using empirical and corrective models for the dynamic wake and for the dynamic stall. To have an example of the state of the art in the application of all these theories it is possible to refer to all the material produced and pubblished by the NREL (National Renewable Energy Lab) with respect to the FAST code [1], which is a very famous simulation tool used to study the wind turbine dynamics and aeroelasticity. This model presents two limits, the first associated to the coupling method, which is weak. Indeed, first the aerodynamic is evaluated using the BEM theory in a quasi-static, equilibrium state of the blade strip, then the aerodynamic load is integrated and used as boundary condition of the beam model to solve the structure dynamics. The second limit concerns the 2D approximation made by the BEM theory, which neglects the three-dimensional effects.

In case of less slender and faster blades, it is possible to find FSI and aeroelasticity works especially on rotorcrafts, with the application of the unsteady boundary element methods strongly coupled with non-linear beam models, as done by Morino and Gennaretti [2]. This method, which is very fast and accurate, is limited to the range of application in which the blades work at small angle of attacks, because the impossibility of the potential theory to predict the separation phenomena.

In case of flows with separation, non-linear and turbulent aerodynamics we need to increase the complexity of the base models. We can find a large amount of material published by Tezduyar, Bazilevs and Takizawa ([3, 4]), using the finite element method and isogeometric analysis applied to solve FSI problem. An example of application to turbomachinery is the work of Bazilevs on large wind turbine, presented in [5]. Here the entire aerodynamic field is simulated directly with a stabilized formulation of Navier-Stokes equations (ALE-VMS) while the structure is modelled with a very high fidelity isogeometric-FEM model, based on a non-linear membrane theory.

1.2.2   A background on wearing on material

The impact of particles on a deposit layer or a clean surface can cause erosion. Modelling this phenomenon is quite complex because several aspects must be accounted for (i.e., impact velocity, particle shape, bonding forces, particle pattern in the deposit layer, particle sintering, etc.).

The numerical study of erosion and deposit phenomena is usually done using particles based models. In the spectra of the possible mathematical models, we can identify two main techniques, the single particle approach and the particle clouds tracking (PCT) approach. As the name suggests, the first method follows the motion of each single particle while the second approach uses a statistical description of the motion of clouds of particles, reducing the computational cost.

For our actual purpose the PCT represents the most interesting solution as it allows to simulate large amounts of particles impacts with a low computational cost. The method was proposed by Baxter in [6] and developed for example in [7]. There, authors simulate the erosion due to coal ash on a metal fan blade, showing a good qualitative agreement with the experimental observation both in time needed to erode the surface and in shape of eroded area.

The particle dynamic solver gives as output the number, direction and energy of impacts that the particles have on the target. In order to evaluate erosion or deposit on the surface, a proper model is needed. The phenomenon is complex and mostly related to the material properties of both target and particles, but also on the shape and sizes of the particles themselves, the mostly used models are empirical and related to the particular case. Tabakoff for example presented an erosion model for coal ash transported in turbine flow in [8].

As we are interested also in the rain erosion on plastic materials (for the wind turbines case) we need a further model that can be found on the work of Keegan et al. [9, 10]. Here the rain and hailstone erosion on a simple covering material used in the wind turbines is studied. Authors used both numerical and experimental tools to study the mechanics of the impact and the damages on the surface, providing a suitable erosion model.

A study on the rain erosion effect on the airfoils used for wind turbine has been presented also by Fiore in [11]. The author applied a single particle approach coupled with a double-lattice method to study the aerodynamics. The model adopted for the aerodynamics gives good results in the range of little angles of attack in very short computational time; this allowed the author to study a large range of configurations and to propose an optimization method on the shape.

Although it is possible to find a large number of studies on the weak coupled solution of erosion on turbomachinery parts due to transported particle, there are very few studies on the mutual effect between erosion due to particle transport and change in the shape of the target. A reference work can be what presented by Casaday [12], in which authors study the change in geometry and its effect on the flow

using a systematic approach. Not more seems to be as automatic calculation like what we will develop and present in Chapter 6.

1.3 Research scope and description

This research poses as main objective to develop numerical tools, which are able to solve complex and strongly coupled fluid-solid interaction problems, starting from an already tested and developed platform. The possible different developments are an indefinite number; we choose to focus our development basing on our main skills and experience, deciding to develop in parallel the aspects of fluid-structure interaction and blade erosion due to transported particles.

At his previous form, the CAE tool package developed by our group was been devoted to study the aerodynamics and erosion/deposit in turbomachinery application, with the main attention to axial fan blades. A natural follow-up to this work is to extend the study including the blade structural behaviour in view of new slender and lighter blade designs. Indeed, composite materials are now in common use in large blade manufacturing, but also the blade radius and aspect ratio are growing to increase the efficiency. This aspect leads to important fluid-structure interaction and vibro-acoustics phenomena, which need detailed computational methods for a reliable prediction.

We focus our attention also on another fluid-solid interaction phenomena, which is the particle erosion of the blades. Looking at the actual common request of the scientific and industrial community, we found two interesting development to add new capabilities to our CAE tools

- the rain erosion phenomena applied to wind turbines, solved adapting a suitable model of the rain erosion to the particle cloud tracking method already implemented and successfully used in works as [13] on large ventilation fans.

- the coupling between the change of geometry due to the particle erosion and the aerodynamic field, which transport the particles themselves.

1.3.1 Synthesis of the program

The first part of the work will be the identification and development of mathematical models suitable to describe the physical systems. Fluid-structure interaction and erosion phenomena are a multi-physics problems that couples the unsteady flow field evolution with the response of an immersed structure or particle motion. It is crucial to find the correct modelling of all these aspects, taking into account the final application of the work.

Using an URANS model represents the most suitable choice to simulate the aerodynamic for both the applications. Indeed, for fluid-structure interaction, we need a good description of the aerodynamic forces (especially the pressure forces) at the

surface of the structure and these models permit to simulate the three-dimensional flow also in case of separation. The averaged solution of the turbulence in the timestep introduce a negligible error as, in the cases in study, the scales associated to the significant FSI coupling follow slower dynamics than the velocity fluctuation due to turbulence.

Furthermore, the same averaged field gives the perfect description for the particle cloud tracking approach, which base its equations on the statistical description of the flow turbulence. Indeed, we will use the cloud description for the particle dynamics as it allows to solve problems of a huge amount of particles (as the rain in wind turbine rain erosion) saving computational costs.

For the structure dynamics, we have to consider the structure of the industrial fan blades we are going to test. Actually, the blades are made by metal alloys or reinforced plastic materials with short or particulate glass and carbon fibres. These materials can be modelled as isotropic and elastic. Furthermore, we consider that for our application, the material should work always in the elastic domain thus the linear elasticity can be used, allowing the finite deformations considering the equations written in the deformed configuration.

Both FSI and erosion problems imply to move the computational domain, following the solid deformation, in the first case, and the surface erosion, in the second case. The mesh motion problem can be solved with a solid extension technique, deforming all the mesh as an elastic body with forced displacement at the boundary.

All the introduced modelling will be presented in detail in Chapter 2.

The finite element method (FEM) will be applied to solve all the sub-problems (fluid flow, structure dynamics, mesh motion, impact/erosion). Especially for the fluid solution, stabilization methods must be used to obtain the numerical solution. Then, for the structural and moving-mesh problems, the weighted residual method can be applied to the three-dimensional elastic problem.

Chapter 3 reports all the FE formulations implemented in the codes and describes also the coupling and interface algorithms to solve FSI and UEB (Updating eroded boundary).

Overview on the numerical solver development for FSI computations

The Fluid Structure Interaction (FSI) analysis could be a useful instrument in terms of:

- Quantification of the structural response to given flow condition.

- Classification of the mechanism underlying the coupling between fluid and structure.

- Characterization of the fatigue in the structure.

- Design expedients to minimize the self-induced vibrations.

This is the reason why many authors developed different strategies for FSI resolution problem. The most used methods to achieve the strong coupling in FSI solution are the so called *partitioned* (or *block-iterative)* approach and the *monolithic* approach.

The adjective "monolithic" is used to identify a global process of discretization on a one enlarged system of equations. In [14, 15, 16] , it is possible to find application of this approach developed by Hubner (2004), Walhorn (2005) and Tezduyar (2006). Another point of view that characterizes the FSI resolution process requires the application of a partitioned scheme. In this way, authors are able to use a specific solver for each region of the domain. The interaction between fluid and solid region is managed by the boundary conditions of the specific solver. The partitioned approach is based on the possibility to apply a specific solver that represents the state-of-art for each physical domain. Following this logic, it is possible to develop an efficient global algorithm, with different grid resolution in the coupling interface between the two domains. Nevertheless, this aspect has to be considered in a particular way, especially during the information transfer process, in the interface zone between different solvers [17, 18].

Establishing a comparison between these two schemes is not a simple task, however, in [19] Degroote (2008) analyses the behaviour of this resolution methods using the same process of discretization. The main result of this analysis is related to the lower computational load required by "partitioned" approach then the "monolithic" one. This difference is considerable if we considerate that the accuracy of the result obtained by these methods is comparable.

Monolithic approach is highly recommended for FSI problems where the stiffness of the structure is very low and the densities between fluid and solid phase are comparable.

The idea behind our study is to solve the different physical domains consecutively in each time interval using dedicated models and avoiding too complex and sparse matrices associate to the final discretized system. However, the simple block-iterative solution presents limits on particularly coupled problems as the separate dynamics are "blind" on what happen on the others, during the separate non-linear convergence steps. Starting from this consideration we propose a mixed algorithm which uses a unique non-linear loop to achieve convergence on the residual of all the systems (like in the monolithic approach), but solving them in a *segregated* fashion, keeping frozen the coupling between different dynamics, only at the single linear solution step, and updating them at each non-linear iteration.

The method consists of a systematic approach, which will be described in detail in Chapter 3.

Overview on the numerical solver development for erosion-geometry morphing computation

Few works can be found on numerical studies that couple aerodynamic and turbulent flows with erosion due to transported particle, in which the change in geometry as effect of the erosion itself is considered, also in the aerodynamic calculation.

Indeed, in usual applications the time needed by the particles to erode an amount of material as large as to change the aerodynamic field is huge. However, if we consider the time scale not in seconds but related to the life of a mechanical part, especially if the part shape is optimized to maximize the aerodynamic performance, a similar study can be extremely useful to evaluate directly a measure of the loss in performance of the part.

Furthermore, the shape of the erosion (as will be presented in the application of Chapter 6) is affected by the change in shape of the boundary as it is related to the impact direction and thus on the normal at the surface that changes if the boundary moves.

As we said, the timing related to this change of geometry is huge so it is possible to develop the algorithm keeping the weak coupling hypothesis. As will be showed, the coupled solver will have the shape of an interface between the two separate solvers, steady RANS and PCT, coupling the two with a dedicated empirical erosion model, which gives the displacement at the mesh boundary to a moving mesh solver. The erosion will be calculated through an iterative procedure in which the iteration represents a time scaled on the time needed to erode a minimum given amount of material (chosen by the user).

1.4   Industrial and research context

1.4.1   Ultimate challenges in wind turbine blades technology

The last updates in wind energy are mainly focused to increase the specific power produced in order to reduce the gap in cost of energy with respect to the other traditional forms. This aspect of course is primarily related to the wind resource. Indeed, a great and continuous increasing of the amount of electric energy produced by wind resource can be visible in the countries of the North of Europe. There, the wind resource appears ideal for the power production, especially in offshore sites.

Application in rigid climate regions lead to damages on the wind turbine blades as effect of ice, rain and sand erosion. Focusing on the rain erosion phenomena, it can be showed that a not protected blade subjected to rainy climates can been damaged by rain erosion resulting in a loss of about 20 % of performance.

Few numerical and experimental works were been presented on this topic (e.g. [9, 11, 20]), in these researches the blade is modelled as a wing strip and the particular interaction between rain and coating material is studied in detail. With our numerical tool, we can study the phenomenon on the full size blade, coupling the RANS
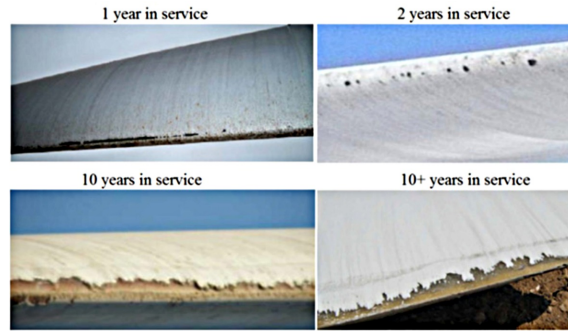
FIGURE 1.1: Wind turbine leading edge erosion due to rain [23]
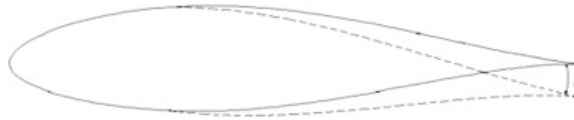
FIGURE 1.2: Camber control concept with morphing airfoil [22]

aerodynamic solution with a particle cloud model of the rain.

It is very easy to observe that to study similar phenomena in an experimental way, implies a study restricted only on the material, and extracted from the real application. In fact, the sizes of the new wind turbine blades do not allow to build an experimental facility like in [21], always remembering the most important purpose of wind industry, to save costs.

The work presented in Chapter 7 will show that, applying the aerodynamic solver in coupling with the PCT solver and a proper erosion model, we can be able to predict the amount of damage on the blade surface, finding the most erosion exposed areas, giving to the designer the possibility to optimize the material distribution and save production costs.

Another aspect of sensible interest is the load and performance control. With the increasing of blades size, the standard control systems can be improved and supported introducing new solutions as presented for example in [22]. One interesting solution is to control, morphing the geometry, the effect due to the unsteady and turbulent shape of the wind on the blade section performance and load. This avoids to turn the entire blade to follow the short period fluctuation of the wind velocity, allowing to use the standard control pitch without the need of improving its velocity and thus its power consumption and weight.

Chapter 4 will report an example of numerical analysis of an active and then a passive morphing system applied to improve the performance of a multi-MW wind turbine.

1.4.2 Ultimate challenges in fan blades technology

An other field of interesting applications is the large axial fan aeroelasticity and control.

Numerical simulation tools are acquiring a crucial role in the virtual prototyping of new fan rotor blades. This, in addition with the possibility in using new advanced materials, is opening the design capability to blades of longer, lighter and more slender structures.

The possibility to simulate directly both the aerodynamic and the effective structure response opens the way to improved design capabilities, avoiding time waste and costs due to long experimental testing campaign and over-dimensioned structures.

In Chapter 5 we will apply the FSI solver to an existing fan blade. The study will show how, even in case of metal structure with little deformation, the coupling between fluid dynamics and structure dynamics can produce effects on both the fluid and the solid involved in the machine main process.

The concept of morphing geometry to control and stabilize the flow was been proposed and applied in several aeronautic and wind turbine applications. We studied the effect of a similar passive system on a large fan blade in order to see if the adoption of this kind of solution brings to benefits on the fan behaviour in off-design conditions.

In Chapter 4 we will report a numerical study on the effect that a passive morphing system (made by an elastic-low stiffness surface) has on the sectional load and flow-field, when it is applied to the trailing edge of an axial fan.

We obtain the results extracting the section of the fan blade and test it in the 2D cascade, with and without the elastic device, in different operating conditions.

It will be possible to observe how the tested device could reduce the load in off-design and high angle of attack conditions, while the same solution could introduce vibrations in design conditions. This study is then extended to the three-dimensional blade to complete the device testing, including the 3D effects.

Chapter 2

Computational mechanics models

As introduced in the previous chapter, for each branch of the multi-physical system we are going to solve we have to find, define and implement a consistent mathematical model. The choice of the model depends on and implies the range of application for which the numerical solver will be suitable. A further consideration have to be done on the computational cost and implementation complexity that results from the chosen model.

Starting from the applications proposed in the first chapter, we can identify the correct mathematical models, observing the properties of the physical fields relative to each particular type of problem. For example, the flow field relative to wind turbines and axial subsonic fans can be characterized by three-dimensional effects, high Reynolds numbers and low Mach numbers. Hence, to simulate the aerodynamics we will need a model for unsteady, three-dimensional, turbulent and incompressible flows.

For FSI we need to define the structural model. In this case, all the applications we propose here, will deal with isotropic materials and three-dimensional solid structures. The properties of the material used for the tested blades we are testing allow to use the theory of linear elasticity. Furthermore, we are not solving structure that are supposed to lead plastic deformations on their material. Bigger deformations can be achieved using the deformed domain as domain base for the local displacement computations.

In this chapter, we will present also the mathematical models used to simulate the particles and their dynamics. For the case of rain simulation, since the big amount of particles, we choose to use the Particle Cloud Tracking method in order to reduce the computational cost. Indeed, the surface of a wind turbine blade is huge with respect to the single raindrop, so it would not have sense to simulate the dynamics of every single droplet to quantify the average damage on the surface.

Finally, we need to define the interface methods and algorithm to couple the different physical system. Leaving the description of the implemented coupling algorithm to Chapter 3, here we will describe the base equations used at the FSI interface and defined to couple the turbulence with the particle could dynamics.

2.1   Aerodynamic Model

2.1.1   Unsteady Reynolds averaged Navier–Stokes equations for incompressible flows

We recall here the Navier-Stokes equations for incompressible, turbulent flows, written in the Reynolds Averaged form. These equations will be the starting point of the discussion that will bring to the final aerodynamic model.

Since that the turbulence is a three-dimensional unsteady phenomenon, the numerical solution of the original N-S equations (DNS - direct numerical simulation) requires a huge amount of computational resources because of the discretizations in time and space. Indeed, the computational domain must have very small control volumes in order to catch every turbulent scale in every place of the field. This is the motivation why, at the actual situation, DNS is used only in research and is applied only on very simple geometries.

In practical problems, we can use statistical averaged equations in order to reduce the problem size. Indeed, we can focus on and solve the quantities that are important for the industrial application (like forces and mean velocities), modelling all the fine scales which are of secondary importance for it.

The way to obtain the RANS equations from the standard N-S equations is to apply the Reynolds averaging [24]. Let $\hat{\phi}$ the instantaneous value of one of the quantities from the N-S equations (velocity, pressure, density, temperature, etc.) it can be decomposed as follows:

$$\hat{\phi} = \bar{\Phi} + \phi' \tag{2.1}$$

where $\bar{\Phi}$ is the mean value (which can be obtained with different averaging method), and ϕ' represents the fluctuations.

Applying this decomposition to the incompressible N-S equation variables, and averaging the resulting equation in time, we can obtain:

$$\frac{\partial \bar{U}_i}{\partial x_i} = 0 \tag{2.2}$$

for the continuity equation, and for the momentum equation (in components):

$$\rho_f \left[\frac{\partial \bar{U}_i}{\partial t} + \bar{U}_j \frac{\partial \bar{U}_i}{\partial x_j} \right] - \bar{f}_i - \frac{\partial \bar{p}}{\partial x_i} - \frac{\partial}{\partial x_j} \left[\mu \left(\frac{\partial \bar{U}_i}{\partial x_j} + \frac{\partial \bar{U}_j}{\partial x_i} - \frac{2}{3} \delta_{ij} \frac{\partial \bar{U}_k}{\partial x_k} \right) - \rho_f \overline{u_i' u_j'} \right] = 0, \tag{2.3}$$

Notice that, after the averaging procedure, the turbulent stress tensor $\rho_f \overline{u_i' u_j'}$ appears on the momentum equation. This term represents the averaged transport of momentum by the velocity fluctuation. As can be seen, this terms is not linear and it is the only one directly depending on the velocity fluctuation components.

In order to close the RANS equations, this term needs to be supplemented before the solution. This problem, called *Turbulence Closure Problem*, is solved adding to the system some closure equations or algebraic relations. There are two types of

models to close the turbulence problem:

- *Eddy viscosity/diffusivity models*, knows also first-order models

- *Second-moment closures*, knows also as Reynolds stress/flux models

The first order models, which will be our choice for this research work, assume that the turbulent stress is directly related to the mean flow field. They are based on the Boussinesq assumption [25], which states that the turbulent stress tensor can be expressed in terms of the mean rate of strain in the same way as the viscous stress, replacing the molecular viscosity coefficient with the *turbulent (eddy) viscosity*.

2.1.2 Turbulence model

Turbulence is not a local phenomenon but evolves in time and depends on the boundary conditions. This implies that, for a correct definition and evaluation of the eddy viscosity, it should be function of some turbulence parameter and, these parameters should be defined by differential equations in order to account for the turbulence evolution in time and space.

This kind of approach depends on the number of parameters (and so, number of equations) chosen to describe the eddy viscosity. One of the most famous and used model is a two-equation model based on the turbulent kinetic energy k and on the rate of turbulent dissipation ε. The $k - \varepsilon$ model gives good results in case of high-Reynolds, rotating and ducted flows, and it represents the choice we did for our implementation.

As we need a good quality solution at the wall (e.g. because of the interface problem for FSI), we chose to use the low Reynolds $k - \varepsilon$ model of Launder and Sharma [26]. Detailed descriptions and application of the method were presented by Dick and Steelant in [27], Mavriplis et al. in [28] and Patel et al. in [29].

The two-equation model, based on the turbulent kinetic energy and dissipation rate, can be written as

$$\rho_f \left[\frac{\partial k}{\partial t} + \boldsymbol{\nabla} \cdot (k\mathbf{u}_f) \right] = \boldsymbol{\nabla} \cdot \left[\left(\mu + \frac{\mu_t}{\sigma_k} \right) \boldsymbol{\nabla} k \right] + S_k, \qquad (2.4)$$

$$\rho_f \left[\frac{\partial \varepsilon}{\partial t} + \boldsymbol{\nabla} \cdot (\varepsilon\mathbf{u}_f) \right] = \boldsymbol{\nabla} \cdot \left[\left(\mu + \frac{\mu_t}{\sigma_\varepsilon} \right) \boldsymbol{\nabla} \varepsilon \right] + S_\varepsilon, \qquad (2.5)$$

Here

$$S_k = P_k - \rho_f \varepsilon - D_t, \qquad (2.6)$$

$$S_\varepsilon = C_{\varepsilon 1} f_1 P_k \frac{\varepsilon}{k} - C_{\varepsilon 2} f_2 \rho_f \frac{\varepsilon^2}{k} + E_t \qquad (2.7)$$

are the source terms, defining $P_k = \mu_t P - 2/3\rho k S$ as the production term, $D_t = 2\mu \left(\frac{\partial \sqrt{k}}{\partial x_i} \right) \left(\frac{\partial \sqrt{k}}{\partial x_i} \right)$ as the isotropic dissipation at wall. Then the model is closed by

defining the quantities

$$E_t \qquad = 2\mu\mu_t/\rho_f \left(\frac{\partial^2 u_i}{\partial x_j \partial x_k}\right)\left(\frac{\partial^2 u_i}{\partial x_j \partial x_k}\right) \tag{2.8}$$

$$P \quad = 4/3\left[(u_{i,j})^2 - u_{m,m}u_{n,n}\right] + (u_{m,n} + u_{n,m})^2 \tag{2.9}$$

$$\tag{2.10}$$

and $C_{\varepsilon 1}$, f_1, $C_{\varepsilon 2}$, f_2 as model coefficients [26].

The connection between the proposed model and the RANS equations is given by the flow velocities and the turbulent viscosity. The last one is defined as follow:

$$\mu_t = C_\mu \rho_f k^2/\varepsilon \tag{2.11}$$

with

$$C_\mu = 0.09 \exp[-3.4/(1 + Re_T/50)^2], \tag{2.12}$$

in which $Re_T = \rho_f k^2/\mu\varepsilon$ is defined as the turbulent Reynolds number.

2.1.3 Arbitrary Lagrangian-Eulerian formulation for URANS equations

Numerical solvers have to guarantee an appropriate kinematic description of the continuum associated to the described fields. In continuous mechanics, usually the algorithms used in the solution of the equations use two kind of descriptions of the motion:

- *Lagrangian description*, in which every node of the domain follows the material particle during motion. This approach is usually adopted in the production of structural and particles solvers.

- *Eulerian description*, in which the mesh is fixed and the fields move relatively to the nodes position. This approach is largely used in the CFD.

The issue arises when the solver combines at the same time two different physics which are usually solved using the two different approaches (like the coupled FSI problem).

In order to solve an aerodynamic field interfacing a moving structure, we need to move the domain nodes, following the deformation. This motion has to be taken into account in the aerodynamic model if it uses an Eulerian description.

For this kind of problems, a third approach is adjoined to the possibilities listed before, and it is called an *Arbitrary Lagrange-Eulerian* (ALE) description [30]. Several applications of this technique can be found in [31, 32, 33, 34, 35, 36, 37, 38]. As the name suggests, this approach combines the two descriptions in order to do not lose the advantages of describing the aerodynamics using an Eulerian point of view, considering a Lagrangian approach for the mesh motion (both fluid and structural).

Following [39] we can apply the ALE formulation to our aerodynamic model. Let $\Omega_t \subset R^{n_{sd}}$ be the spatial domain with boundary Γ_t, where the subscript t states that the fluid domain have to be considered time dependent. The URANS equations of incompressible flows in the ALE frame can be written on Ω_t and $\forall t \in (0, T)$ as

$$\rho_f \left[\left. \frac{\partial \mathbf{u}_f}{\partial t} \right|_{\hat{x}} + (\mathbf{u}_f - \mathbf{u}_m) \cdot \boldsymbol{\nabla}_x \mathbf{u}_f \right] - \mathbf{f}_f - \boldsymbol{\nabla}_x \cdot \boldsymbol{\sigma}_f = 0, \qquad (2.13)$$

$$\boldsymbol{\nabla}_x \cdot \mathbf{u}_f = 0, \qquad (2.14)$$

$$\rho_f \left[\left. \frac{\partial k}{\partial t} \right|_{\hat{x}} + \boldsymbol{\nabla}_x \cdot (k \mathbf{u}_f) \right] - \boldsymbol{\nabla}_x \cdot \left[\left(\mu + \frac{\mu_t}{\sigma_k} \right) \boldsymbol{\nabla} k \right] - S_k = 0, \qquad (2.15)$$

$$\rho_f \left[\left. \frac{\partial \varepsilon}{\partial t} \right|_{\hat{x}} + \boldsymbol{\nabla}_x \cdot (\varepsilon \mathbf{u}_f) \right] - \boldsymbol{\nabla}_x \cdot \left[\left(\mu + \frac{\mu_t}{\sigma_\varepsilon} \right) \boldsymbol{\nabla} \varepsilon \right] - S_\varepsilon = 0, \qquad (2.16)$$

where ρ_f, $\mathbf{u}_f$ and $\mathbf{f}_f$ are the fluid density, velocity and external force, respectively, while $\mathbf{u}_m$ is the local domain velocity.

The stress tensor $\boldsymbol{\sigma}$ is defined, using the Boussinesq hypothesis, as

$$\boldsymbol{\sigma}_f(p, \mathbf{u}) = -p\mathbf{I} + 2(\mu + \mu_t)\boldsymbol{\varepsilon}_f(\mathbf{u}_f). \qquad (2.17)$$

Here p is the pressure, $\mathbf{I}$ is the identity tensor, μ and μ_t are the molecular and turbulent dynamic viscosities, and $\boldsymbol{\varepsilon}_f(\mathbf{u}_f)$ is the strain-rate tensor:

$$\boldsymbol{\varepsilon}_f(\mathbf{u}_f) = \frac{1}{2} \left((\boldsymbol{\nabla}_x \mathbf{u}_f) + (\boldsymbol{\nabla}_x \mathbf{u}_f)^T \right). \qquad (2.18)$$

As reported in [39], the time derivative has to be taken in a fixed-domain (where $\hat{x}$ represents the spatial coordinates of the reference initial domain), while the spatial gradients are taken with respect to the coordinates of the current configuration of the fluid domain x.

2.2 Structure dynamics model

We will deal for this work with metal and in general isotropic materials. Furthermore, the expected behaviour of the structure has to belong to the elastic regime of the material response. For this reason, we can use for now a linear elastic model for the structure dynamics, considering to treat large deformation of the slender structure, using an *Updated Lagrangian Formulation* in the discretization procedure (see the next chapter for a complete description).

We use the linear elastodynamics theory for Hookean materials as the base mathematical model for the structure dynamics. This represent a well-known theory and a complete description can be found for example in [40].

We can obtain the tensor form of the governing equations starting from the Newton second law. This form is independent of the choice of coordinate system and

represent the general equations of motion for an elastic solid

$$\rho_s \frac{\partial^2 \mathbf{u}_s}{\partial t^2} - \mathbf{f}_s - \nabla_x \cdot \boldsymbol{\sigma}_s = 0, \tag{2.19}$$

where $\mathbf{u}_s$ s is the displacement, $\mathbf{f}_s$ the volume forces vector and $\boldsymbol{\sigma}_s$ the Cauchy stress tensor defined through the constitutive equations

$$\boldsymbol{\sigma}_s = C : \boldsymbol{\varepsilon}_s(\mathbf{u}_s) \tag{2.20}$$

Here, $\boldsymbol{\varepsilon}_s(\mathbf{u}_s)$ represent the strain tensor while C is the fourth-order stiffness tensor.

For the linear elasticity hypothesis, the infinitesimal strain is directly related to the first order derivative of the local displacement through the following *strain-displacement* equation:

$$\boldsymbol{\varepsilon}_s(\mathbf{u}_s) = \frac{1}{2}\left((\nabla_x \mathbf{u}_s) + (\nabla_x \mathbf{u}_s)^T\right). \tag{2.21}$$

Recalling the constitutive equation 2.20, the material information are stored in the stiffness tensor. This is a fourth order tensor with generally 36 independent components, which are considered constant in the linear Hookean theory. The number of independent parameters decrease as the symmetry grade of the material properties increase, until arriving to the isotropic material, which can be defined with only two independent parameters:

$$C = \begin{bmatrix} \lambda_1 + 2\lambda_2 & \lambda_1 & \lambda_1 & 0 & 0 & 0 \\ \lambda_1 & \lambda_1 + 2\lambda_2 & \lambda_1 & 0 & 0 & 0 \\ \lambda_1 & \lambda_1 & \lambda_1 + 2\lambda_2 & 0 & 0 & 0 \\ 0 & 0 & 0 & \lambda_2 & 0 & 0 \\ 0 & 0 & 0 & 0 & \lambda_2 & 0 \\ 0 & 0 & 0 & 0 & 0 & \lambda_2 \end{bmatrix} \tag{2.22}$$

The parameters λ_1 and λ_2 are called Lamé constants. With this definition it is possible to rewrite Eq 2.20 as

$$\sigma_{s,ij} = \lambda_1 \delta_{ij} \varepsilon_{s,kk} + \lambda_2 (\varepsilon_{s,ij} + \varepsilon_{s,ji}) \tag{2.23}$$

using the repeated index convention.

The Lamé constants can be related to the more useful Young's modulus, shear modulus and Poisson's ratio with the following expressions resulting from the inversion of Eq 2.20:

$$\lambda_1 = \frac{E\nu_p}{(1+\nu_p)(1-2\nu_p)}, \ \lambda_2 = G = \frac{E}{2(1+\nu_p)} \tag{2.24}$$

2.3 Mesh motion

The ALE approach implies the motion of the mesh. This motion, in case of domains which keep the original topological properties can be done on the mesh itself, avoiding remeshing. In this way, it is possible to save a lot of computational time because there is no need to recalculate and rebuild all the elements. The only problem on moving the mesh nodes is to find a way which guarantee (minimizing the active controls and iterations) to keep the mesh quality. Indeed, CFD problems are very sensible to the mesh quality, which, if not good enough, could bring to instabilities, non-consistent fields and fake gradients.

The control on the mesh quality takes long time and it is usually done during the mesh design. It would be very difficult and heavy to do it using an automatic algorithm inside of a scientific code, so it becomes very important to find a way to keep the most than possible the original quality of the mesh.

The mesh motion technique proposed by Stein, Tezduyar, and Benney [41, 42] gives the possibility to solve FSI problems with large deformations, keeping and controlling the grid quality during the motion and maintaining the boundary structure of the mesh as designed for the fixed initial reference (constant y^+ during the mesh motion).

This method treats the mesh like an elastic solid and solve the motion problem by solving the static linear elasticity on all mesh nodes, giving as boundary condition the displacements of the boundary. Following [41], let $\Omega_m \subset \mathfrak{R}^{n_{sd}}$ be the domain, with n_{sd} the number of spatial dimensions and Γ_m the boundary. Using the linear elasticity we can write the equation of the elastic equilibrium for the points of Ω_m

$$\boldsymbol{\nabla} \cdot \boldsymbol{\sigma}_m = \mathbf{0}, \tag{2.25}$$

Notice that the volume force term $\mathbf{f}_m = 0$ in this case, because we are interested only on the displacement associated to a boundary displacement, without any external fields effect.

In Eq. 2.25, $\boldsymbol{\sigma}_m$ is the Cauchy stress tensor already defined in the previous chapter. In this case is useful to consider the material associated to the mesh domain as isotropic, so we have

$$\boldsymbol{\sigma}_m = \lambda_1 tr(\boldsymbol{\varepsilon}_m(\mathbf{u}_m))\mathbf{I} + 2\lambda_2\boldsymbol{\varepsilon}_{\mathbf{m}}(\mathbf{u}_{\mathbf{m}}), \tag{2.26}$$

and, again, the strain tensor can be defined in term of mesh displacements $\mathbf{u}_m$, using the linear theory

$$\boldsymbol{\varepsilon}_m(\mathbf{u}_m) = \frac{1}{2}\left((\boldsymbol{\nabla}\mathbf{u}_m) + (\boldsymbol{\nabla}\mathbf{u}_m)^T\right). \tag{2.27}$$

Now the problem is to define properly the Lamé constants λ_1, λ_2 in order to obtain the best result in terms of mesh quality after the displacement.

Continuing to adopt the method proposed by Tezduyar et al., we will obtain the equivalent material properties for the mesh, using the so called Jacobian based

stiffness model. Which will be discuss in the next chapter.

2.4   FSI model, interface equations

In the previous sections, we defined all the mathematical models relative to the different physical systems we are going to solve. In this section we deal about the coupling of these systems and in particular, we will define the relation that allows the interaction between the aerodynamic field and the structural motion and response.

All the following relations are defined at the interface between the two domains. Let $\Gamma_{i,f}$, $\Gamma_{i,s}$ be respectively the portions of the boundary of the fluid and solid domains, which represent the interface. The points of $\Gamma_{i,f}$ and $\Gamma_{i,s}$ are coincident so we can define the following relations between the fields of both the systems on the points of $\Gamma = \Gamma_{i,f} = \Gamma_{i,s}$.

- **Aerodynamic effect on the structure**. The aerodynamic field acts on the structure, transmitting a force on its boundary. This effect can be modelled by applying the fluid traction force as a boundary condition for the structural stress

$$\boldsymbol{\sigma}_s \cdot \mathbf{n}_s - \mathbf{h}_f = \boldsymbol{\sigma}_s \cdot \mathbf{n}_s - \boldsymbol{\sigma}_f \cdot \mathbf{n}_f = 0, \quad on \quad \Gamma_i \qquad (2.28)$$

  here $\mathbf{n}$ are the normal vectors and $\mathbf{h}_f$ is the fluid traction, defined in components as

$$h_{f,i} = -pn_i\delta_{ij} + \varepsilon_{f,ij}n_j \qquad (2.29)$$

- **Effect of the structure velocity on the aerodynamic field**. The moving boundary represents a sort of inflow for the fluid field as the fluid particles at the interface must have zero relative velocity with respect to the wall (for the impermeability and no-slip condition of viscous flows). Hence, if the boundary moves, the fluid at the boundary must follow this movement, transmitting a boundary velocity to the aerodynamic field. This effect can be obtained imposing the following equation on Γ

$$\mathbf{u}_f - \mathbf{v}_s = 0, \quad on \quad \Gamma_i \qquad (2.30)$$

2.5   Particles dynamics and damage in erosion phenomena

The second coupling phenomena we are going to deal is the erosion of the structures (moving or fixed). In turbomachinery, the erosion phenomena are mainly driven by a solid phase dispersed and transported in the fluid field. The material of the particle phase depends on the application and we can find erosion phenomena due to metal particles, coal ash, sand, rain, hail. As introduced before, the actual way to solve the erosion problem in turbomachinery is to model first the transport of the particles with a one-way coupling with the flow solution, and then to apply a

suitable empirical description for the erosion effect.

As presented in [7], two-phase flows can be characterized by two ratios

$$\frac{\tau_p}{\tau_e}, \quad \alpha_p = \frac{\sum_i n_i V_{p,i}}{V} \tag{2.31}$$

the first is the ratio between the particle response time and the average time between inter-particle collisions. The second one is the volume fraction of the dispersed phase. Through these two ratios, it is possible to identify the dense or dilute nature of a flow, choosing the correct model to analyse it.

In our applications, we will deal with particle flows that have $\frac{\tau_p}{\tau_e} < 1$ and $\alpha_p < 10^{-5}$, so we can use a one-way coupling approach in which the solid phase is considered as a dispersed and transported phase, which does not interfere with the fluid dynamics [43].

To deal with this kind of problems the simplest and most common approach is the Lagrangian description of the single particle motion. The particle dynamics is described through an ordinary differential equation called *Basset-Boussinesque-Osees* (BBO) equation [7]

$$m_p \frac{d\mathbf{v_p}}{dt} = \mathbf{F} \tag{2.32}$$

where m_p, $\mathbf{v_p}$ are the particle mass and velocity, while the force term include in general different effects like buoyancy, gravity, pressure gradients force and drag force. Studies on the force contributions can be found for example in [44, 45] where it is demonstrated that, for high values of density ratio (the ratio between the particle density and the fluid density) forces other than the drag do not give relevant contributions to the particle motion. So Eq. 2.32 becomes

$$m_p \frac{d\mathbf{v}_p}{dt} = \mathbf{F}_D = -1/8\pi d_p^2 \rho_f C_D(\mathbf{u}_f - \mathbf{v}_p)|\mathbf{u}_f - \mathbf{v}_p| \tag{2.33}$$

Applications of two-phase flows usually involve turbulent flows. Turbulence has a direct effect on the particle motion thus, it has to be taken into account. Due to the fluctuating character of turbulent velocity field, a dispersion of particle released nominally at the same position is observed, that is particles released from the same position at different time follow different trajectories. This phenomenon is called turbulent dispersion.

The trajectory of a particle is computed by solving its equation of motion, the BBO equation, hence the instantaneous turbulent velocity field should be known. However, this information is not provided by all the turbulence models. RANS models, for instance, provide a time-averaged velocity field; on the contrary LES models compute the instantaneous velocity. Therefore, depending on the turbulence model adopted also turbulent dispersion has to be modelled.

Besides the problem of evaluating the instantaneous velocity field, it has to be taken into account also the number of trajectories to simulate. In order to obtain statistically independent results a huge number of trajectories should be tracked, thus

requiring a huge computational time. To avoid this limit a model is needed. There-
fore, turbulent dispersion models have to accomplish two different tasks: to esti-
mate the instantaneous flow velocity in the position of the particle (if not available,
i.e., in RANS simulations), and to reduce the number of particle trajectories which
has to be tracked.

Considering that the aerodynamic model adopted in this work is a RANS model, a
turbulent dispersion model, and in particular the so-called *Particle Cloud Tracking*
(PCT), will be used and hence described in the following section.

2.5.1   Particles cloud tracking

We use the PCT model [46] to simulate a large number of particles without tracking
them individually. The PCT approach was used in turbulent particle dispersion [47,
48, 49, 50, 51] and validated in turbomachinery and biomass furnaces [52, 53]. In
the PCT model, each trajectory is not related to a particle, but to a group of particles
(a "cloud"), thus representing the evolution of the cloud position as a function of
time:

$$\mathbf{x}_c = \int_0^t \mathbf{v}_c dt' + (\mathbf{x}_c)_0. \tag{2.34}$$

Here, subscript c refers to the cloud, $\mathbf{v}_c$ is the velocity of the cloud, and $(\mathbf{x}_c)_0$ is the
initial position of the cloud, usually at the inflow boundary.

The equation of motion for the cloud is given starting from the Basset–Boussinesque–
Oseen formulation (Eq. 2.33), which, with one-way dependence hypothesis accord-
ing to Armenio and Fiorotto [54], reads as

$$\frac{d\mathbf{v}_c}{dt} = \tau_R^{-1} \left(\langle \mathbf{u} \rangle - \mathbf{v}_c \right) + \langle \mathbf{f} \rangle + \left(1 - \frac{\rho}{\rho_p} \right) \mathbf{g}, \tag{2.35}$$

where $\langle\ \rangle$ denotes ensemble average of the enclosed quantity (defined later), $\mathbf{f}$ is
the centrifugal and Coriolis forces, ρ_p is the particle material density, and τ_R is the
particle relaxation time, which, for spherical particles, reads as

$$\tau_R^{-1} = \frac{3}{4d_p} C_D \frac{\rho}{\rho_p} \| \langle \mathbf{u} \rangle - \mathbf{v}_c \|. \tag{2.36}$$

Here, d_p is the particle diameter and C_D is the drag coefficient based on the particle
Reynolds number $Re_p = \frac{\|\langle \mathbf{u} \rangle - \mathbf{v}_c\| d_p}{\nu}$, first introduced in [55]. The initial condition
for $\mathbf{v}_c$ is given as $\mathbf{v}_c(0) = \langle \mathbf{u} \rangle|_{t=0}$.

The ensemble average for the dispersed phase within the cloud is defined ac-
cording to the hypothesis of independent statistical events, and for any quantity θ
it reads as

$$\langle \theta \rangle = \frac{\int_{\Omega_c} \theta PDF(\mathbf{x},t) d\Omega}{\int_{\Omega_c} PDF(\mathbf{x},t) d\Omega}. \tag{2.37}$$

Here, θ is ensemble-averaged quantity, Ω_c is the cloud domain, and $PDF(\mathbf{x},t)$ is
the multi-variate probability density function of the dispersed phase. This definition

of the ensemble average is appropriate for stationary and non-stationary quantities, and for both continuous and discontinuous quantities.

The PCT approach assumes that particle position distribution within a cloud is Gaussian, and the cloud size varies in time according to the properties of the flow. To this end, the *PDF* describing the particle distribution within the cloud reads as

$$PDF(\mathbf{x},t) = \frac{1}{(2\pi)^{1/2}\sigma} exp\left(-\frac{1}{2}\left(\frac{\|\mathbf{x}-\mathbf{x_c}\|}{\sigma}\right)^2\right). \tag{2.38}$$

Here, σ is the square root of the variance of particle position, which accounts for the turbulent dispersion of particles. We will define it in Section 3.4. The cloud size (cloud radius) is taken as 3σ, and that gives us Ω_c. Each cloud is assumed to consist of perfectly spherical particles with the same chemical and physical characteristics. Combining Eqs. (2.35) and (2.36), we obtain

$$\frac{d\mathbf{v}_c}{dt} = C_D'\|\langle\mathbf{u}\rangle - \mathbf{v}_c\|\left(\langle\mathbf{u}\rangle - \mathbf{v}_c\right) + \langle\mathbf{f}\rangle + \left(1 - \frac{\rho}{\rho_p}\right)\mathbf{g}, \tag{2.39}$$

where

$$C_D' = \frac{3}{4d_p}C_D\frac{\rho}{\rho_p}. \tag{2.40}$$

2.5.2 Turbulence–particle interaction parameters

The variance is taken to be dependent upon the Lagrangian time scale of the particle-laden flow, τ_L, and, according to Baxter [46], its Markovian approximation reads as

$$\sigma^2 = 2(v')_c^2\tau_L^2\left(\frac{t}{\tau_L} - (1 - e^{-t/\tau_L})\right) + \sigma_0^2, \tag{2.41}$$

where τ_L is the Lagrangian integral time scale defined as

$$\tau_L = max(\tau, \tau_p), \tag{2.42}$$

with τ_p and τ the particle motion and turbulence time scales. The fluctuating component of the particle velocity for the cloud, driven by the turbulence–particle interaction [56], reads as

$$(v')_c^2 = (u')_c^2\left(1 - e^{-\tau/\tau_p}\right) = \frac{2}{3}k\left(1 - e^{-\tau/\tau_p}\right). \tag{2.43}$$

2.6 Erosion models

The particular application covers a crucial role in the choice of the erosion model. The erosion mechanism depends on the interaction between materials which have different mechanical properties and fracture behaviours. In turbomachinery applications, the interest is usually pointed on turbo-engines, in the case of coal ash,

metal particle and sand erosion; furthermore, it is common on wind turbines installed in hard climates, to encounter serious performance damages due to rain and hail erosion.

As pointed by Tabakoff in [8] *"The problem of predicting erosion in rotating machinery is very complex and has not been satisfactorily discussed in the literature"* and, *" The theoretical studies concerning erosion are predominantly empirical. They involve basic assumption about the process governing material removal"*.

On the base of this knowledge, we will present and discuss the two erosion model suitable to treat the applications chosen for the purpose of this thesis, which are rain erosion on wind turbine blades and sand erosion on metal structures.

2.6.1   Raindrop erosion

Based on the computed data from the flow and particle computations, we can compute the rain erosion on the surface of a wind turbine blade using one of the models proposed in the literature. Keegan et al. [10] provides a review of the available models for rain erosion. According to Evans et al. [57], a threshold damage velocity can be computed as

$$v_D \approx 1.41 \left(\frac{K_m^2 c_m}{\rho_w^2 c_w^2 d_w} \right)^{1/3}. \tag{2.44}$$

Here ρ_w and c_w are the density of the water and the compressional wave speed in water, and d_w is the droplet diameter; K_m is the fracture toughness of the target material, and c_m is the Rayleigh wave velocity of the target material, defined as

$$c_m = \left(\frac{0.862 + 1.14 v_m}{1 + v_m} \right) \left(\frac{E_m}{2(1 + v_m)\rho_m} \right), \tag{2.45}$$

with ρ_m, v_m and E_m being the density, Poisson's ratio and Young's modulus for the target material.

The threshold damage velocity is the minimum impact velocity of a raindrop that causes erosion damage to the blade. In quantifying the damage, we will use v_D in combination with other computed data. As a first approximation, one can write the impact force of a droplet as

$$F_i = \frac{m_w v_i^2}{d_w}, \tag{2.46}$$

with m_w representing the mass of a water droplet, and v_i its impact velocity. Combining Eqs. (2.44) and (2.46), the minimum impact force that causes damage to the blade, F_d, can be computed. Assuming that the damage is proportional to the impact force and the number of droplets impacting, the damage during the time

step Δt can be predicted as

$$\Delta D = \Delta n_w \frac{F_i}{F_d} H\left(\frac{F_i}{F_D} - 1\right), \qquad (2.47)$$

where Δn_w is the number of droplets impacting during Δt, per unit surface area, and $H(\cdot)$ is the Heaviside step function. We use Eq. (2.47) to predict the erosion patterns. The impact count, n_w, and damage, D, are calculated by summing Δn_w and ΔD over the number of time steps the PCT computation is carried out.

2.6.2 Sand and coal ash erosion

Grant and Tabakoff developed an empirical model to predict the erosion of ductile alloys [58]. This empirical relations together with the analysis of particle trajectories in turbomachines, can be used to predict the erosion on different rotating machine components made by hard particles like coal ash or sand.

Following what presented in [58] and [8], we can define the erosion per unit mass of impacting particles as

$$e = K_1 f(\beta_1) V_1^2 \cos^2 \beta_1 (R_T^2) + f(V_{1N}) \qquad (2.48)$$

Here β_1 is the relative angle between the particle path and the surface, V_1 is the particle velocity, R_T is the tangential restitution ratio

$$R_T = 1 - 0.0016 V_1 \sin \beta_1 \qquad (2.49)$$

and the functions

$$f(\beta_1) = [1 + CK(K_{12} \sin(pi/21/\beta_0)\beta_1)]^2 \qquad (2.50)$$

$$f(V_{1N}) = K_3 (V_1 \sin \beta_1)^4 \qquad (2.51)$$

where β_0 is the angle of maximum erosion, $CK = 1$ for $\beta_1 \leq 3\beta_0$ and $CK = 0$ for $\beta_1 > 3\beta_0$. K_1, K_{12}, K_3 are empirical constants that have to be determined with respect to the particular application in terms of particle and eroded structure materials.

Chapter 3

Discretization, integration and interface schemes

In the previous chapter, we defined all the mathematical models adopted to describe the physics of the problems. Once applied to a particular case, the systems of partial differential equations defined before, become a set of boundary values problems, for which, in general, it is not possible to find an analytical closed solution.

Discretization techniques help to find the approximated solution of the boundary values problem by using numerical schemes and numerical calculus. The expression of the discretized form of the boundary values problem depends on the technique and, in general, we can discretize (passing from an infinitesimal description of the continuum to a finite description of a discretized domain). The main approaches are the well-known *finite differences* (FD), *finite volumes* (FV) and *finite elements* (FE).

In this thesis we will adopt the FE method to discretize and solve numerically all the PDE systems previously defined. The complete treatise and demonstration of consistency of the method is out from the purpose of this thesis, it is possible to find an ample literature on the topic, e.g. the book of T. Hughes [40]. We will give here just a brief description of the fundamentals of the method, passing directly to its application to our problem in the next sections.

The main constituents of the FEM applied to solve a boundary element problem are

- **The variational or weak statement of the problem**. To obtain the variational form of the problem we need to define the trial and test (weights or virtual displacement) functions, in order to apply the virtual work principle.

- **The approximated solution of the variational equations using finite element functions**

The most famous method to obtain the approximated solution of the boundary problem in weak formulation is the Galerkin's method which is an example of so-called *weighted residual methods* completely presented in [59].

In the following discussions we will refer to the trial functions maintaining the nomenclature of the original variable (e.g. with u^h for the displacements) and to the weight functions with an alternative nomenclature (e.g. w^h for the virtual displacements). Here, h refers to the characteristic length scale of the **mesh**, in other

words, of the discretized domain.

All the FEM formulations regarding the FSI modelling were been implemented in the already existing in-house code XENIOS++, while a FORTRAN95 interface was been developed to couple the aerodynamics (XENIOS++), PCT and erosion (P-Track code) modelling.

XENIOS++ [60] is an OOP (object oriented) software developed with the C++ language. It was verified and used by our group for purely CFD computations applied to turbomachinery. PC-Track [7] is a FORTRAN-based code developed and used to study erosion and deposit on turbomachinery parts subjected to particle-laden flows.

3.1 Finite element stabilized formulation of turbulent flow equations in ALE frame

We will base all the aerodynamic formulation, basing on what already implemented in XENIOS++ code [60], extending the same formulation on our moving boundary problem in ALE frame.

As introduced before, we will solve all the equation systems using the Galerkin's least square (GLS) method and in particular (as we will see from the stabilized formulations of the NS problem) the Petrov-Galerkin method.

Given Eqs. (2.13)–(2.14), we can form some suitably-defined finite-dimensional trial solution spaces for velocity and pressure: $\mathscr{S}_{\mathbf{u}}^h$, $\mathscr{S}_p^h$ and, for now, dedicated test function spaces for the continuity and momentum equations $\mathscr{V}_C^h$ and $\mathscr{V}_{NS}^h$.

The finite element formulation of Eqs. (2.13)–(2.14) can be written as follows: find $\mathbf{u}_f^h \in \mathscr{S}_{\mathbf{u}}^h$ and $p^h \in \mathscr{S}_p^h$ such that $\forall \mathbf{w}_C^h \in \mathscr{V}_C^h$ and $\forall \mathbf{w}_{NS}^h \in \mathscr{V}_{NS}^h$:

$$
\int_{\Omega_t} \mathbf{w}_{NS}^h \cdot \rho_f \left(\left. \frac{\partial \mathbf{u}_f^h}{\partial t} \right|_{\hat{x}} + (\mathbf{u}_f^h - \mathbf{u}_m^h) \cdot \boldsymbol{\nabla}_x \mathbf{u}_f^h - \mathbf{f}^h \right) d\Omega + \int_{\Omega_t} \boldsymbol{\varepsilon}(\mathbf{w}_{NS}^h) : \boldsymbol{\sigma}(p^h, \mathbf{u}_f^h) d\Omega
$$

$$
- \int_{\Gamma_{\mathrm{h}}} \mathbf{w}_{NS}^h \cdot \mathbf{h}^h d\Gamma + \int_{\Omega_t} \mathbf{w}_C^h \boldsymbol{\nabla}_x \cdot \mathbf{u}_f^h d\Omega = 0, \tag{3.1}
$$

It is possible to notice how, because of the same integration domain, it is possible to sum the three weak equations (momentum, continuity and boundary condition) in one integral form as in Eq. 3.1.

The same approach can be applied to the two equations of the turbulence model, obtaining the final equations in weak form

$$\int_{\Omega_t} \mathbf{w}_k^h \cdot \rho_f \left(\frac{\partial k^h}{\partial t} \Big|_{\hat{x}} + \boldsymbol{\nabla}_x \cdot (k^h \mathbf{u}_f^h) \right) d\Omega - \int_{\Omega_t} \mathbf{w}_k^h \cdot \left(\boldsymbol{\nabla}_x \cdot \left[\left(\mu + \frac{\mu_t}{\sigma_k} \right) \boldsymbol{\nabla}_x k^h \right] \right) d\Omega$$

$$- \int_{\Omega_t} \mathbf{w}_k^h S_k d\Omega = 0, \tag{3.2}$$

$$\int_{\Omega_t} \mathbf{w}_\varepsilon^h \cdot \rho_f \left(\frac{\partial \varepsilon^h}{\partial t} \Big|_{\hat{x}} + \boldsymbol{\nabla}_x \cdot (\varepsilon^h \mathbf{u}_f^h) \right) d\Omega - \int_{\Omega_t} \mathbf{w}_\varepsilon^h \cdot \left(\boldsymbol{\nabla}_x \cdot \left[\left(\mu + \frac{\mu_t}{\sigma_\varepsilon} \right) \boldsymbol{\nabla}_x \varepsilon^h \right] \right) d\Omega$$

$$- \int_{\Omega_t} \mathbf{w}_\varepsilon^h S_\varepsilon d\Omega = 0. \tag{3.3}$$

The direct application of the finite element method to the Galerkin least squares formulation for the solution of incompressible flows, introduces three sources of instability. Each of those sources must be treated in the formulation of the numerical scheme in order to achieve a stable and consistent approximated solution.

The first source of instability comes from the incompressible condition which treats the pressure variable with a single spatial term in the momentum equation, deprive the system of equations of a pressure evolution equation. This indetermination gives to the system the possibility of violating the inf-sup condition (known as Babuska-Brezzi condition [40]) on the stability.

A second effect is due to the modelling of convective non-symmetric terms with the Galerkin's shape function, which are symmetric operators. This produces non-physical oscillation in the solution of the velocity field. It is possible to demonstrate that the amplitude of the oscillation is a function of the intensity of the convective transport measured by the Peclet number

$$Pe = \frac{uh}{2Diff} \tag{3.4}$$

where u is the local velocity, h the length of the discretization and $Diff$ the diffusivity.

The final source of instability is related to the so-called reactive terms in the turbulence equations, in other words, the terms proportional to the unknown of the equation.

Stabilized formulations to solve all of these aspects were been proposed, developed and successfully used in the last 20 years. In particular

- The PSPG (Pressure Stabilized – Petrov Galerkin) [61] formulation is used to solve the instability due to the incompressible constraint.

- The SUPG (Streamline Upwind – Petrov Galerkin)[62] formulation is used to solve the instability on the convective terms

- The DRD (Diffusion for Reaction Dominated problems) technique [63, 64] is used to solve the instability due to the reactive terms in the turbulence closure model.

3.1.1 PSPG formulation

Basing on what proposed in [61] and recalled in [60], the solution of the numerical instability due to the incompressibility constraint is achieved by relaxing the constraint itself, i.e. making the divergence of the velocity field in the continuity equation dependent by the pressure.

This approach cannot be directly applied because it causes a loss in consistency between the final form and the original differential form of Eq. 2.14. In order to avoid the inconsistency the PSPG technique proposes to introduce a perturbation of the Galerkin weight function applied to the continuity equation. The PSPG term assumes the form:

$$\sum_{e=1}^{n_{el}} \int_{\Omega_t^e} \frac{1}{\rho_f} \tau_{\text{PSPG}} \left(\nabla_x q^h \right) \cdot \left[\text{Ł}(p^h, \mathbf{u}_f^h) - \rho_f \mathbf{f}^h \right] d\Omega = 0, \qquad (3.5)$$

where τ_{PSPG} is the stabilization factor and

$$\text{Ł}(q^h, \mathbf{w}^h) = \rho_f \left(\frac{\partial \mathbf{w}^h}{\partial t} \Big|_{\hat{x}} + (\mathbf{u}_f^h - \mathbf{u}_m^h) \cdot \nabla_x \mathbf{w}^h \right) - \nabla_x \cdot \boldsymbol{\sigma}(q^h, \mathbf{w}^h). \qquad (3.6)$$

which state that the residual of Eq. 2.13 is used for the stabilization, recovering the consistency with the original model.

The stabilization factor is defined using the form proposed in [65]

$$\tau_{\text{PSPG}} = \frac{h}{2\|U\|} Z(Re_U) \qquad (3.7)$$

with h is in this case the diameter of the equivalent sphere at the element, Re_U is the local Re number related to the global velocity and the function Z is defined as follow

$$Z(Re_U) = \coth(Re_U) - \frac{1}{Re_U} \qquad (3.8)$$

3.1.2 SUPG formulation

In general, a discretized description of the non-linear convective terms with symmetric operators (e.g. central finite difference) conducts to instability as the algorithm loses the direction of flow propagation. Upwind schemes allow this capability and avoid the instability with the price of including an additional numerical diffusion.

In the simple scalar upwind schemes, this diffusion is very high and produce a solution, which is stable but highly damped. The Streamline Upwind scheme used in our implementation, allow to reduce this negative effect, restricting the effect of the upwind scheme only on the streamline direction.

It can be demonstrated [60], that such an artificial diffusivity is mathematically

equivalent to modify the Galerkin weight function at the convective term as follows

$$w = w + \tau_{\text{SUPG}} u_i w_i \tag{3.9}$$

In order to keep the consistency, this modification is done on all the weight function of the momentum equation in integral form, giving the final SUPG/PSPG formulation of the ALE-URANSE.

Recalling Eq. 3.1 and defining the test function spaces for the velocity and pressure $\mathscr{V}_{\mathbf{u}}^h$ and $\mathscr{V}_p^h$, we can find $\mathbf{u}_f^h \in \mathscr{S}_{\mathbf{u}}^h$ and $p^h \in \mathscr{S}_p^h$ such that $\forall \mathbf{w}^h \in \mathscr{V}_{\mathbf{u}}^h$ and $\forall q^h \in \mathscr{V}_p^h$:

$$
\begin{aligned}
& \int_{\Omega_t} \mathbf{w}^h \cdot \rho_f \left(\frac{\partial \mathbf{u}_f^h}{\partial t} \Big|_{\hat{x}} + (\mathbf{u}_f^h - \mathbf{u}_m^h) \cdot \nabla_x \mathbf{u}_f^h - \mathbf{f}^h \right) d\Omega + \int_{\Omega_t} \boldsymbol{\varepsilon}(\mathbf{w}^h) : \boldsymbol{\sigma}(p^h, \mathbf{u}_f^h) d\Omega \\
& - \int_{\Gamma_h} \mathbf{w}^h \cdot \mathbf{h}^h d\Gamma + \int_{\Omega_t} q^h \nabla_x \cdot \mathbf{u}_f^h d\Omega \\
& + \sum_{e=1}^{n_{el}} \int_{\Omega_t^e} \frac{1}{\rho_f} \left[\tau_{\text{SUPG}} \rho_f (\mathbf{u}_f^h - \mathbf{u}_m^h) \cdot \nabla_x \mathbf{w}^h + \tau_{\text{PSPG}} \nabla_x q^h \right] \cdot \left[\text{Ł}(p^h, \mathbf{u}_f^h) - \rho_f \mathbf{f}^h \right] d\Omega = 0,
\end{aligned}
\tag{3.10}
$$

In our case, the stabilization factor τ_{SUPG} is defined from [66] as

$$\tau_{\text{SUPG}} = \sum_n^{nen} \left| \mathbf{u}^h \cdot \nabla N_n \right| \tag{3.11}$$

where N_n is the shape function associated to the node n and nen is the number of nodes of the element.

3.1.3 DRD-DRDJ formulation

As introduced, the numerical instability associated to the turbulence closure equations comes from the reactive terms. This source produces significant effects in the situation in which the convective action becomes negligible, i.e. stagnation points and boundary layer separation zone as demonstrated by Corsini et al [67] and in [60].

To solve the problem Corsini in [68] proposed the DRDJ (Diffusion for Reaction Dominated Problem with Jump Factor) based on the DRD technique (Diffusion for Reaction Dominated Problem) formulated by Tezduyar and Park [63], which is the actual technique implemented in the XENIOS++ code. As in the upwind scheme, the DRDJ technique is obtained introducing an additional diffusive term, which depends on the Peclet number and on the reaction number defined as

$$r_k = \frac{c_k h^2}{\nu + \frac{\nu_t}{\sigma_k}} \tag{3.12}$$

for the turbulent kinetic energy equation and

$$r_\varepsilon = \frac{c_\varepsilon h^2}{\nu + \frac{\nu_t}{\sigma_\varepsilon}} \tag{3.13}$$

for the dissipation rate equation.

Using this approach and following the compact form of [68], we can define the vectors of trial and test functions $\phi^h \in \mathscr{S}_\phi^h$ and $\psi^h \in \mathscr{V}_\psi^h$, with $\phi^h = \{k^h, \varepsilon^h\}^T$ and so, to define the weak form of the $k - \varepsilon$ equations as

$$\int_{\Omega_t} \psi^h \cdot \rho_f \left(\frac{\partial \phi^h}{\partial t} \Big|_{\hat{x}} + (\mathbf{u}_f^h - \mathbf{u}_m^h) \cdot \nabla_x \phi^h + \mathbf{B}_{TC} \phi^h - \mathbf{F}_{TC}^h \right) d\Omega$$

$$+ \int_{\Omega_t} \nabla_x \psi^h \cdot \left(\rho_f \nu_{TC} \left(\nabla_x \phi^h \right) \right) d\Omega$$

$$- \sum_{e=1}^{n_{el}} \int_{\Omega_t^e} \mathbf{P}_{TC}^{stab}(\psi^h) \cdot \left[\text{Ł}_{TC}(\phi^h) - \rho_f \mathbf{F}_{TC}^h \right] d\Omega$$

$$+ \sum_{e=1}^{n_{el}} \int_{\Omega_t^e} \mathbf{K}_{TC}^{DC} \rho_f \nabla \psi^h : \nabla \phi^h d\Omega = 0, \tag{3.14}$$

where

$$\text{Ł}_{TC}(\phi^h) = \rho_f \left(\frac{\partial \phi^h}{\partial t} \Big|_{\hat{x}} + (\mathbf{u}_f^h - \mathbf{u}_m^h) \cdot \nabla_x \phi^h + \mathbf{B}_{TC} \phi^h \right) - \nabla_x \cdot \left(\rho_f \nu_{TC} \left(\nabla \phi^h \right) \right) \tag{3.15}$$

defining the following matrices

$$\mathbf{B}_{TC} = \begin{bmatrix} \frac{\varepsilon}{k} & 0 \\ 0 & c_{\varepsilon 2} f_{\varepsilon 2} \frac{\varepsilon}{k} \end{bmatrix} \tag{3.16}$$

$$\nu_{TC} = \begin{bmatrix} \left(\nu + \frac{\nu_t}{\sigma_k} \right) & 0 \\ 0 & \left(\nu + \frac{\nu_t}{\sigma_\varepsilon} \right) \end{bmatrix} \tag{3.17}$$

$$\mathbf{F}_{TC} = \begin{bmatrix} P_k - D \\ C_{\varepsilon 1} P_k \frac{\varepsilon}{k} + E \end{bmatrix} \tag{3.18}$$

$$\mathbf{P}_{TC}^{stab} = \begin{bmatrix} \tau_{SUPG-k} & 0 \\ 0 & \tau_{SUPG-\varepsilon} \end{bmatrix} \tag{3.19}$$

$$\mathbf{K}_{TC}^{DC} = \begin{bmatrix} \kappa_{DRDJ-k} & 0 \\ 0 & \kappa_{DRDJ-\varepsilon} \end{bmatrix} \tag{3.20}$$

Here κ_{DRDJ-k} and $\kappa_{DRDJ-\varepsilon}$ are the DRDJ diffusivities defined in [63, 69, 70, 68, 71]).

3.1.4   Time integration scheme – Crank-Nicolson

Applying the finite element discretizzation

$$u_i = \sum_a N_a(\xi) U_i^a \tag{3.21}$$

it is possible to obtain from the URANS problem the non-linear FE system

$$\mathbf{M}\frac{d\mathbf{U}_f(t)}{dt} + (\mathbf{U}_f(t) - \mathbf{U}_m(t)) \cdot \mathbf{K}_{NL}(\mathbf{U}_f(t)) + \mathbf{K}(\mathbf{U}_f(t)) + \mathbf{B}_P\mathbf{P}(t) = \mathbf{g}(t) \quad (3.22)$$

where $\mathbf{M}$ is the mass matrix, $\mathbf{K}_{NL}(\mathbf{U}_f(t))$ is the non-linear convective term matrix, $\mathbf{K}(\mathbf{U}_f(t))$ is the diffusive term matrix, $\mathbf{B}_P$ is the matrix of the pressure gradients and $\mathbf{g}(t)$ is the known terms vector.

The numerical integration of this system can be done using the Crank-Nicolson scheme [72] by discretizing the time derivative and obtain the following form

$$\mathbf{M}\frac{\mathbf{U}_f^n - \mathbf{U}_f^{n-1}}{\Delta t} + \theta\left[(\mathbf{U}_f^n - \mathbf{U}_m^n(t)) \cdot \mathbf{K}_{NL}(\mathbf{U}_f^n) + \mathbf{K}(\mathbf{U}_f^n)\right] + \mathbf{B}_P\mathbf{P}^n =$$
$$\left[\theta\mathbf{g}(t^n) + (1-\theta)\mathbf{g}(t^{n-1})\right]$$
$$- \quad (1-\theta)\left[(\mathbf{U}_f^{n-1} - \mathbf{U}_m^{n-1}) \cdot \mathbf{K}_{NL}(\mathbf{U}_f^{n-1}) + \mathbf{K}(\mathbf{U}_f^{n-1})\right] \quad (3.23)$$

with n the time step number, Δt the time-step, and setting $\theta = 0.5$ to have the Crank-Nicolson second order implicit scheme.

An identical approach is used to integrate the $k - \varepsilon$ equations.

3.2 FEM formulation for the geometrically non-linear – finite deformation elasticity

The variational form of Eq. 2.19 is usually obtained considering the hypothesis of small perturbations with respect to the *reference* configuration. This allows to reduce the problem to a very simple set of linear algebraic equations using the FE method. If we admit that the deformation can become large and finite, it will be necessary to formulate the problem on the *current* or *deformed* configuration, in order to continue to use the model introduced in Chapter 2.

It has to be notice that the current configuration of the body is unknown and it is determined at each step of the solution problem. The non-linearity of the model arises from this last aspect as the base equations suppose linear elasticity, defining this kind of problem as geometrically non-linear.

As presented for example in [73], we can obtain the final variational form applying the Galerkin's technique to Eq. 2.19 with respect to the reference domain and then to apply the transformation from the reference to the deformed configuration.

It is possible to prove [73] that, at the end of the process, the transformation to the expressions integrated on the deformed body brings to a form that is practically identical to the small perturbation theory, except for a single term which keeps into account for the geometrical non-linearity and for the fact that, at each solution step the integration domain must be updated.

We can find the variational form, and then the FEM formulation of the structure

dynamics problem, by applying the GLS method and the FEM discretization to each term of Eq. 2.19. For a complete description of the method, please refer to [73].

Let define with capital letters the indices and variables relative to the reference configuration ($X_I \in \Omega_0$), keeping the notation of Chapter 2 for the current configuration variables ($x_i \in \Omega_t$). The variation of the Green strain tensor can be written as

$$\delta E_{IJ} = \frac{1}{2}\left(\delta u_{i,j} + \delta u_{j,i}\right) F_{iI} F_{jJ} = \delta \varepsilon_{ij} F_{iI} F_{jJ} \tag{3.24}$$

where $\delta \varepsilon_{ij}$ is the strain matrix from the deformed shape, which is identical to the small perturbation form, and $F_{iI} = \left(\delta_{iI} + u_{i,I}\right)$ are the deformation gradient components. To do not make the notation too heavy, we will omit the subscript $s - solid$ in the rest of the section.

Defining J as the Jacobian determinant of the deformation gradient, it is possible to write the transformation from the Kirchhoff stress τ_{ij} to the Cauchy stress in current configuration as

$$\tau_{ij} = J\sigma_{ij} \tag{3.25}$$

Using Eq. 3.24 and 3.25 we can obtain the variational form of the stress-strain term of Eq. 2.19 as

$$\delta E_{IJ} S_{IJ} = \delta \varepsilon_{ij} \sigma_{ij} J. \tag{3.26}$$

Integrating the expression on the reference domain and then making the transformation on the integral, we can obtain

$$\int_{\Omega_0} \delta \varepsilon_{ij} \sigma_{ij} J d\Omega_0 = \int_{\Omega_t} \delta \varepsilon_{ij} \sigma_{ij} d\Omega_t \tag{3.27}$$

From the last expression, we can obtain the matrix form of the discretized equations applying the FE technique. Let N_n be the element shape function defined at node n. It can be demonstrated that

$$\int_{\Omega_t} \delta \varepsilon_{ij} \sigma_{ij} d\Omega_t = \delta \mathbf{u}^T \int_{\Omega_t} \mathbf{B}^T \sigma d\Omega_t \tag{3.28}$$

where the matrix $\mathbf{B}$ can be obtained from Eq. 3.24, by applying the finite element description of the displacement

$$u_i = \sum_a N_a(\xi) U_i^a \tag{3.29}$$

in which ξ are the parametric space variables of definition of N_a and U_i^a is the nodal displacement.

In the geometrically non-linear case $\mathbf{B} = \mathbf{B}_0 + \mathbf{B}_G^{NL}$ and it is possible to demonstrate that $\mathbf{B}_0$ is the same that can be obtained in the linear case for small perturbation, while the non-linear part $\mathbf{B}_G^{NL}$ defines the non-linearity due to the deformation.

The same procedure can be applied to the other two terms (inertial and external
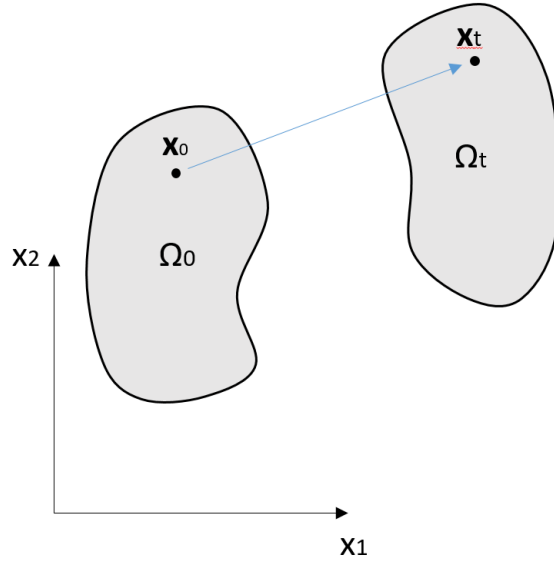
FIGURE 3.1: Reference and deformed configuration of the structure domain

forces) of Eq. 2.19 to obtain the residual in variational form

$$\int_{\Omega_t} \delta \varepsilon_{ij} \sigma_{ij} d\Omega_t + \int_{\Omega_t} \delta u_i \rho \ddot{u}_i d\Omega_t - \int_{\Omega_t} \delta u_i \rho f_i d\Omega_t - \int_{\partial \Omega_t} \delta u_i t_I ds = 0 \qquad (3.30)$$

Recalling again the FE description, we can arrive to the final matrix form of the problem

$$\mathbf{f}_a - \mathbf{K}_{ab} \mathbf{U}^T - \mathbf{M}_{ab} \ddot{\mathbf{U}}^T = 0 \qquad (3.31)$$

where $\mathbf{f}_a$, $\mathbf{K}_{ab}$ and $\mathbf{M}_{ab}$ are respectively the generalized force vector, the stiffness matrix and the mass matrix of the FEM problem, defined as

$$\mathbf{f}_a = \int_{\Omega_t} N_a \rho \mathbf{f} d\Omega_t + \int_{\partial \Omega_t} N_a \mathbf{t} ds \qquad (3.32)$$

$$\mathbf{K}_{ab} = \int_{\Omega_t} \mathbf{B}_a^T \mathbf{D} \mathbf{B}_b d\Omega_t + G_{ab} \mathbf{I} = \int_{\Omega_t} \mathbf{B}_a^T \mathbf{D} \mathbf{B}_b d\Omega_t + \int_{\Omega_t} N_{a,i} \sigma_{ij} N_{b,i} d\Omega_t \mathbf{I} \qquad (3.33)$$

$$\mathbf{M}_{ab} = \int_{\Omega_t} N_a \rho N_b d\Omega_t \mathbf{I} \qquad (3.34)$$

Equation 3.33 implies the definition of the two terms of matrix $\mathbf{B}$. In particular, the G_{ab} terms define the geometric non-linear part.

3.2.1   Time integration scheme – Generalized α

The Generalized-α method proposed by Chung and Hubert [74] is used to obtain a stable time integration scheme for the structure dynamic equations.

Applying the procedure of [74] to Eq. 3.31, and solving with respect to the nodal

displacement increment vector, we can obtain the following implicit system

$$
\begin{aligned}
[(1-\alpha_F)\mathbf{K}+k_M\mathbf{M}]\Delta\mathbf{U}^n = \\
-\quad \mathbf{K}\mathbf{U}^{n-1}+\mathbf{M}(k_{Mv}\dot{\mathbf{U}}^{n-1}+k_{Ma}\ddot{\mathbf{U}}^{n-1})-\left[(1-\alpha_F)\mathbf{f}^n+\alpha_F\mathbf{f}^{n-1}\right]
\end{aligned}
\quad (3.35)
$$

$$(3.36)$$

which is completed by the explicit updating step

$$
\ddot{\mathbf{U}}^n = \frac{1}{\beta\Delta t^2}(\Delta\mathbf{U}^n - \dot{\mathbf{U}}^{n-1}\Delta t - (0.5-\beta)\Delta t^2\ddot{\mathbf{U}}^{n-1}); \quad (3.37)
$$

$$
\dot{\mathbf{U}}^n = \dot{\mathbf{U}}^{n-1}+(1-\gamma)\Delta t\ddot{\mathbf{U}}^{n-1}+\gamma\Delta t\ddot{\mathbf{U}}^n; \quad (3.38)
$$

$$
\mathbf{U}^n = \mathbf{U}^{n-1}+\Delta\mathbf{U}^n; \quad (3.39)
$$

with the scheme constants defined as follows

$$
\gamma = 0.5 + \alpha_F - \alpha_M; \quad (3.40)
$$

$$
\beta = 0.25(1+\alpha_F-\alpha_M)(1+\alpha_F-\alpha_M); \quad (3.41)
$$

$$
k_M = \frac{1-\alpha_M}{\beta\Delta t^2}; \quad (3.42)
$$

$$
k_{Mv} = \frac{1-\alpha_M}{\beta\Delta t}; \quad (3.43)
$$

$$
k_{Ma} = \frac{1-\alpha_M-2\beta}{2*\beta}; \quad (3.44)
$$

$$(3.45)$$

where α_F and α_M are opportunely defined in order to guarantee the stability and maximum convergence order.

3.3 FEM formulation of the moving mesh equations

We report here the FE formulation discussed in [75] for the moving mesh solution. Let define the finite element trial and test function spaces as $\mathscr{S}^h = \{u_m^h | u_m^h \in [H^{1k}(\Omega)]^{n_{sd}}, u_m^h = g^h \text{ on } \Gamma_g\}$ and $\mathscr{V}^h = \{w^h | w^h \in [H^{1k}(\Omega)]^{n_{sd}}, w^h = 0 \text{ on } \Gamma_g\}$, with $H^{1k}(\Omega)$ the finite-dimensional function space on Ω. Then the Galerkin's formulation of Eq. 2.25 can be written as

$$
\int_\Omega \boldsymbol{\varepsilon}_m(\mathbf{w}^h):\boldsymbol{\sigma}_m(\mathbf{u}_m^h)d\Omega = \int_{\Gamma_h}\mathbf{w}^h\cdot\mathbf{h}_m d\Gamma \quad (3.46)
$$

considering that the force vector can be supposed zero for a moving mesh problem. As introduced in Chapter 2, this method has the peculiarity to keep the mesh quality properties in the refinement zones, which is a very important property in case of turbulent flow calculations. The *Jacobian-based stiffening*, first proposed in [76] and then improved in [75], allows this capability by modifying the element equivalent stiffness with a term proportional to the cell Jacobian. In particular, if a general

integral term is expressed in the FE discretization as

$$\int_\Omega [...]d\Omega = \sum_e \int_\Sigma [...]^e J^e d\Sigma \tag{3.47}$$

with $J^e = det(\partial x/\partial \xi)^e$, the element stiffness alteration occurs as follows

$$\int_\Sigma [...]^e J^e d\Sigma \rightarrow \int_\Sigma [...]^e J^e \left(\frac{J^0}{J^e}\right)^Z d\Sigma. \tag{3.48}$$

With J^0 a constant dependent on the characteristic size of the problem and Z an exponent that we will put equal to 1 for all the computations. For further detail and test cases, see [75, 76].

3.4 Discretized particle equations

In the discretized particle equations, ensemble averaging is carried out over the discretized cloud domain $\Omega_c = \bigcup_{e=1}^{n_{elc}} (\Omega_c)_e$, where $(\Omega_c)_e$ is the cloud element, and n_{elc} is the number of elements. The cloud elements come from a fixed mesh, which we call "particle mesh," and consist of the elements of that fixed mesh within the radius 3σ (with σ defined as in Eq. 2.41). With that, the discretized version of ensemble averaging is written as

$$\langle \theta \rangle^h = \frac{\sum_{e=1}^{n_{elc}} \int_{(\Omega_c)_e} \theta PDF(\mathbf{x},t)d\Omega}{\sum_{e=1}^{n_{elc}} \int_{(\Omega_c)_e} PDF(\mathbf{x},t)d\Omega}, \tag{3.49}$$

where the element-level integration is performed by Gaussian quadrature.

3.4.1 Trajectory calculation

Spatially-discretized version of Eq. (2.39) is written as

$$\frac{d\mathbf{v_c}^h}{dt} = \mathbf{a}_c^h, \tag{3.50}$$

where

$$\mathbf{a}_c^h = C_D' \| \langle \mathbf{u} \rangle^h - \mathbf{v}_c^h \| \left(\langle \mathbf{u} \rangle^h - \mathbf{v}_c^h \right) + \langle \mathbf{f} \rangle^h + \left(1 - \frac{\rho}{\rho_p}\right) \mathbf{g}. \tag{3.51}$$

Time discretization of Eq. (3.50) is done with a predictor–multicorrector algorithm.

Predictor stage:

$$(\mathbf{v}_c^h)_{n+1}^0 = (\mathbf{v}_c^h)_n + (\mathbf{a}_c^h)_n \Delta t. \tag{3.52}$$

Multicorrector stage:

$$(\mathbf{v}_c^h)_{n+1}^{i+1} = (\mathbf{v}_c^h)_n + \left((\mathbf{a}_c^h)_n + (\mathbf{a}_c^h)_{n+1}^i\right)\frac{\Delta t}{2}. \tag{3.53}$$

Here the subscript n is the time level, and the superscript i is the counter for the multiple corrections. We stop the corrections when

$$\frac{(\mathbf{v}_c^h)_{n+1}^{i+1} - (\mathbf{v}_c^h)_{n+1}^{i}}{(\mathbf{v}_c^h)_{n+1}^{i+1}} \leq 2 \times 10^{-2}. \tag{3.54}$$

At each time step, the PCT model requires the computation of the cloud mean position and radius, and the identification of the elements contained within the cloud volume. This is done with the search algorithm described in [77].

3.5 XENIOS^{++} / FSI-Module: Block-iterative strong coupling algorithm for computational fluid-structure interaction problems

The FSI solution is obtained through a strongly coupled, segregated solution method. The strong coupling between the four systems (ALE-URANS, $k - \varepsilon$, structure dynamics and mesh motion) is achieved by enforcing the consistency at the interface and between the coupled quantities between different systems, iterating internally to the time-step until to reach the convergence on all the system residuals.

We can define three main loops, the time loop to solve the unsteady problem, the outer non-linear loop to solve the implicit coupled systems, and the inner solutions of the linearized forms. Figure 3.2 shows the flow-chart of the algorithm.

At each time step, the solver executes the following:

- Solution of the ALE-URANS equations loading the time-step mesh velocities $\mathbf{v}_m$ and enforcing from the previous non-linear iteration or time-step (if it is the first iteration) the solid velocity as boundary flow velocity. Let $\Gamma_{i_f} = \Gamma_{i_s} = \Gamma_i$ be the interface domain between the solid and the fluid, the interface condition for the fluid can be written as

$$\mathbf{u}_f - \mathbf{v}_s = 0, \quad on \quad \Gamma_i \tag{3.55}$$

  The turbulence variables values are obtained from the previous iteration or time-step (if it is the first non-linear iteration).

- Solution of the two-equation turbulence system, using the field variables already computed.

- Solution of the structure dynamic system, applying the aerodynamic traction vector at the interface

$$\boldsymbol{\sigma}_s \cdot \mathbf{n} - \mathbf{h} = 0, \quad on \quad \Gamma_i \tag{3.56}$$

Here $\mathbf{h} = \boldsymbol{\sigma}_f \cdot \mathbf{n}$ and $\mathbf{n}$ is the unit vector normal to the interface surface.

3.5. XENIOS^{++} / FSI-Module: Block-iterative strong coupling algorithm for computational fluid-structure interaction problems

39

- Updating of the explicit variables such as the structure velocity and acceleration.

- Iteration until the convergence on the total residual norm is achieved

- Solution of the mesh motion imposing the local displacement on Γ_i

- Explicit computation of the mesh velocity
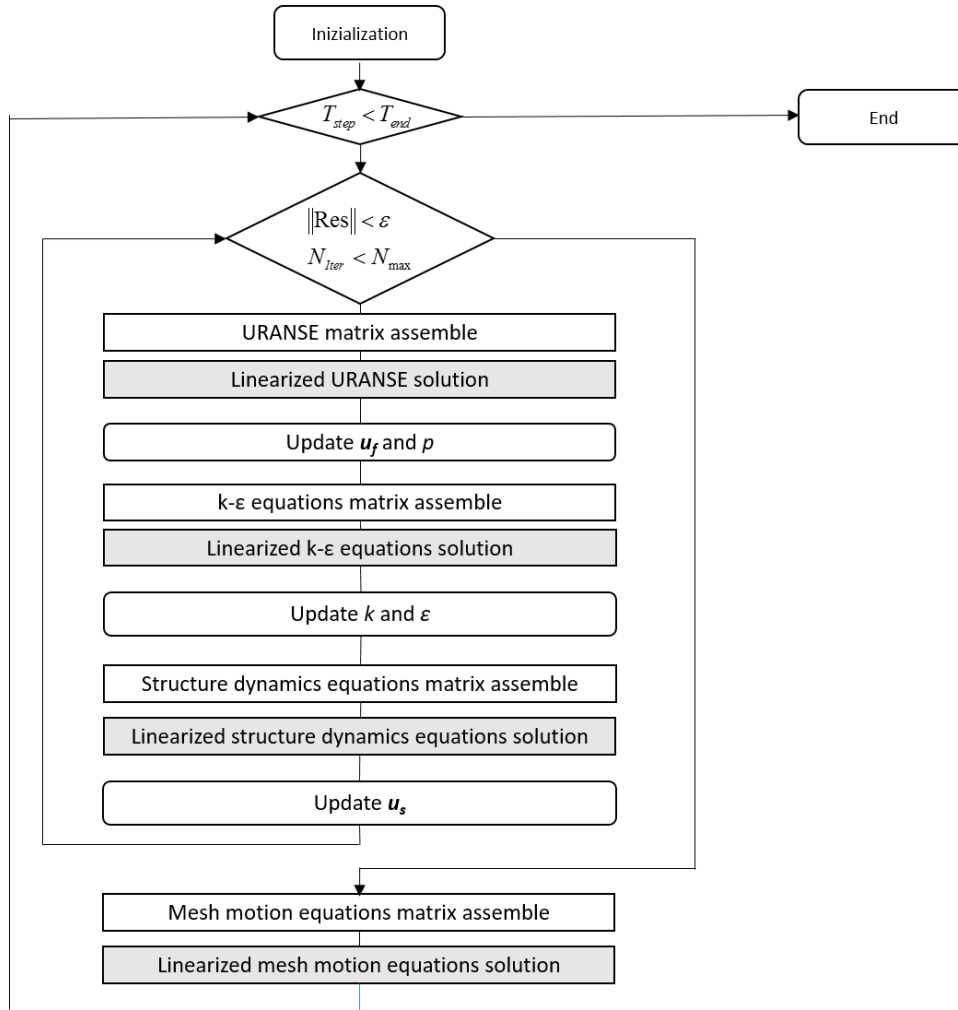
FIGURE 3.2: Rationale of the FSI algorithm

In this algorithm we can find the two logics introduced above, indeed, the solution procedure can be considered **segregated** as we solve separately in the non-linear loop the main physical systems ($N-S$, $k-\varepsilon$, *Elasticity*), but also **block-iterative** because we move the mesh at the end of the convergence problem. In theory, to obtain the best consistency with fluid-structure interaction problems, we should use a full monolithic approach, which solves all the equations together, also for the mesh motion. However avoiding this further non-linearity produces more stable and convergent solutions as the Jacobian of the cell is not changing during the solution of the physical systems.

The domain is composed by a single mesh in which the solid and fluid elements are defined in the solver with different physical properties and for which different finite element matrices are assembled. This approach results in an automatic management of the interface in the case of automatic domain decomposition for parallel computation. This approach is to not confuse with the immersed boundary approach, indeed, here the boundary is well defined in the mesh and the mesh moves following the structure displacement.

The inner linear solution of the matrix systems is done using the GMRES solver provided in the open source PETSC library. We use XENIOS++ code, self-produced by our research group, for all the computations. Appendix A reports the result for a validation test of the solver.

3.6   MASAI Interface for erosion with adapted geometry problems

As reported also in the introduction, it is difficult to find applications and references on numerical solvers that predict the erosion due to particle-laden flows and, at the same time, update the eroded surface and calculation domain for the aerodynamic solution.

The MaSAI algorithm, written in FORTAN 95, has been developed in order to sequentially perform three different analysis:

1. A CFD analysis to investigate the flow stream;

2. A PCT analysis to obtain the erosion data;

3. A Moving Mesh analysis to evaluate the displacement of the eroded boundary and re-mesh the domain accordingly.

Figure 3.3 shows the scheme of the algorithm. MaSAI starts acquiring the reference numerical domain and the initial and boundary conditions. Once the geometry is defined, MaSAI (Multiphase Solver and Adaptive-mesh Interface) launches the CFD solver of XENIOS. As the flow field is computed than the PCT solver PC-Track [7] starts and assumes that flow field as an input. At the end of PC-Track simulation, the erosion pattern is known and MaSAI computes the displacement of the grid nodes. Since for very small displacements the variations in flow field are negligible, we set a minimum erosion displacement (e_{lim}) below which both the grid and flow field are unaffected by the erosion. At each iteration MaSAI evaluates the maximum erosion displacement (e_{max}) and computes the scale factor. Multiplying the predicted erosion displacements by we are sure that at each iteration the maximum value of eroded material always equals e_lim, thus avoiding the issue of non-linear time-dependent phenomena. This of course results in a contraction/expansion of the actual simulated time at each MaSAI step.

The computed erosion displacements are then applied to the grid and the Adaptive

Mesh code of XENIOS provides a new grid accounting for the eroded geometry. Thanks to this operation, the flow field varies as the erosion process evolves and the geometry of the target body changes. Then, the erosion prediction varies according to the changing flow field. The simulation can be kept running since an exit condition occurs. The exit condition can be set in terms of both maximum simulated time and maximum eroded material, thus providing an extremely flexible tool.
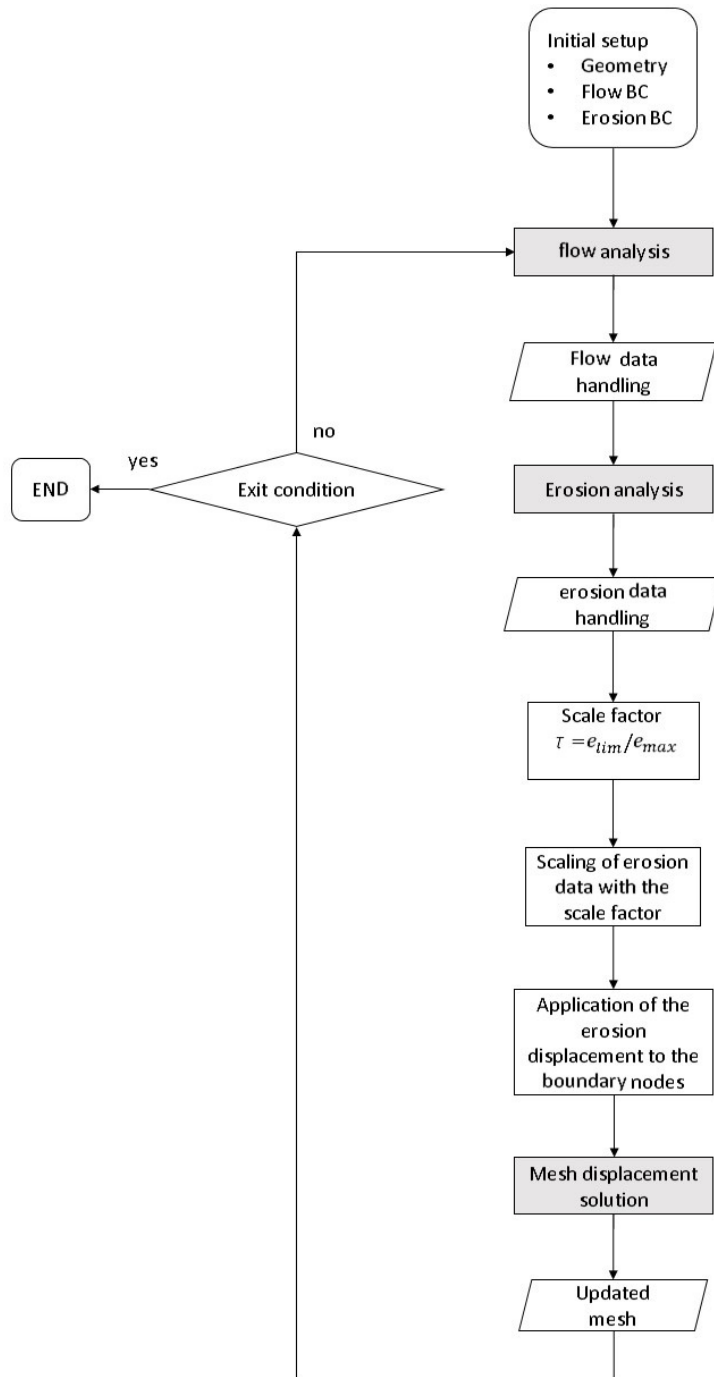
FIGURE 3.3: Rationale of the MaSAI algorithm

Chapter 4

Passive control of performance and load with morphing geometries

4.1 Performance improvement on wind turbine section

During the last twenty years, the development process on wind turbines implied an increment in the size of the rotor. As an effect of this, the maximum operating turbine size reaches 5-6 MW in nominal power, with blade length of 60 or more meters. These particular dimensions are designed especially for offshore applications, because of the transportation problem associated to large structures.

Considering this rotating system, phenomena directly involved with the life cycle and performance evolution are not simple to be predicted and the current experience does not allow to know in advance how these structures behave over long periods. The main factors that influence the velocity at the rotor blades are:

- Atmospheric boundary layer;

- Small turbulent scale fluctuation;

- Wind gusts;

- Interaction between fluid and rotor blade.

The relative aerodynamic field resulting from these phenomena is unsteady, and it presents a variable inflow velocity, which involves a variation of the angle of attack at the section level, connected to a variation of the aerodynamic load. This fluctuation produces a fatigue load on the blade, but also inside the structural components of the wind turbine, as the transmission system. This aspect is relevant also in terms of expected rotor performance; in fact, the aerodynamic surface is usually designed with BEM methods, which take into account mainly the steady behaviour of the airfoils.

A possible solution that can be useful for damping these oscillations and better managing the flow variability is to use a variable geometry, based on a concept of

smart blade (see for example [78, 79]).

We present here a numerical study on the active and passive trailing edge morphing. In particular, the study focuses on the aerodynamic response of a midspan blade section, in terms of FSI and driven surface deformation. The work of this section is an updated version of the work published in [80].

In order to contextualize the 2D problem, we used as flow condition the local aerodynamic quantities recorded for the same section, using the NREL wind turbine simulator FAST, applied to simulate the 5MW NREL wind turbine.

The two systems (active and passive control) have two different operating logic, thus they require to be evaluated in two different conditions. We simulate the passive system in a turbulent wind, while the active system follows a simple start-up procedure.

The passive system is modelled and solved through the FSI algorithm. The active morphing is simulated using the same model described above, but imposing a time-varying deformation of the trailing edge surface, so in this case the FSI does not account for the structure dynamics as it is an external constraint of the solution.

4.1.1 Turbine description

The definition of the baseline wind turbine used as base in this work is reported in [81] and corresponds to the 5 MW HAWT designed by the National Renewable Energy Laboratory. Table 4.1 summarizes the main characteristics of the wind turbine, while Table 4.2 reports the baseline blade properties.

Table 4.3 illustrates the aerodynamic design of the blade using the AeroDyn [82] nomenclature. The blade node locations, labelled as "RNodes", are directed along the blade-pitch axis from the rotor centre (apex) to the blade cross sections. The element lengths, "DRNodes", sum to the total blade length of 61.5 m, divides the wind turbine in 17 section. "DU" class of airfoil refers to Delft University and "NACA" refers to National Advisory Committee for Aeronautics.

4.1.2 Reference airfoil

In a wind turbine blade, the midspan sections are critical because they contribute (as the tip region) to the performance, but they also experience an oscillation of the relative wind due to the turbulence. This effect is greater than the effect that the wind turbulence has on the tip region, making the mid region more subjected to aerodynamic load vibrations. Furthermore, we focus the solution on a two-dimensional view. This is the reason why it is not possible to obtain accurate results, when this solver is applied on the innermost and outermost regions, which are characterized by the presence of secondary flows. These motivations led towards a reference airfoil located in the mid-tip span region, and in particular, located on the 12th nodal position of Table 4.3. At this position, we can find a NACA 64517

airfoil, with a local relative velocity that can be extracted from the strip theory calculation.

Rating	5 MW
Rotor orientation, configuration	upwind, 3 blades
Control	variable speed, collective pitch
Rotor, hub diameter	126 m, 3m
Hub height	90 m
Cut - in, rated, cut – out wind speed	3 m/s, 11.4 m/s, 25 m/s
Cut – in, rated rotor speed	6.9 rpm, 12.1 rpm

TABLE 4.1: Turbine data

Length	61.5 m
Overall mass	17740 kg

TABLE 4.2: Blade data

Node (-)	RNodes (m)	DRNodes (m)	Chord (m)	Airfoil Profile (m)
1	2.8667	2.7333	3.542	Cylinder
2	5.6000	2.7333	3.854	Cylinder
3	8.3333	2.7333	4.167	Cylinder
4	11.7500	4.1000	4.557	DU40-A17
5	15.8500	4.1000	4.652	DU35-A17
6	19.9500	4.1000	4.458	DU35-A17
7	24.0500	4.1000	4.249	DU30-A17
8	28.1500	4.1000	4.007	DU25-A17
9	32.2500	4.1000	3.748	DU25-A17
10	36.3500	4.1000	3.502	DU21-A17
11	40.4500	4.1000	3.256	DU21-A17
12	44.5500	4.1000	3.010	NACA64-A17
13	48.6500	4.1000	2.764	NACA64-A17
14	52.7500	4.1000	2.518	NACA64-A17
15	56.1667	2.7333	2.313	NACA64-A17
16	58.9000	2.7333	2.086	NACA64-A17
17	61.6333	2.7333	1.419	NACA64-A17

TABLE 4.3: Blade sections data

4.1.3 Active case analysis

We are interested in the performance estimation of the starting manoeuvre of the wind turbine, related to an application of an active morphing concept, applied on the trailing edge of the airfoil.

We superimpose the trailing edge deformation as a function of the expected relative wind velocity. The deformation was achieved through a simple parabolic shape function applied to the trailing edge coordinates.

The active morphing process starts from the full-deformed configuration, corresponding to the cut-in relative wind speed, and finishes in the undeformed configuration at the nominal relative wind speed. The section is subjected to the velocity path reported in Figure 4.2, characterized by a relative wind starting velocity from 5 m/s (rotor stopped and cut-in wind velocity), to reach the nominal operating point condition linearly.

During the evolution process, the angle of attack has been kept constant, exploiting the variable speed control system, reported in Table 4.1. In this way, it is possible to preserve similar triangle input speed of the wind turbine. Figure 4.1 shows the morphing process evolution. The airfoil trailing edge area was rotated by 3 degrees as to increase the camber. In this case, the trailing edge deflection rate is considered constant.
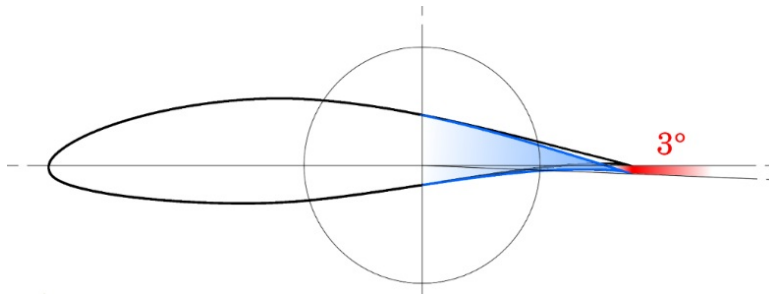

FIGURE 4.1: Active morphing, configuration at t = 0 s.
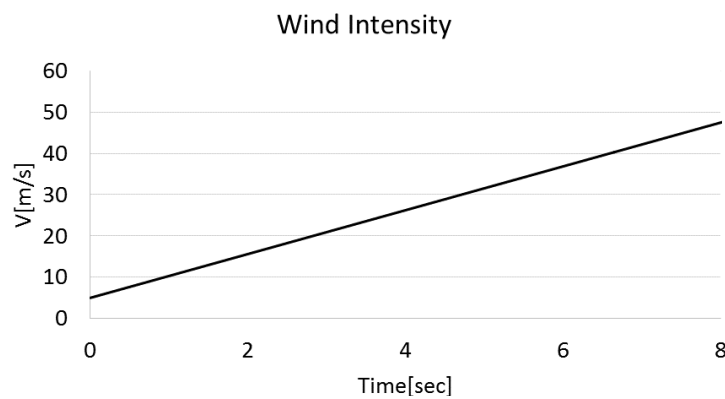
FIGURE 4.2: Relative wind velocity considered in the start-up case

4.1.4 Passive case analysis

In the passive control case, we want to estimate the response of the trailing edge morphing system, when the airfoil is subjected to a variable input velocity, which simulates the typical turbulence scenario in the nominal operating point of the wind turbine.

The turbulence simulator TurbSim [83] is used to obtain the wind input for FAST
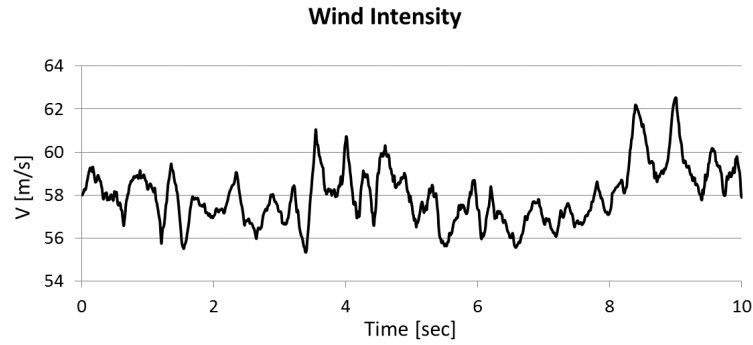
Wind Intensity

FIGURE 4.3: Section relative wind velocity, computed for the passive morphing case
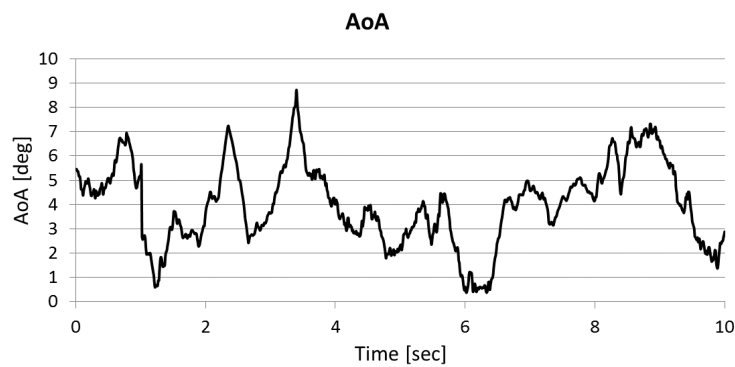
AoA

FIGURE 4.4: Section angle of attack, computed for the passive morphing case.

[1] in order to obtain the local aerodynamic quantities corresponding to an IEC-NTM (Normal Turbulence Model) [84]. After that, we take the relative wind velocity magnitude (Figure 4.3) and local angle of attack (Figure 4.4) at the corresponding section. Finally, we applied this velocity profile using a tabular velocity input at the inlet boundary of the CFD domain.

4.1.5 Fluid mesh and boundary conditions

The adopted grid is an "O-type" construction with an average radius of about 80 chords. In this way, it is possible to identify two different areas with different boundary conditions. In the specific, there will be a fixed-wall and a moving-wall region on the airfoil surface, the last one starting from the 60 % of the chord length until the trailing edge. The mesh domain counts 2.1E+04 hexahedral cells assembled in a structured way. The coupled interface is characterized by a y+ dimension of 1.

Standard boundary conditions were applied to the RANS computations of incompressible flow (Table 4.4).

Inflow	V0 = 12 m/s; TI = 5%
	Time varying velocity (IEC-NTM)
Outflow	Zero gradient
Fixed wall	No-slip condition
Moving wall	No-slip condition
Radial far field	Zero gradient

TABLE 4.4: Fluid phase boundary conditions.

4.1.6 Solid mesh and boundary conditions

For this application, a lower order model for the structure dynamic is used to simulate a geometry similar to what proposed in literature. The morphing structure can be solved as a truss structure, modelled with mono-dimensional linear bar elements. The inside part of the airfoil profile was modelled through the frame structure shown in Figure 4.6.

We applied different mechanical properties to obtain an automatic response in term of displacement, considering the induced stresses generated on the airfoil by external conditions. In this way, the airfoil is able to adapt the trailing edge configuration in order to minimize the load magnitude in this area.

We choose the mechanical properties of the solid elements such as to avoid flutter instabilities and deformations magnitude out of the linear deformation field:

- Isotropic material

- Young Modulus: 2 GPa

- Material Density: 1500 kg/m3

- Element Section Area: 0.01 – 0.05 m

It is possible to observe that these properties can be easily obtained with a particular polymeric material, which are of common use in wind turbine technology.

The structure is constrained imposing a zero displacement at the two leftmost nodes.
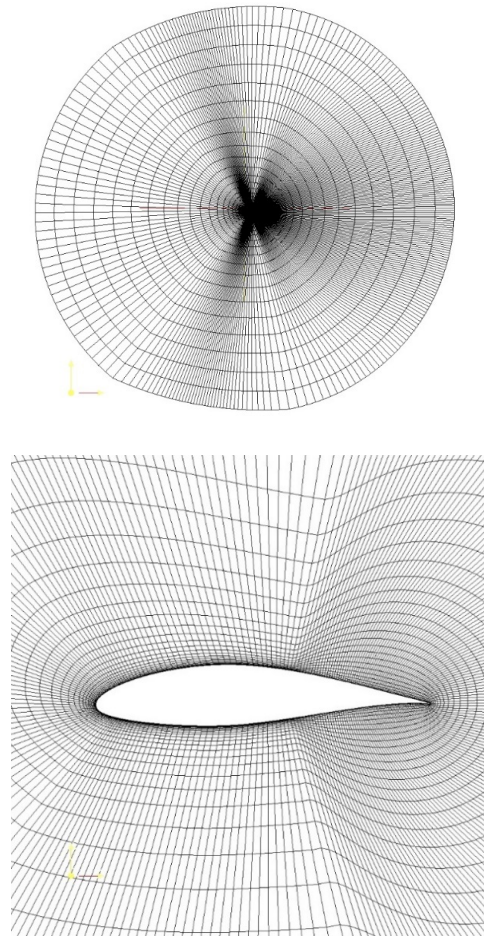
FIGURE 4.5: Fluid computational domain.
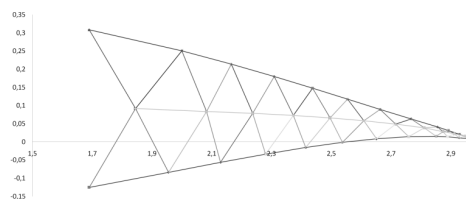
FIGURE 4.6: Frame structure applied for the trailing edge.

4.1.7 Results

It is possible to observe the results in terms of the main aerodynamic parameters. Figure 4.7 shows the final comparison in terms of lift coefficient, drag coefficient and their ratio between the standard (rigid) and the morphed configuration of the airfoil in the active case. As expected, the lift coefficient trend for the morphed configuration stands at higher levels than the standard. This difference tends to fade near the nominal operating point, where the airfoil curvature returns toward the original configuration. The drag coefficient trends, in the morphed and standard configuration, are comparable. This is the reason why the aerodynamic efficiency,

defined as the ratio CL/CD, assumes a higher value in the morphing configuration. We must observe before analyse the passive case results that, since the structural model is a linear model, the material and structure choice must be such that the maximum elements deformation is limited to the linear field (small deformations). Figure 4.8 shows the result of the lift coefficient for the passive case. As expected, the morphed and the standard configuration show a comparable trend. This is due to the limited area assigned to the morphing process, limited only in trailing edge airfoil region. The main difference in lift production is observable in terms of oscillation amplitude. However, also for this application we can note a decrease in term of drag coefficient, as shown in Figure 4.8.

Figure 4.8 reports also the aerodynamic efficiency; the morphing configuration in this case can be more efficient than the original airfoil. We choose to represent a half-second window in this case because of the high frequency associated to the unsteady aerodynamic solution.
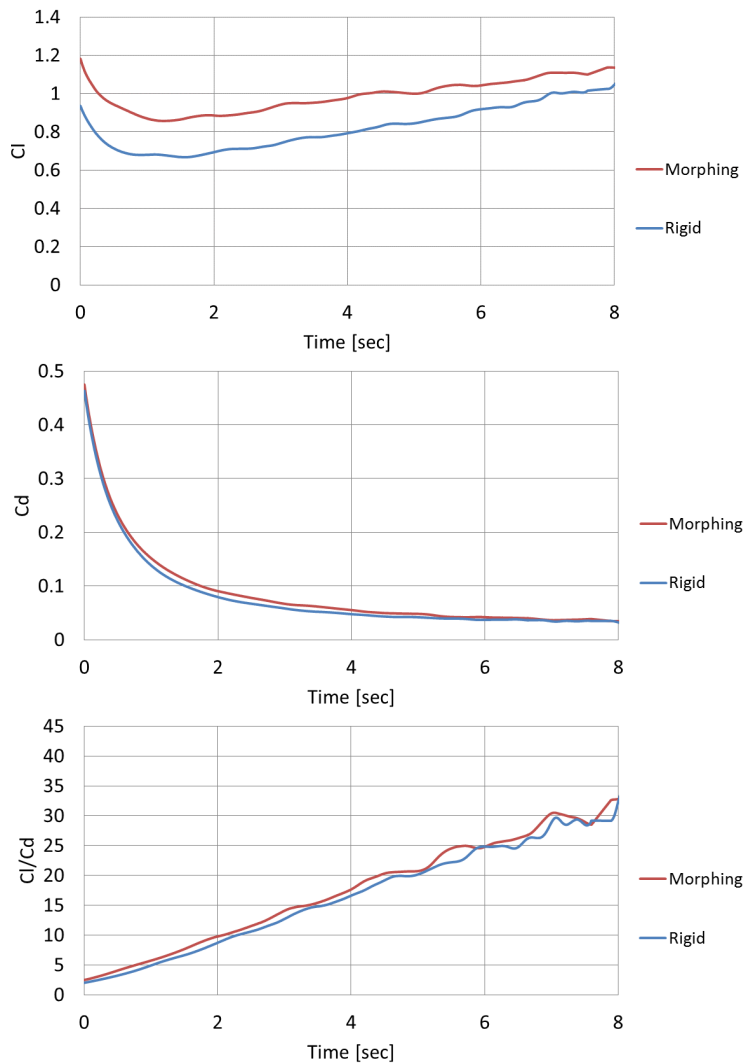

FIGURE 4.7: Active case, aerodynamic coefficients.
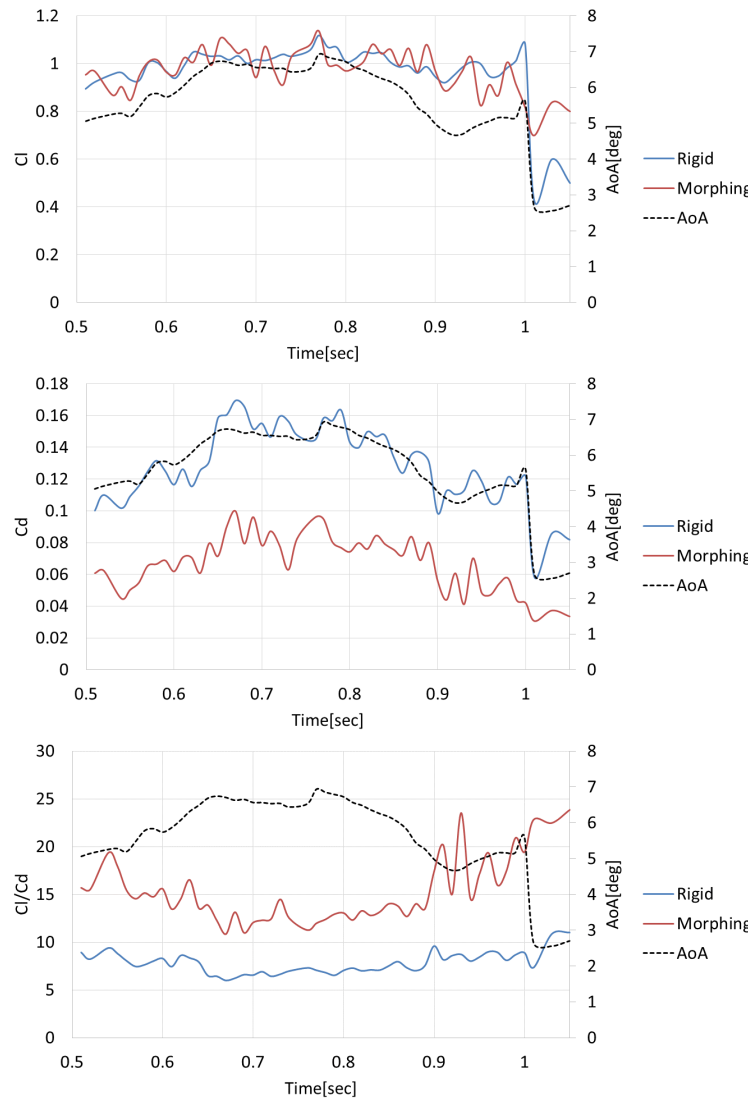
FIGURE 4.8: Passive case, aerodynamic coefficients

4.1.8 Conclusions

We investigated the effect that an active and a passive trailing edge morphing control could have on a section of a large wind turbine.

In order to have an indication of this effect, we chose to simulate the turbine conditions, which we expect are the most significant for the application of these two ways of control. In particular, we simulate a symbolic start-up manoeuvre for the active case, and a normal turbulence at the rating wind velocity for the passive case. The study produces the following results:

- Active morphing: in the start-up procedure, the morphed airfoil produces a greater aerodynamic efficiency, as effect of the greater lift coefficient.

- Passive morphing: during the power production state, in normal turbulence conditions, the drag of the morphing airfoil is less than the rigid section case.

This can be translated in a potential increment in blade torque.

Using a FEM solver based on linear beam elasticity for the structural displacement, the solution has a limitation on the displacement magnitude. A possible future development can be to study the effect of a big deformation structure, which can be probably useful in terms of vibrational load reduction. This improvement will be applied to the study of a similar system on axial fan blades, which is the topic of the next two sections.

4.2 Passive morphing control system for fan blades - 2D study

Large fan systems used in tunnel and metro ventilation are usually subjected to a range of different operating conditions. In this range, the flow rate, the fan velocity but also the inlet flow direction, vary, leading the fan to operate far from the rating design point. Furthermore, in real application the flow at the inlet is not uniform and of not constant velocity, as an effect of the unsteady nature of a real flow field, and due for example to the presence of near structures and other obstacles. In these off-design conditions, the fan rotor is subjected to vibrational loads and loss in performance.

For this kind of product, the development of an active control system to reduce the negative effects in off-design and unsteady inlet conditions is not a practicable way. Conversely, passive systems always represent an interesting solution for their constructive simplicity and low costs.

The system we have applied and tested is a passive control based on the aeroelastic deformation, applied at the trailing edge of the blade. This solution is based on something already presented and studied for aircrafts (e.g. [85, 86]), where the elastic and morphing trailing edge is used to reduce the aerodynamic drag and noise. It was also adopted and for wind turbines [22, 87, 88], where the application of a deformable trailing edge is supposed to be useful to reduce the vibrational loads, noise and efficiency losses, due to the random nature of the turbulent wind. Other applications can be found in [89, 90, 79].

The study presented in this section refers to the work published in [91].

4.2.1 Fan and blade description

As base of all the computations, we take the geometry and flow conditions of the FLÄKT WOODS 224JMTS, which is a reversible large axial fan for tunnel ventilation. Table 4.5 reports the fan main characteristics.

We choose a reversible fan because we would to test the control system evaluating its effect especially on the stall and off-design loads, and a reversible airfoil has a greater attitude in manifesting stall and flow separations. The choice is also

related to the availability of experimental data of the overall aerodynamic performance

Figure 4.9 shows the problem set-up with respect to the blade geometry. We take as reference to obtain the cascade, the section at r = 0.99 m (88 % of the fan radius). In this way, we are far from both the tip region and the hub region, reducing the most than possible the error due to neglect the three-dimensional aerodynamic effects.

The domain is obtained from the section extracted as in Figure 4.9. The cascade has a local pitch of 388.8 mm, the section cord c is 210 mm long and forms an angle θ of 20 degrees with the disc plane.
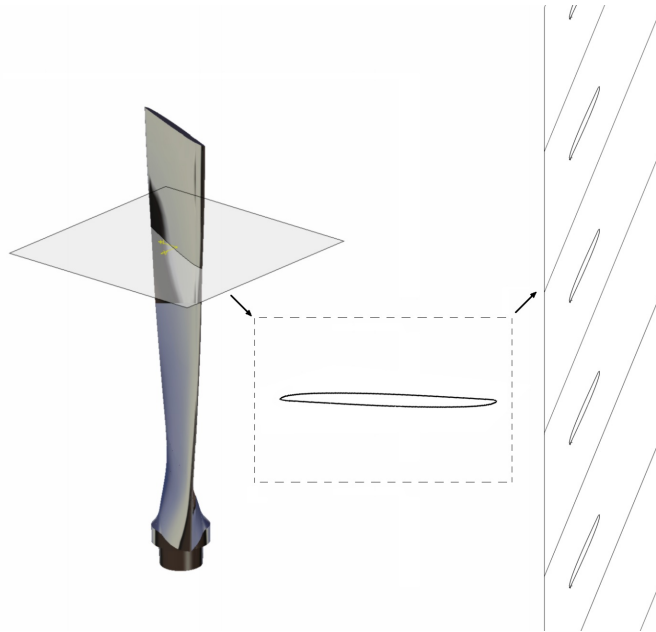
FIGURE 4.9: Reference blade and section.

Fan model	224JMTS
Fan diameter	2.240 m
Hub diameter	0.8 m
Blade radius	0.72 m
Tip gap	0.009 m
Tip chord	0.21 m
Hub chord	0.26 m
Base section thickness	0.06 m
Tip section thickness	0.012 m
Number of blades	16
Nominal speed	985 rpm
Nominal power	192 kW

TABLE 4.5: Fan characteristics.

Length	0.05 m
Thickness	0.001 m
Young modulus	300 MPa
Poisson coefficient	0.4
Density	1000 kg/m^3

TABLE 4.6: Flexible trailing edge extension characteristics.

4.2.2 Elastic trailing edge device

To simulate a flexible extension of the trailing edge we use a rectangular bar with the geometrical and mechanical properties listed in Table 4.6. The density and stiffness are such as to obtain a finite deformation under the assumed flow conditions, but avoiding flutter instabilities. The chosen properties can be obtained using a polymeric material. The material is assumed isotropic and with uniform density.

4.2.3 Computational domain and boundary conditions

Figure 4.10 and 4.11 show some details of the computational domain used to simulate the cascade. The inlet boundary is one cord far from the leading edge while the outlet is at two cords of distance from the trailing edge (along the cord direction). The cascade condition is imposed by making periodic the two lateral edges.

The grid is of structured type, made by linear quadrilateral elements, Table 4.7 reports the domain characteristics. As the turbulent solver use a low-Reynolds model, the y^+ at wall is 1.

The overall implicit equation system, solved by the non-linear solver, is composed by 121460 degrees of freedom, considering the 9 degrees of freedom for each node ($\mathbf{u}_f$, p, k, ε, $\mathbf{u}_s$, $\hat{\mathbf{u}}$). Table 4.8 reports the boundary condition for the four systems.

The single grid approach allows to switch on and off the presence of the elastic bar, by simply communicating to the solver which elements are fluid and which are solid.

4.2.4 Test set-up

We investigate the effect of the application of the elastic device on three operating conditions. These test conditions are based on experimental data, relative to blade load tests conducted by the fan manufacturer. All the experimental data and fan information have been used by courtesy of Fläkt Woods Ltd (UK) and obtained via private communication.

Table 4.9 reports the specifications of the three test cases. TEST 1 corresponds to a minimum load condition; TEST 2 corresponds to the point of maximum total efficiency of the fan; while TEST 3 corresponds to the case in which the maximum load on the blade was recorded during the experimental tests.
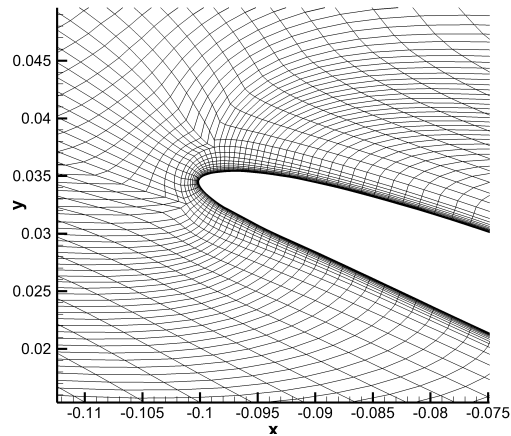
FIGURE 4.10: Detail of the grid (leading edge).

Considering the relative flow velocity, the Reynolds number at the inlet varies from 1.43E+06 to 1.45E+06, while the maximum Mach number is 0.33, justifying the assumptions of turbulent incompressible flow.
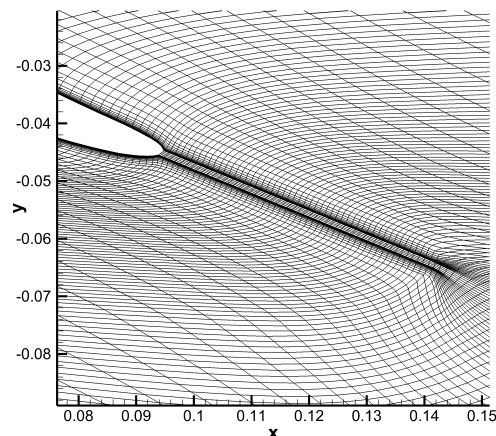
FIGURE 4.11: Detail of the grid (morphing surface).

Element type	QUAD4
Total number of nodes	17685
Total number of elements	17296
Fluid elements	17096
Solid elements	200
Wall nodes	305
Interface nodes	105
Average y^+ at wall	1

TABLE 4.7: Computational domain characteristics.

Fluid velocity	
Inlet	$\mathbf{u}_f = \mathbf{u}_{test}$
Outlet	Zero gradient
Wall and interface	$\mathbf{u}_f - \mathbf{u}_s = 0$
Left and right	Periodic
Pressure	
Left and right	Periodic
Other boundaries	Zero gradient
Turbulence quantities	
Inlet	TI = 5%
Outlet	Zero gradient
Wall and interface	$(k, \varepsilon) = (0,0)$
Left and right	Periodic
Structure displacements	
Cantilever constraint	$\mathbf{u}_s = 0$
Interface	$\boldsymbol{\sigma}_s \cdot \mathbf{n} - \mathbf{h} = \mathbf{0}$
Mesh displacement	
wall and interface	$\hat{\mathbf{u}} - \mathbf{u}_s = 0$
other boundaries	$\hat{\mathbf{u}} = 0$

TABLE 4.8: Boundary conditions of the implicit systems.

4.2.5 Frame of reference

The frame of reference used to define the solution domain is an orthonormal right-handed set of unit vectors, defined as follows:

- *O* (origin): airfoil center of gravity

- *Z* (blade axis): vector parallel to the blade axis, directed from the hub to the tip.

- *Y* (rotation/thrust axis): vector lying on a plane normal to the rotor disc plane, parallel to the rotation axis of the fan and directed opposite to the fan angular velocity vector.

- *X* (in-plane axis): vector lying on the rotor disc plane, defined to close the orthonormal right-hand system.

Figures 4.12, 4.15 and 4.18 show the defined system, projected on the cascade plane.

4.2.6 Results

The following sections report the results of the three numerical tests with a brief description of the plots. A complete and general discussion on all the results is given at the end of the section.

We identify as CASE A the case with no elastic device and as CASE B the case with the device (FSI solution). Figures 4.12, 4.15 and 4.18 show the contour plots

Test 1	
Flow rate	99.88 m^3/s
Total efficiency	61.8 %
Maximum measured stress the blade	21.92 $\pm$ 2.94 MPa
Test 2	
Flow rate	79.29 m^3/s
Total efficiency	75.3 %
Maximum measured stress the blade	23.49 $\pm$ 2.67 MPa
Test 3	
Flow rate	51.03 m3/s
Total efficiency	52.9 %
Maximum measured stress the blade	24.47 $\pm$ 16.00 MPa

TABLE 4.9: Test conditions.

of the flow field quantities in the blade vane, for both the cases, with and without the elastic surface at the trailing edge. Here we choose to describe the fields with three non-dimensional quantities. In particular, we use the pressure field ($\tilde{p} = \frac{p - p_{inf}}{\rho_f}$) to have a view on the load acting on the blade surface. The velocity magnitude ($|\tilde{\mathbf{u}}| = \frac{|\mathbf{u}_f|}{|\mathbf{u}_{inf}|}$) and the streamlines to see the velocity field and the vorticity magnitude ($\xi = \tilde{\nabla} \times \tilde{\mathbf{u}}$) in order to see the turbulence and wake characteristics.

The other figures report the components of the aerodynamic force per unit length (as this is a 2D computation), acting on the blade section. In these plots, we use as directions to project the force, the in-plane direction (X) and out-of-plane direction (Y) (where "plane" is the rotor disc plane, e.g. see Figure 4.12).

It is important to notice that we do not change the original blade geometry and we test this device by adding an additional surface. As the aerodynamic load depends on the wet surface, in all the tests the aerodynamic force results greater in case B, which has a 1/4 of cord of length more. If we normalize the loads, evaluating the aerodynamic coefficient of the section, we can show that there is a reduction of the blade load associated to the use of the morphing system in the high load cases (Test 2 and 3). Starting from this consideration, we can obtain the plots of Figure 4.13, 4.14, 4.16, 4.17, 4.19, 4.20 evaluating the aerodynamic coefficients as follows:

$$C_x = \frac{F_x}{0.5\rho_f c |\mathbf{u}_{inf}|^2} \tag{4.1}$$

$$C_y = \frac{F_y}{0.5\rho_f c |\mathbf{u}_{inf}|^2} \tag{4.2}$$

Where C_x and C_y are respectively the in-plane and out-of-plane aerodynamic force coefficient.

All the simulations have started from a steady solution of the flow field (obtained with the bar as rigid in the case B) and have carried on setting a fixed $\Delta t = 0.001 sec$.

Test 1

In this test condition, the local angle of attack is about 6 degrees. The flow is attached and the elastic surface mean displacement does not affect significantly the flow field, except for a little oscillation of the pressure field due to vortex shedding associated to the elastic response of the bar. We can observe differences between the two cases looking at the aerodynamic force plots in Figure 4.13 and 4.14. Here two aspects are evident:

- the average load is higher in the case of trailing edge extension. As discussed before, the motivation is the increased wet surface of the section and we will ignore this aspect in future considerations.

- the effect of the elastic device is to increase the unsteadiness of the flow field, resulting in an oscillation of the aerodynamic load.

After the initial transient, the aeroelastic coupling reaches a stable oscillating condition for which it is possible to extract the vibrational characteristics. Starting from the displacement data of the elastic bar, we obtain a frequency of 13.6 Hz, an amplitude of 0.2 mm and a mean value of 2.5 mm and 0.89 mm in the Y and X direction respectively.
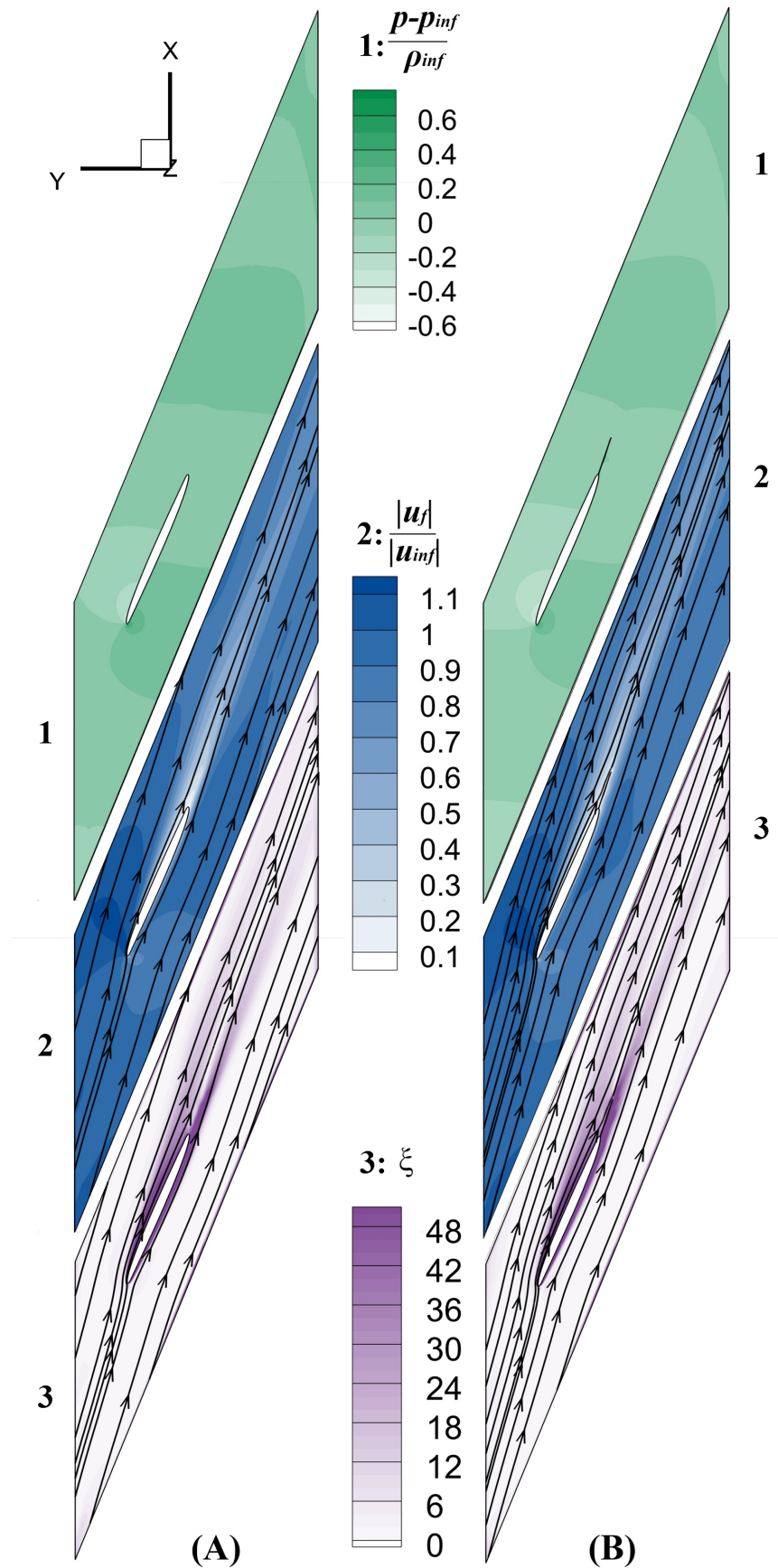
FIGURE 4.12: Test 1, flow field non-dimensional variables (1: pressure, 2: velocity magnitude, 3: vorticity). a) Original geometry; b) Elastic device at the trailing edge
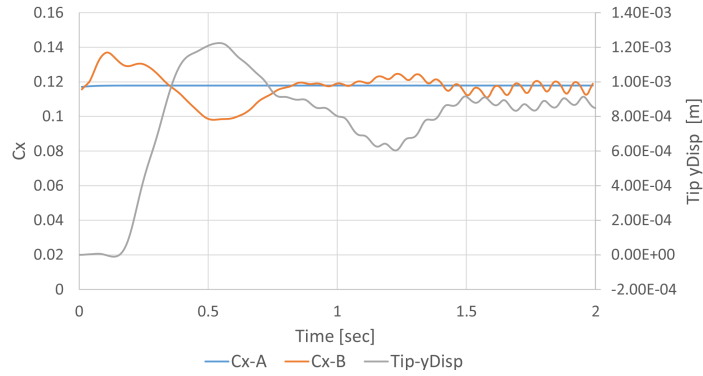
FIGURE 4.13: Test 1, aerodynamic force coefficient in the rotor plane direction (x) and vertical displacement of the elastic surface (tip point).
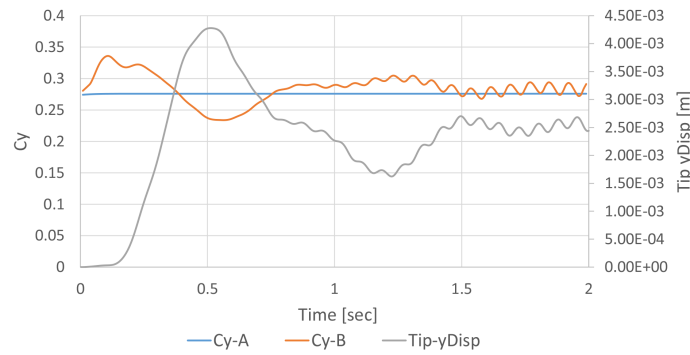

FIGURE 4.14: Test 1, aerodynamic force coefficient in the out-of-plane direction (y) and vertical displacement of the elastic surface (tip point).

Test 2

This test corresponds to the maximum efficiency condition. The local angle of attack is around 10 degrees and although a small separation region at the trailing edge is observable, the flow can be watched as attached. Here, the effect of the elastic extension on the flow field can be notice as a small reduction of the thickness of the wake released by the trailing edge (Figure 4.15, contours 2 and 3).

The instability related to the vortex shedding is present. However, this is not the only observable effect; indeed, the elastic surface responds directly to the main flow characteristics, assuming an average finite deflection upward.

The average aerodynamic coefficients are reduced from case B with respect to case A in both the directions. Therefore, we can state that the bar deflection "drives" better the flow reducing the aerodynamic drag, but at the same time, it reduces the pressure jump between suction side and pressure side, reducing the lift.

It is possible to define a stable oscillating condition with the following characteristics: 6.7 Hz of frequency, 0.5 mm of amplitude, and a mean value 3.85 mm in Y direction and 1.17 mm in X direction.
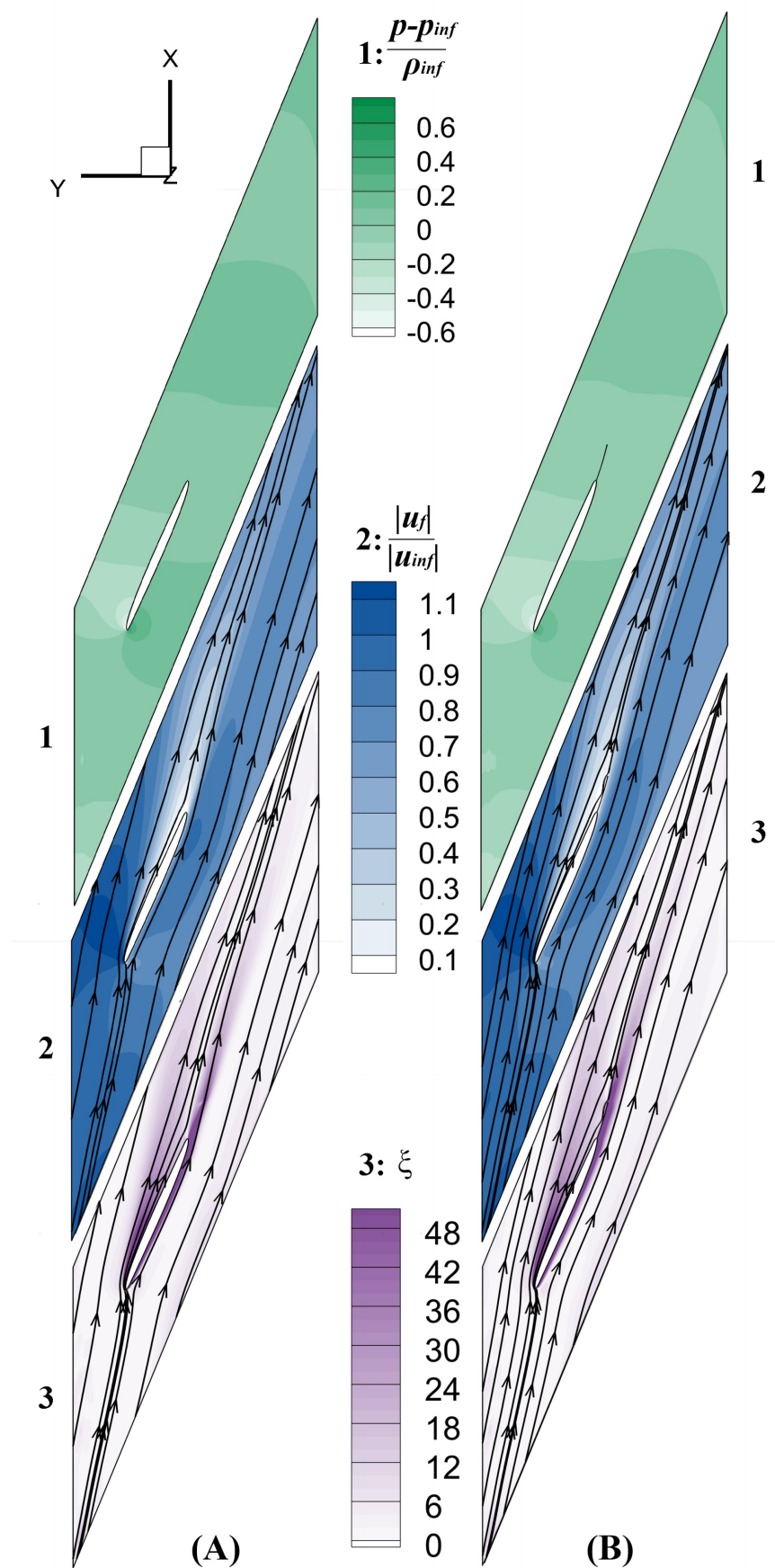
FIGURE 4.15: Test 2, flow field non-dimensional variables (1: pressure, 2: velocity magnitude, 3: vorticity). a) Original geometry; b) Elastic device at the trailing edge

FIGURE 4.16: Test 2, aerodynamic force coefficient in the rotor plane direction (x) and vertical displacement of the elastic surface (tip point).

FIGURE 4.17: Test 2, aerodynamic force coefficient in the out-of-plane direction (y) and vertical displacement of the elastic surface (tip point).

Test 3

In this case, the angle of attack of the section is about 13.5 degrees and a larger separation region is present. The fan is working in a condition with high aerodynamic load on the blade.

This time, the effect of the device on the flow field is more evident, especially from the velocity and vorticity fields in Figure 4.18. The presence of the elastically reacting surface at the tail of the airfoil seems to reduce the flow separation and the trailing edge stall.

This behaviour reflects on the aerodynamic forces, especially in the x direction, where a significant reduction is observable (see Figure 4.19 and 4.20). This effect represent what we were expecting from this kind of passive device, i.e. to reduce the load oscillations in stall conditions.

FIGURE 4.18: Test 3, flow field non-dimensional variables (1: pressure, 2: velocity magnitude, 3: vorticity). a) Original geometry; b) Elastic device at the trailing edge
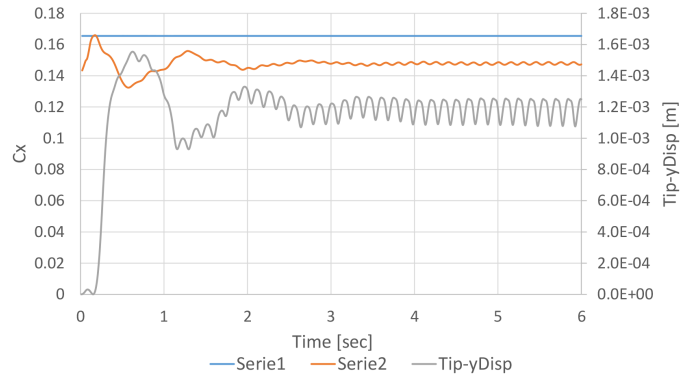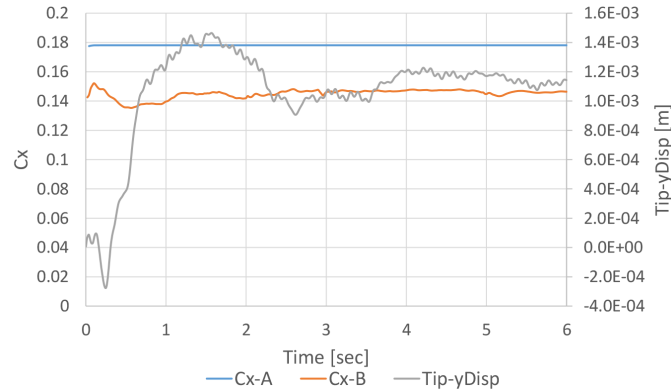
FIGURE 4.19: Test 3, aerodynamic force coefficient in the rotor plane direction (x) and vertical displacement of the elastic surface (tip point).
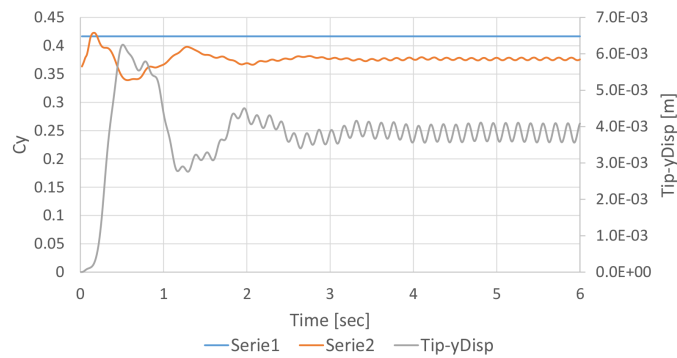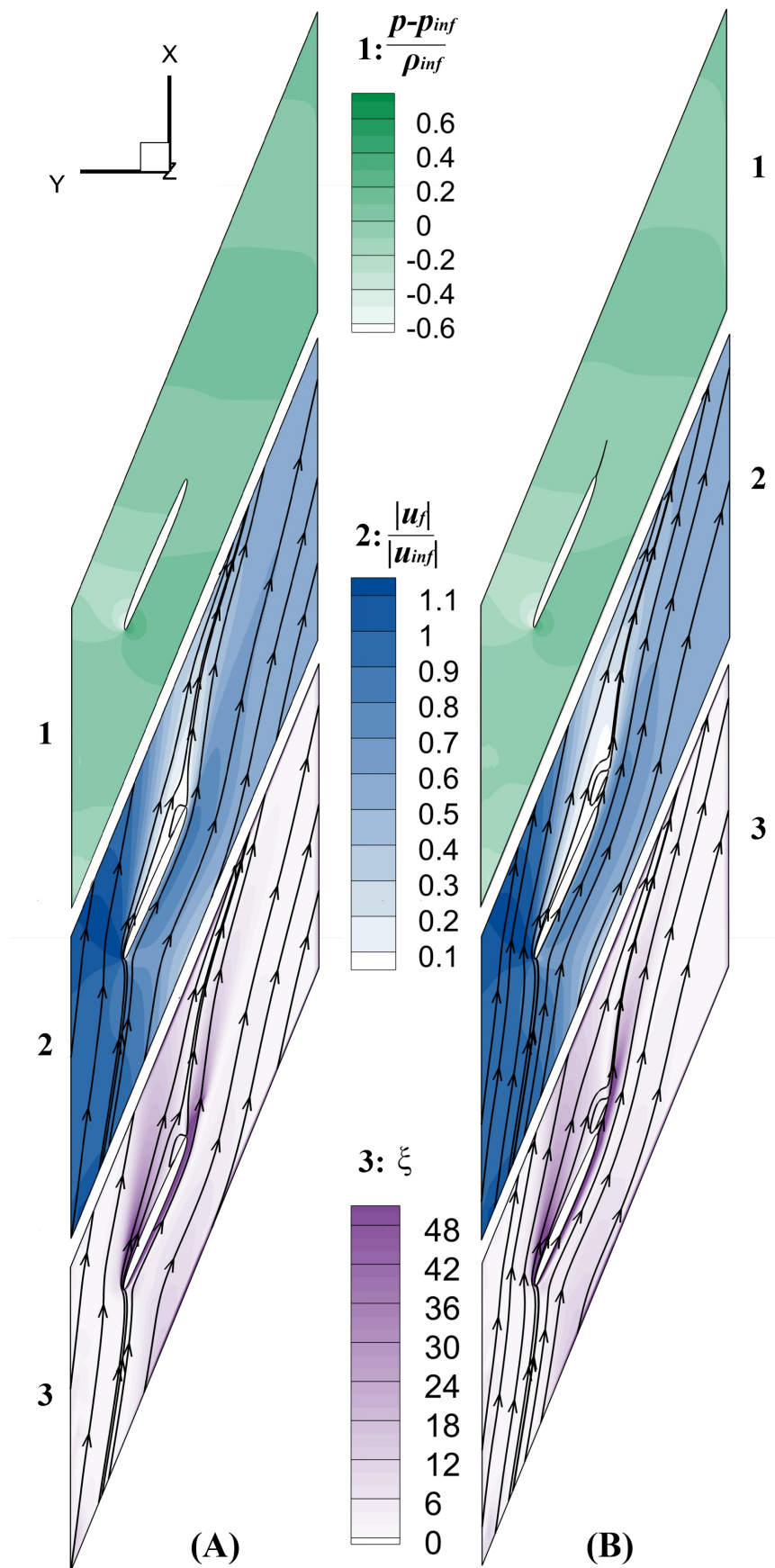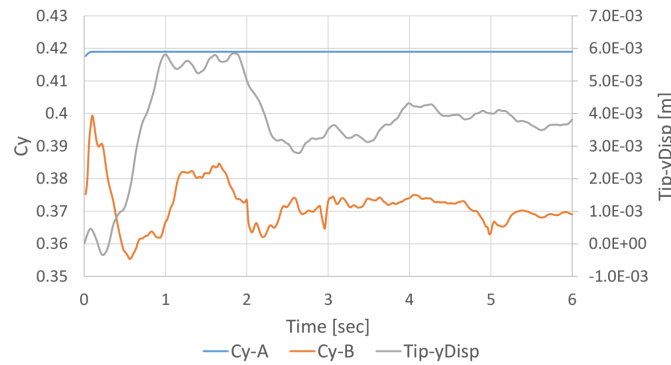

FIGURE 4.20: Test 3, aerodynamic force coefficient in the out-of-plane direction (y) and vertical displacement of the elastic surface (tip point).

This time the oscillation assume a complex shape, due to the unstable and complex dynamics associated to the largely separated flow.

General observations

The analysis of all the results leads to identify three main effects that the elastic passive device could have on this system. The first observation confirms the hypothesis that, leaving the trailing edge of the airfoil free to deflect as an effect of the aerodynamic load, allows to passively control the load magnitude and to reduce the stall in off-design, high incidence conditions. This aspect is dominant in Test 3 (Figure 4.18, 4.19 and 4.20).

The second consideration has to be done on the negative effect that the system has on the attached flow conditions. Here, it is possible to observe that, after a certain transient, the system starts to oscillate with a stable oscillation, which induces a vibrational load on the blade. This second phenomenon is dominant in Test 1, but is present also in Test 2, where both the effects give a noticeable contribution to the final observed dynamics.

The final observation has to be done on Test 2. Indeed, in this case, both the effects described above are present and they are acting in a considerable manner. It is important to notice that Test 2 is the case closest with the design condition at which the blade should work, and that both the effects reduce the performance. In fact, the first reduces the load and so the output of the fan, while the second introduces a vibratory load.

4.2.7 Conclusions

We tested the effect that a passive elastic device applied to the trailing edge of a large axial fan blade, has on the flow field and on the local sectional load of the blade.

The FSI solver has been applied to an extracted section of the blade at a high midspan radius; the section is treated as part of a periodic cascade, in three different inflow conditions, solving the field with and without the elastic device.

We can conclude from this study that the application of a morphing passive device to the reference blade results in two different effects, with respect to the flow condition. When the flow is totally attached, the fact of having an elastically reacting surface in the field leads to unsteadiness and oscillations for constant inlet velocities. On the other hand, the study shows that this solution has a potential applicability in controlling the load and the separation region in stall conditions.

However, both of these two effects have a negative impact on the performance near the design point, because of the lift reduction and vibratory load generation.

Nevertheless, this last consideration does not exclude the possibility of developing technologies in this direction and an interesting extension of this research could be a parametric study oriented

- to different lengths and materials, e.g. reducing the length and the material density, to have a more detailed map on the stall control capability, but also trying to reduce the aeroelastic vibration in stable flows;

- to a device integrated in the original section geometry, as a morphing trailing edge region.

4.3 Passive morphing control system for fan blades - 3D study

The work presented in [91] and in the previous section, represents the first part of a main study completed by this section. Here we extend the application to the three-dimensional blade, investigating the fluid-structure interaction dynamics also including all the effect neglected in the 2D problem and, in this way, completing the virtual testing of the device.

The work is subdivided in two phases. First, the aerodynamic field is solved in

order to find the span region in which to apply the control surface. Then, we can move to the fluid-structure interaction (FSI) simulations using the information on the test conditions and device material from the previous 2D study.

4.3.1   Fan description

We use for this study the fan blade of the FLÄKT WOODS 224JMTS (Figure 5.1), already used in the 2D study (Table 4.5).
For our computation we consider the blade installed on the hub with a pitch angle of 20 degrees. Figure 5.1 shows the fan and a sketch of the CAD model of the entire rotor.

4.3.2   Computational domain

The simulation has been done on a periodic domain relative to the single blade vane. Indeed, we suppose for now that the fan is operating in a clean inlet condition thus that the inlet flow is not affected by any distortion. This approach allows to save computational costs and simulation time, that is important considering the complexity of the coupled final system.
Figure 4.22, shows views of the domain which is a structured, multiblock domain of hexahedral elements. The frame of reference used to generate the domain is defined as follows

- **Origin**, point located at the intersection between the blade and fan axes;

- **Y axis**, axis of rotation, directed upwind with respect to the inflow absolute velocity;

- **Z axis**, corresponding with the blade CG axis, pointing in the radial direction;

- **X axis**, automatically defined to close the right hand frame

The overall computational mesh counts 1 million of elements subdivided in two main blocks, the structural block relative to the morphing surface and composed by 4.e+03 elements that form the solid three-dimensional structure, and the fluid block composed by the remaining elements. To guarantee a correct solution at wall we set the wall space such to have an average $y^+ \simeq 1$. Figure 4.22 shows also a section view of the mesh near the trailing edge.
The fluid domain is extended for one chord upwind from the leading edge and two chords downwind from the trailing edge.
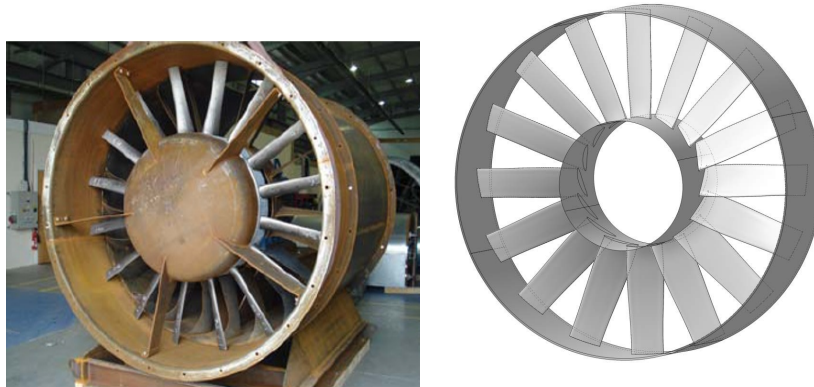
FIGURE 4.21: Fan view and cad model.

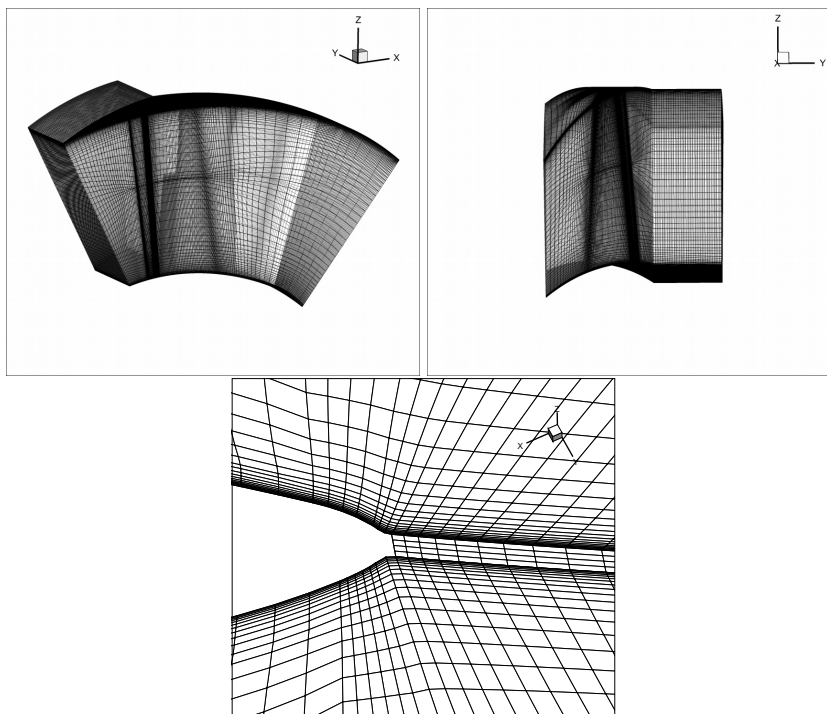FIGURE 4.22: Mesh: 3D view (top), lateral view (middle), section detail (bottom).

4.3.3 Boundary conditions and mechanical properties

We solve the system in the blade relative frame of reference, which is a system of axes that starts from the configuration outlined in the previous section, rotating with the blade. Figure 5.5 shows the boundary patches where are defined the boundary conditions reported in Table 4.11

Fluid phase

On the fluid domain we impose an inlet velocity which can be expressed in terms of relative velocity as

$$\mathbf{u}_{inf} = \omega \times \mathbf{x}_f|_{inlet} + V_{inlet}\hat{\mathbf{y}} \tag{4.3}$$

The function for the inlet absolute velocity V_{inlet} is obtained by scaling on the right flow rate the empirical function reported in the plot of Figure 4.23. In the same way is obtained the radial distribution of turbulent kinetic energy, scaling an empirical distribution in order to have an average turbulence intensity (TI) at inlet of about 5%.

In addition to the boundary condition we have to define the physical properties of the flow, which is air with standard density $\rho_f = 1.225$ and kinematic viscosity $v = 1.5e - 05$. The reference pressure is set to $p_{ref} = 0Pa$.

Deformable solid parts

The elastic surface is constrained to the trailing edge of the blade with a simple cantilever constraint.

The spanwise extension and placement of the surface will be decided after a preliminary CFD study, in order to apply it to the most useful zone.

The material and thickness properties of the moving surface are the same as in [91] and we recall them here in Table 4.10.
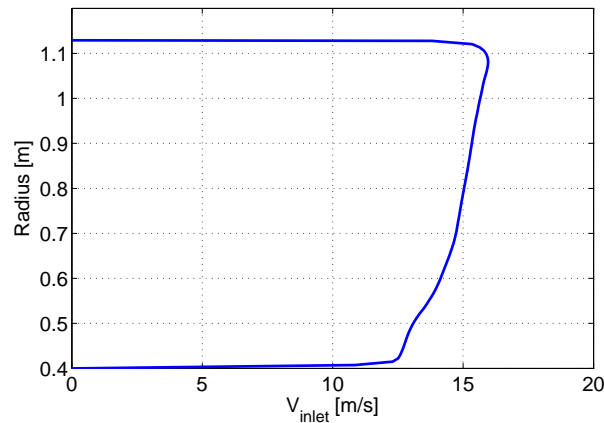
FIGURE 4.23: Radial distribution of the inlet absolute velocity for a flowrate of 51 m^3/s.
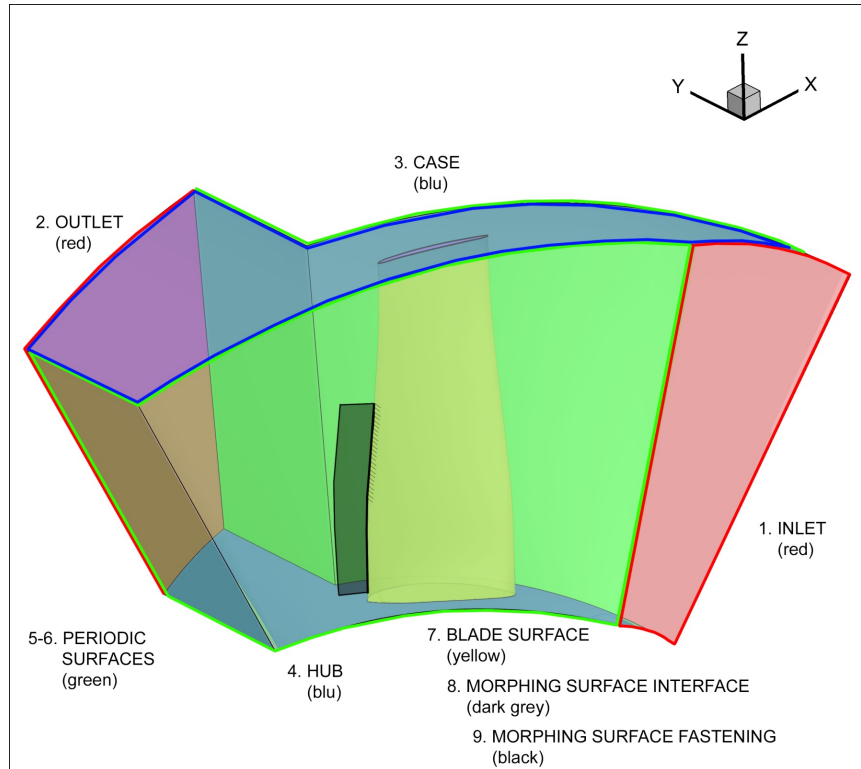
FIGURE 4.24: Boundary patches

Length	0.05 m
Thickness	0.001 m
Young modulus	300 MPa
Poisson coefficient	0.4
Density	1000 kg/m^3

TABLE 4.10: Flexible trailing edge extension characteristics.

Moving mesh

The moving mesh solver needs constraint at the equivalent solid boundary. In this case, the elastic domain will take the displacement directly from the structural solver, while for all the other boundary patches we simply fixed to zero the mesh displacements.

4.3.4 Operating point for FSI computation

Starting from the fan experimental data we are interested in high loaded conditions in order to see the maximum effect on the blade. We have the maximum load before the stall corresponding to $52 m^3/s$ of flow rate.

Patch	Fluid solver	Structural solver	Mesh motion
1. Inlet	$\mathbf{u}_f = \mathbf{u}_{inf}$	$\mathbf{u}_s = 0$	$\mathbf{u}_m = 0$
	$grad(p) = 0$		
	$k = k_{inflow}\ (TI = 5\%)$		
	$\varepsilon = \varepsilon_{inflow}$		
2. Outlet	*Zero gradient*	$\mathbf{u}_s = 0$	$\mathbf{u}_m = 0$
3. Case	$\mathbf{u}_f = \omega \times \mathbf{x}_{case}$	$\mathbf{u}_s = 0$	$\mathbf{u}_m = 0$
	$grad(p) = 0$		
	$k = 0$		
	$\varepsilon = 0$		
4. Hub	$\mathbf{u}_f = 0$	$\mathbf{u}_s = 0$	$\mathbf{u}_m = 0$
	$grad(p) = 0$		
	$k = 0$		
	$\varepsilon = 0$		
5-6 Periodic patches	*Periodicity*	$\mathbf{u}_s = 0$	$\mathbf{u}_m = 0$
7. Blade surface	$\mathbf{u}_f = 0$	$\mathbf{u}_s = 0$	$\mathbf{u}_m = 0$
	$grad(p) = 0$		
	$k = 0$		
	$\varepsilon = 0$		
8. Morphing surface	$\mathbf{u}_f = 0$		
	$grad(p) = 0$		
	$k = 0$		
	$\varepsilon = 0$		
9. Morphing surface fastening	$\mathbf{u}_f = 0$	$\mathbf{u}_s = 0$	$\mathbf{u}_m = 0$
	$grad(p) = 0$		
	$k = 0$		
	$\varepsilon = 0$		

TABLE 4.11: Boundary conditions.

4.3.5 Results

Dimensioning and placement of the morphing surface

Starting from CFD studies of the fan it is possible to see the aerodynamic field and select the portion of the blade in which the device could be more useful. We know from [91] that this kind of passive control should have the maximum benefit at high angle of attack configurations, reducing the stall of the blade sections.

What is important for the actual purpose is to catch the span region with a higher probability to find the flow separation. Figure 4.25 shows the velocity field computed from the initial state CFD. From this picture is evident that the root and low-mid span regions are the most affected by flow separation. We use this result

to place the device, which will be not on the entire blade span, leaving the tip and high-span region free. Indeed, we know from [91] that this morphing surface can introduce unsteady oscillation and vibrations at low angle of attack, which are common incidences at high span locations.

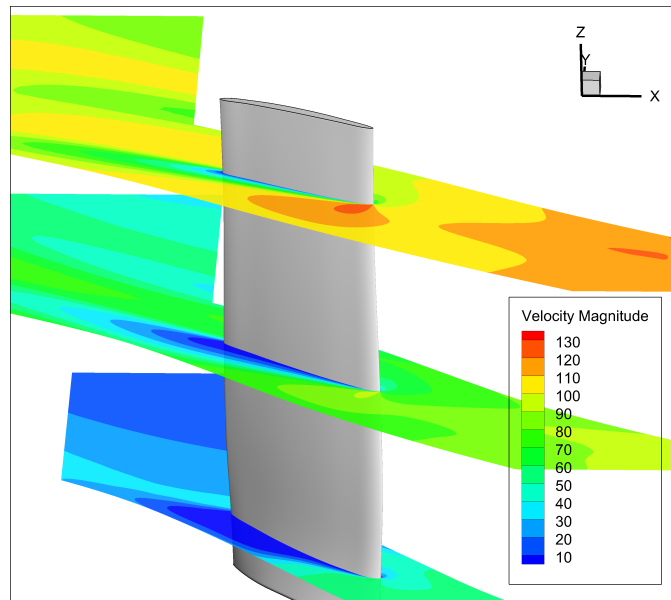Figure 4.26 shows the blade with the attached device.

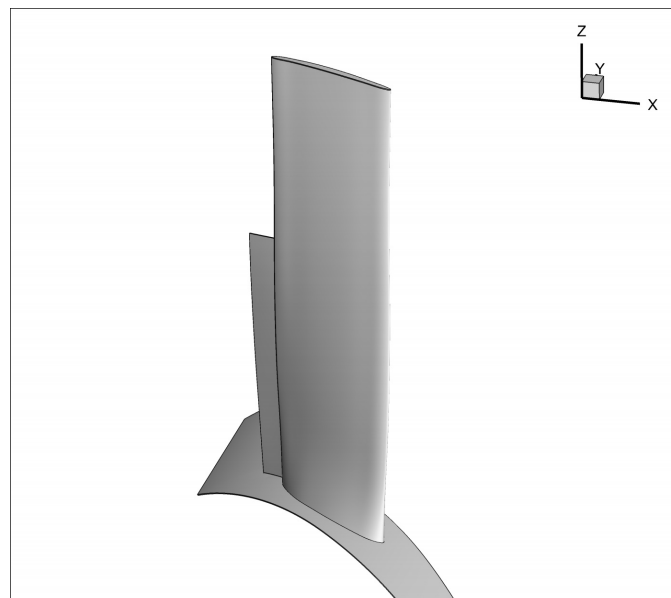FIGURE 4.25: CFD solution of the reference blade. Velocity field section at three different radius [*m/sec*].

FIGURE 4.26: 3D view of the blade with the elastic surface at the trailing edge

FSI solution: elastic displacement

The displacement of the surface results in a complex and three-dimensional mode. The twist of the blade and so the three-dimensionality of the geometry covers an important role on the complexity of the response. However, considering the low stiffness of the material coupled with the small thickness of the surface, we can notice that the motion is mostly affected by the aerodynamic forces, that, as we will see in the next sections, is related to the surface displacement because of the FSI coupling.

In order to show the displacement shape of the surface we plot on Figure 4.27 the contour and deformed shape corresponding to the time steps in the simulation (3 seconds of simulation using a 3E-03 sec of time step) corresponding to the maximum and minimum displacement recorded on all the nodes.

Figure 4.28 shows the time solution of the displacement of two reference nodes, in particular the node with higher displacement and the node at the tip of the higher section of the elastic surface.

Starting from the observation of these two plots, we can extract the frequency of the response (as the structure is elastic and the solver linear) which is about 1.18 Hz.
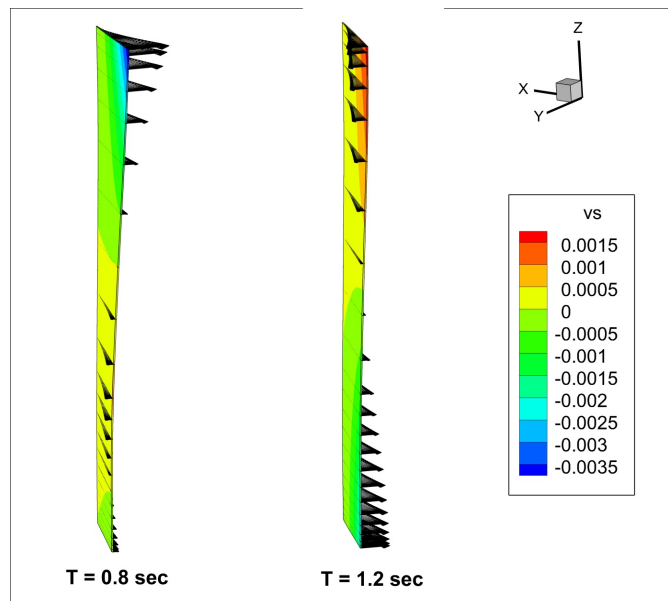
FIGURE 4.27: 3D displacement ([*m*]) solution of the elastic surface at time 0.8 sec (left) and 1.2 sec (right)
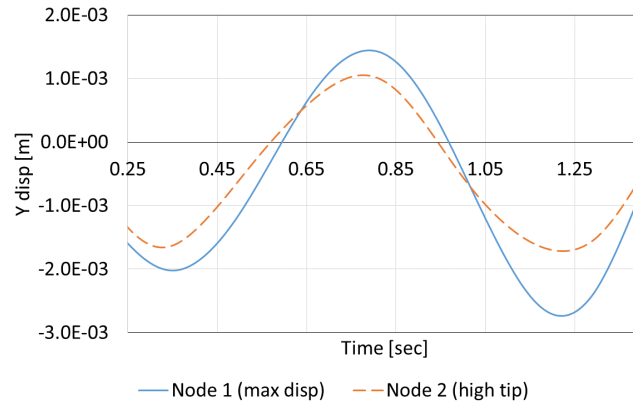
FIGURE 4.28: Main oscillation cycle in the time history of the y component of the displacement for nodes 1 (maximum displaced node) and 2 (higher section tip).
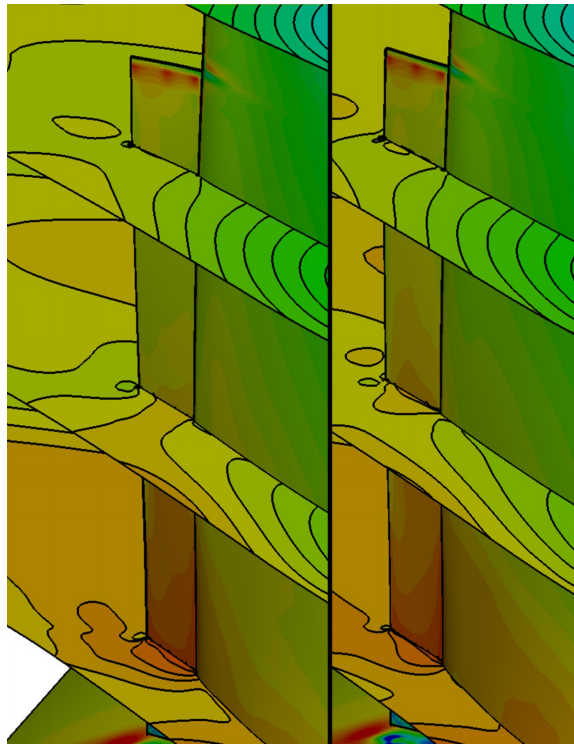
FIGURE 4.29: Detail of pressure contour plot at time 0.8 sec and 1.2 sec

FSI solution: unsteady aerodynamic field

The elastic displacement of the control surface affects the aerodynamic field in terms of vortex structures, pressure unsteadiness and velocity field. Figure 4.30 reports the view at different span-wise sections of the pressure field in the two observation points outlined in the previous section. In particular, we choose the same time steps of Figure 4.27 which are the most significant for an evaluation of the

unsteadiness of the fields due to the surface displacement (and thus due to the coupling between the two physical systems). It is possible to observe how, due to the elastic motion, the pressure field results as an unsteady field. The detail showed in Figure 4.29 underlines the generation of pressure fluctuation due to vortex structures generated by the trailing edge motion.
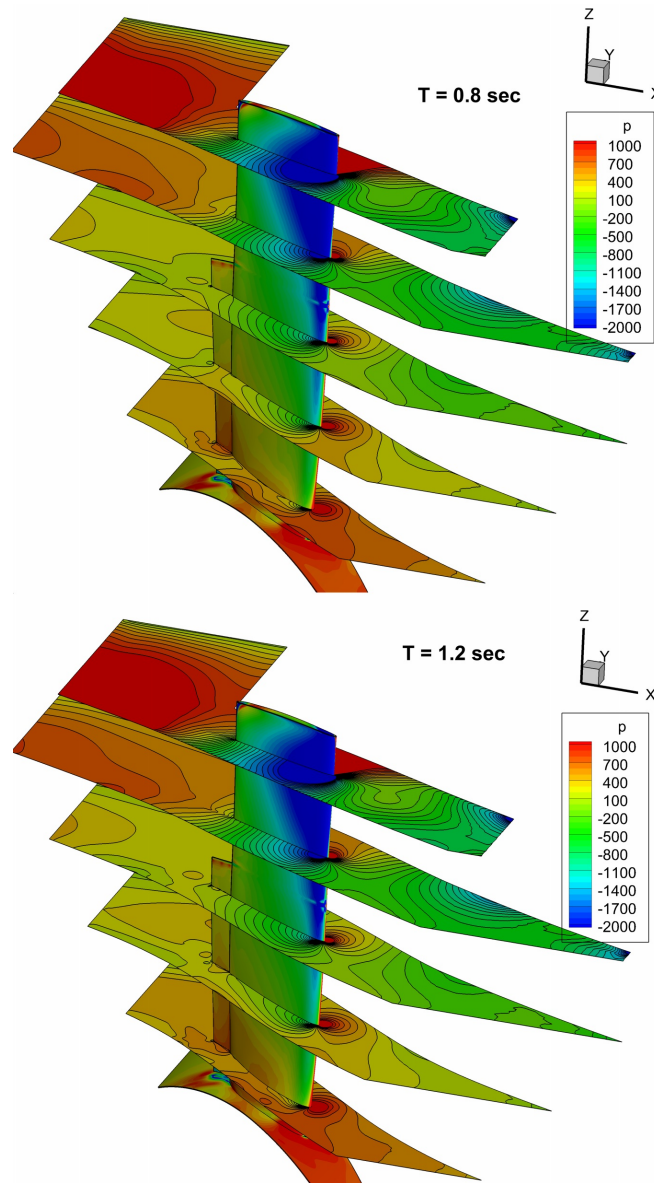
FIGURE 4.30: Sectional contour of pressure [*Pa*] field at time 0.8 sec and 1.2 sec

Observations on performance and effect of the control device

Recalling the results obtained in [91] we can confirm the stabilization effect on the separating flow at the root sections of the blade. Figure 4.31 demonstrate this statement showing the reduction of the separation area. However, the aerodynamic field in the middle-span section become unstable because the presence of the elastic

device, which starts an unsteady and unstable vibration when coupled with the aerodynamic. The low stiffness used to define the material plays an important role in allowing this unstable coupling and further study on the choice of a suitable material could solve this problem.
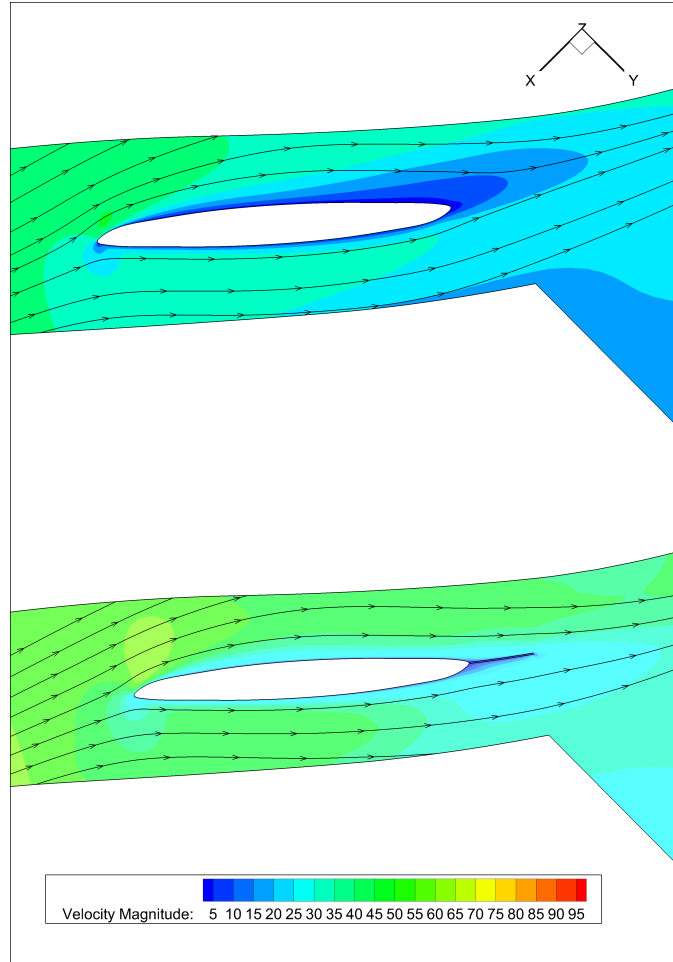
FIGURE 4.31: Velocity field [m/s] at R = 0.5 m

The three-dimensional nature of the surface oscillation and the shape of the unsteady aerodynamic field conducts to a final consideration about the possibility of studying FSI problems on fast rotor blades using the two-dimensional approximation at the section. Indeed, it is evident that the three-dimensional effects are not negligible in this kind of solution unless to accept a certain grade of approximation.

4.3.6 Conclusion

We studied the effect of a passive morphing control surface applied to the trailing edge of the blade of a large horizontal axis fan, simulating in time the unsteady system with a fluid-structure interaction solver.
Recalling the previous study on the same topic but at the section level (two-dimensional study), we complete the numerical testing of the control device verifying its effect

also in three-dimensional case. To do it, we chose from the sectional study the most significant operating point showing that for this kind of geometry, the three-dimensionality of both the flow and structure response introduce a not negligible complexity on a FSI problem.

The device, which was supposed to mitigate the flow separation in high loaded condition, works properly for the near root radial positions, but the unstable aeroelastic motion produces pressure fluctuation at the mid-span region.

Further studies could be done on different materials and configurations, keeping in mind the importance of using strongly coupled solver in order to catch the non-negligible mutual interaction between the structure dynamics and the surrounding aerodynamic field.

Chapter 5

Advanced FSI in industrial fan blade simulation

Industrial and aeronautical fan technology followed in recent years a continuous development assisted by numerical CAE (Computation aided engineering) tools. Furthermore, the application of new materials and manufacturing techniques permits to generate complex three-dimensional designs with high aerodynamic performance. Ample literature can be found on design and testing of horizontal axis fan blade with CFD (e.g. [92]) and FEA tools (e.g. [93]), with very high fidelity models adopted to study aerodynamics and structure stresses.

Although the high level of accuracy showed by CFD and structural FEA models, they start to lack in consistency with the physical problem when the coupling effects between aerodynamic field and structure response become not negligible for the purpose of the analysis.

Aeroelastic problems in turbomachinery attract the attention of industrial and academic researchers [94, 95, 96, 97]. At the moment, the most part of the literature produced for this topic presents studies on flutter and mistuning or flow unbalancing effect on the aeroelastic response, using the one-way weak coupling approach, see for example [95]. The assumption of small or negligible fluid-structure coupling is often adequate in the case of turbomachinery flutter. However, Sadeghi and Liu demonstrate in [98] that this assumption breaks down for light and slender blades (small inertia structures). Furthermore, the nonlinear flutter behaviour is not predictable with linearized models and one-way coupling models. Nonlinear flutter cases in turbomachinery were demonstrated by Carstens and Belz in [99] and by Sadeghi and Liu in [100, 98].

Although many research studies were conducted by Tezduyar and Takizawa (on parachute applications [101]), Bazilevs (on wind turbines [102]), strongly coupled FSI simulations on fan blades with three-dimensional non-linear models are much less common to find in the literature. The work of Sadeghi and Liu [103] on the coupled fluid-structure simulation for turbomachinery blade rows, shows an application of the method to a transonic fan. In this work, the authors solve the eigenvalue problem for the linear structure dynamics, which guarantees a fast and filtered solution, neglecting the high-frequency modes. The aerodynamic is solved through a 3D-RANSE model with good agreement with the experimental data.

Following a very similar logic, we present in this chapter a work in which the strongly coupled solver is used to study the FSI on a large subsonic fan, showing the effect on both the fluid part and the structural part, focusing on the aspect directly related to the coupled dynamics.

5.1 Problem set-up

5.1.1 Fan description

As in the previous chapter we use the fan blade of the FLÄKT WOODS 224JMTS (Figure 5.1, Table 4.5). The choice of the fan is simply related to the availability of experimental data of the overall aerodynamic performance.
Also in this case we consider the blade installed on the hub with a pitch angle of 20 degrees.

5.1.2 Computational domain

The simulation has been done on a periodic domain relative to the single blade vane, similar to what presented in the previous chapter. Indeed, we suppose also in this case that the fan is operating in a design condition and the inlet flow is not affected by any distortion. This approach allows to save computational costs and simulation time, aspects which are important to keep into account considering the complexity of the coupled final system.

 Figure 5.2 shows a view of the domain, which is structured, multiblock and composed by hexahedral elements. The frame of reference is defined as follows:

- **Origin**, point located at the intersection between the blade and fan axes;

- **Y axis**, axis of rotation, directed upwind with respect to the inflow absolute velocity;

- **Z axis**, corresponding with the blade CG axis, pointing in the radial direction;

- **X axis**, automatically defined to close the right hand frame

FIGURE 5.1: Fan view and cad model.
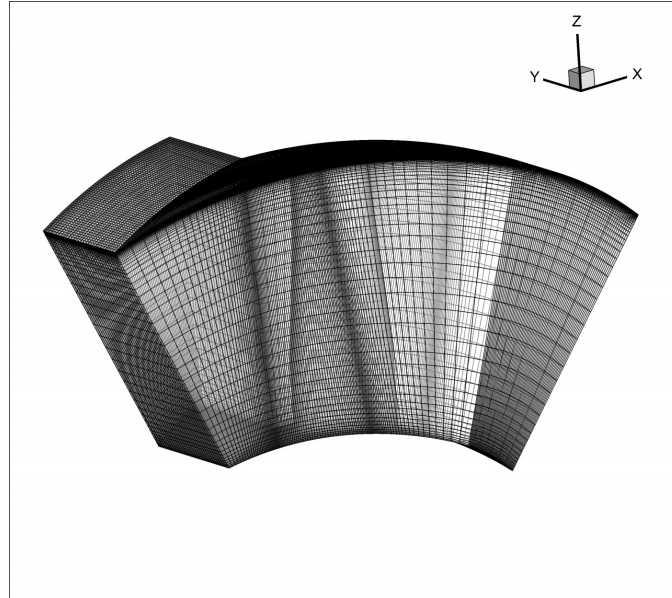
FIGURE 5.2: Mesh: 3D view.
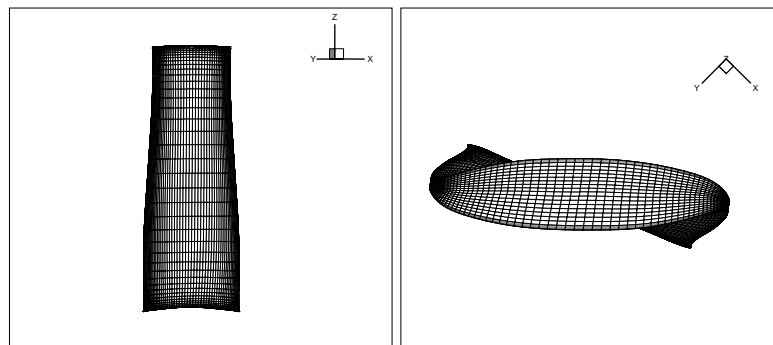
FIGURE 5.3: Structural mesh

The computational mesh is subdivided in two main blocks, the structural block (Figure 5.3) composed by 4.e+04 elements that form the solid blade structure, and the fluid block composed by 5.e+05 elements. To guarantee a correct solution at wall we set the wall space such to have an average $y^+ \simeq 1$, while for a complete development of the flow field we extended the domain 1 chord upwind from the leading edge and 2 chords downwind from the trailing edge. Figure 5.4 shows a section view of the mesh near the trailing edge.

5.1.3 Boundary conditions

We solve the system in the blade relative frame of reference. Figure 5.5 shows the boundary patches where are defined the boundary conditions reported in Table 5.1
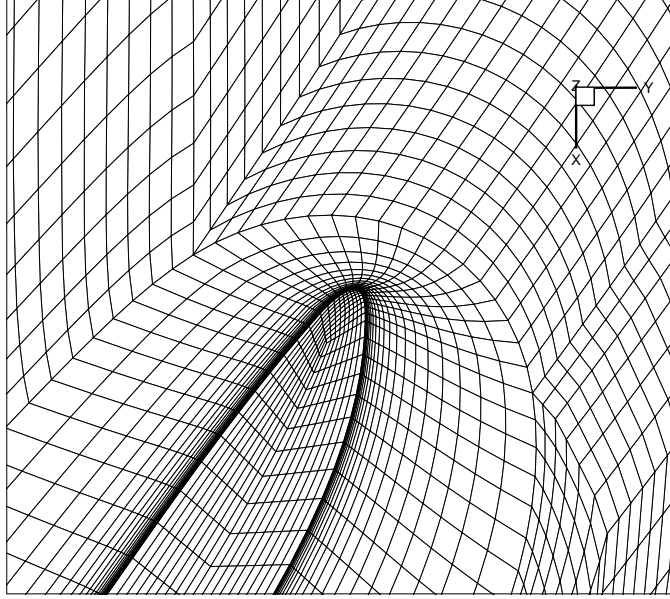
FIGURE 5.4: Mesh section detail

Fluid phase

The BC structure for the fluid case is very similar to what already defined in Chapter 4 for the 3D case. On the fluid domain, we impose the inlet velocity in terms of relative velocity as

$$\mathbf{u}_{inf} = \boldsymbol{\omega} \times \mathbf{x}_f|_{inlet} + V_{inlet}\hat{\mathbf{y}} \tag{5.1}$$

The function for the inlet absolute velocity V_{inlet} is obtained by scaling on the right flow rate the empirical function reported in the plot of Figure 4.23. In the same way is obtained the radial distribution of turbulent kinetic energy, scaling an empirical distribution in order to have an average turbulence intensity (TI) at inlet of about 5%.

Again, the physical properties of the flow are referred to air with standard density $\rho_f = 1.225$ and kinematic viscosity $\nu = 1.5e - 05$. The reference pressure is set to $p_{ref} = 0Pa$.

Deformable solid parts

The blade is considered constrained to the hub with a simple cantilever constraint. The material is aluminium alloy with the main properties reported in Table 5.2.

Moving mesh

The moving mesh solver needs constraint at the equivalent solid boundary. In this case, the elastic domain will take the displacement directly from the structural solver, while for all the other boundaries we simply fixed to zero the mesh displacements.
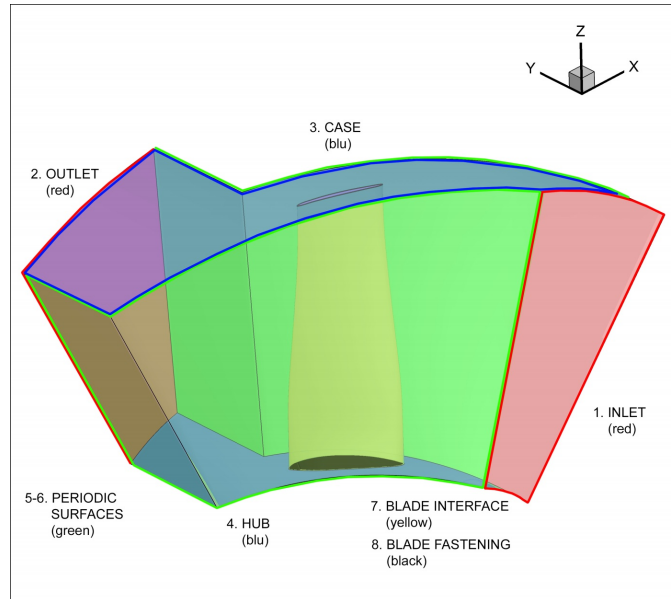
FIGURE 5.5: Boundary patches

5.1.4 Operating point for FSI computation

Looking at the efficiency curve in Figure 5.6 we can see that the maximum efficiency point is for a flow rate of about 79.3 m^3/s. We chose this point for the FSI calculation as we are interested in to verify how the aeroelastic coupling affects the performance and the aerodynamic field, thus, in a virtual prototyping point of view, we should focus on the significant operating point used in the fan design.
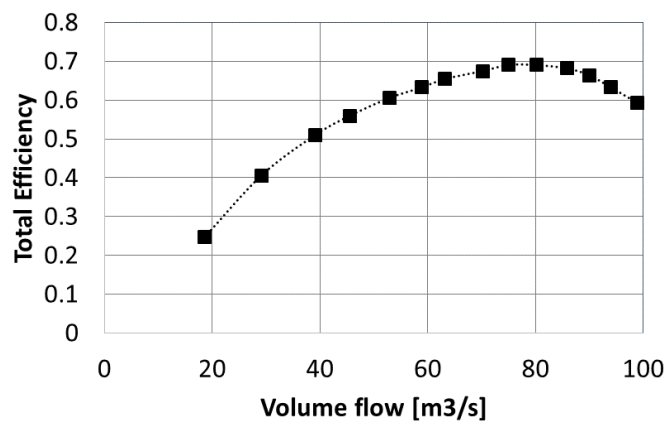
FIGURE 5.6: Fan efficiency from experimental data

Patch	Fluid solver	Structural solver	Mesh motion
1. Inlet	$\mathbf{u}_f = \mathbf{u}_{inf}$	$\mathbf{u}_s = 0$	$\mathbf{u}_m = 0$
	$grad(p) = 0$		
	$k = k_{inflow} \ (TI = 5\%)$		
	$\varepsilon = \varepsilon_{inflow}$		
2. Outlet	*Zero gradient*	$\mathbf{u}_s = 0$	$\mathbf{u}_m = 0$
3. Case	$\mathbf{u}_f = \omega \times \mathbf{x}_{case}$	$\mathbf{u}_s = 0$	$\mathbf{u}_m = 0$
	$grad(p) = 0$		
	$k = 0$		
	$\varepsilon = 0$		
4. Hub	$\mathbf{u}_f = 0$	$\mathbf{u}_s = 0$	$\mathbf{u}_m = 0$
	$grad(p) = 0$		
	$k = 0$		
	$\varepsilon = 0$		
5-6 Periodic patches	*Periodicity*	$\mathbf{u}_s = 0$	$\mathbf{u}_m = 0$
7. Blade interface	$\mathbf{u}_f = 0$		
	$grad(p) = 0$		
	$k = 0$		
	$\varepsilon = 0$		
8. Blade fastening	$\mathbf{u}_f = 0$	$\mathbf{u}_s = 0$	$\mathbf{u}_m = 0$
	$grad(p) = 0$		
	$k = 0$		
	$\varepsilon = 0$		

TABLE 5.1: Boundary conditions.

Material	Aluminium alloy
Young modulus	64 GPa
Poisson coefficient	0.34
Density	2700 kg/m^3

TABLE 5.2: Blade material properties.

5.2   Results

5.2.1   Performance verification with CFD

We need to solve the CFD with fixed geometry in order to give to the FSI solution a correct initial condition.

To verify the CFD solution we can compare the total pressure jump obtained with the steady solution of the RANSE problem with the experimental data. Figure 5.7 shows the fan curve of the total pressure jump with respect to the flow rate.

From the range of solution obtained we continue our analysis from the one corresponding to the maximum efficiency flow rate. Figure 5.8 shows a sectional view at different blade span location of the velocity field for the selected point. In this case the structure is considered fixed so the solution process has been carried
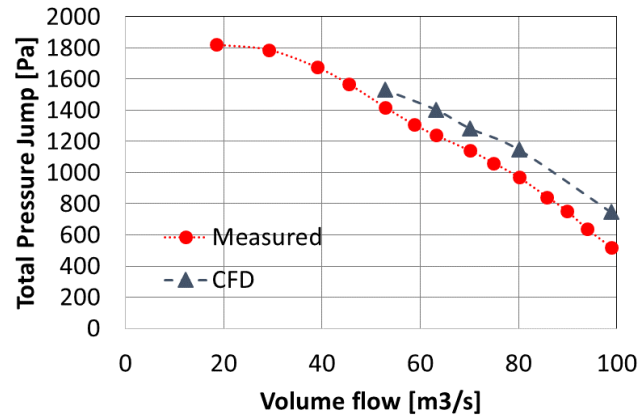
FIGURE 5.7: Total pressure jump.

on until the steady state.

5.2.2 FSI solution: elastic displacement

Figure 5.9 shows the total displacement of the blades points. From a static point of view, the displacement of the structure results in a coupled bending-torsion mode as in most turbomachinery applications that present blades with high aspect ratio. The bending is directed upwind, out of the disk plane, as effect of the lift force. The blade is mechanically balanced on is axis and with respect to the centre of rotation so the torsion is due to an unbalanced aerodynamic pressure at the section, e.g. a finite distance between the aerodynamic centre and the section elastic centre coupled with the aerodynamic moment of the section.

In order to give a measure of the structure dynamics we chose to show the displacement of the tip nodes at the leading and trailing edges. Figure 5.10 shows the time history of the displacement of these two node. Neglecting to comment the displacement in axial direction (Z), which is only related to the centrifugal forces, we can focus on the other two components related to the aeroelastic motion. It is very interesting to notice that the phase of the nodal displacement is shifted. This is a very common effect in aeroelasticity due to the strong coupling of the aerodynamic forcer and the structure motion, although the magnitude of the displacement is very small due to the high blade stiffness. Indeed, the chosen blade is an old design blade made with a high stiffness material that, coupled with an high stiffening effect of the centrifugal force, does not allow large displacements.

5.2.3 FSI solution: unsteady aerodynamic field

We choose as observation point the instant of maximum displacement at tip, however, to choose a different step would bring to similar results. Indeed, the difference is related to the fact that the FSI solution field is unsteady and the unsteadiness in the field can be only generated by the elastic motion.

Figure 5.11 shows respectively the difference between velocity and pressure fields, made between the steady CFD and the FSI cases. It is possible to notice how the elasticity of the blade affects the field around it, producing pressure oscillations in time and space and conditioning the velocity field as effect of the moving boundary.

5.2.4   Observations on performance

As explained, the high stiffness of the structure and its motion does not allow large deformations. The maximum amplitude of the aeroelastic oscillation is in the order of 1 mm. This low value indeed cannot affect in a considerable way the performance of the fan as Table 5.3 reports. Thus, we can orient for this study the analysis of the results just at the observation of the dynamic of the fields.

Solver	Total pressure jump [kPa]
CFD	1147.34
FSI	1150.28

TABLE 5.3: Performance comparison, total pressure jump.

5.3   Conclusion

The numerical fluid-structure interaction analysis was applied to study an axial fan blade. Using a dedicated finite element solver we were able to obtain in one simulation the solution of the unsteady turbulent flow and structural motion in the blade vane.

The blade motion results in a small and phase shifted vibration composed by a coupled bending-torsional mode. As expected, the bending motion is directed upwind (toward the suction side) and out-of-plane, while the torsional vibration is principally due to aerodynamic unbalancing at the blade section (effect of flow separation at the trailing edge and blade twist.

The analysis of the flow field influenced by the structure motion shows the development of pressure fluctuation at the blade surface, these fluctuations do not affect the performance because of the high stiffness of the structural system. However, this kind of effect can affect the aeroelastic stability, as they will be amplified in cases of lighter and softer materials or more slender designs. The development of CAE tools able to solve these coupled systems will give a very useful testing platform for future fan virtual prototyping.
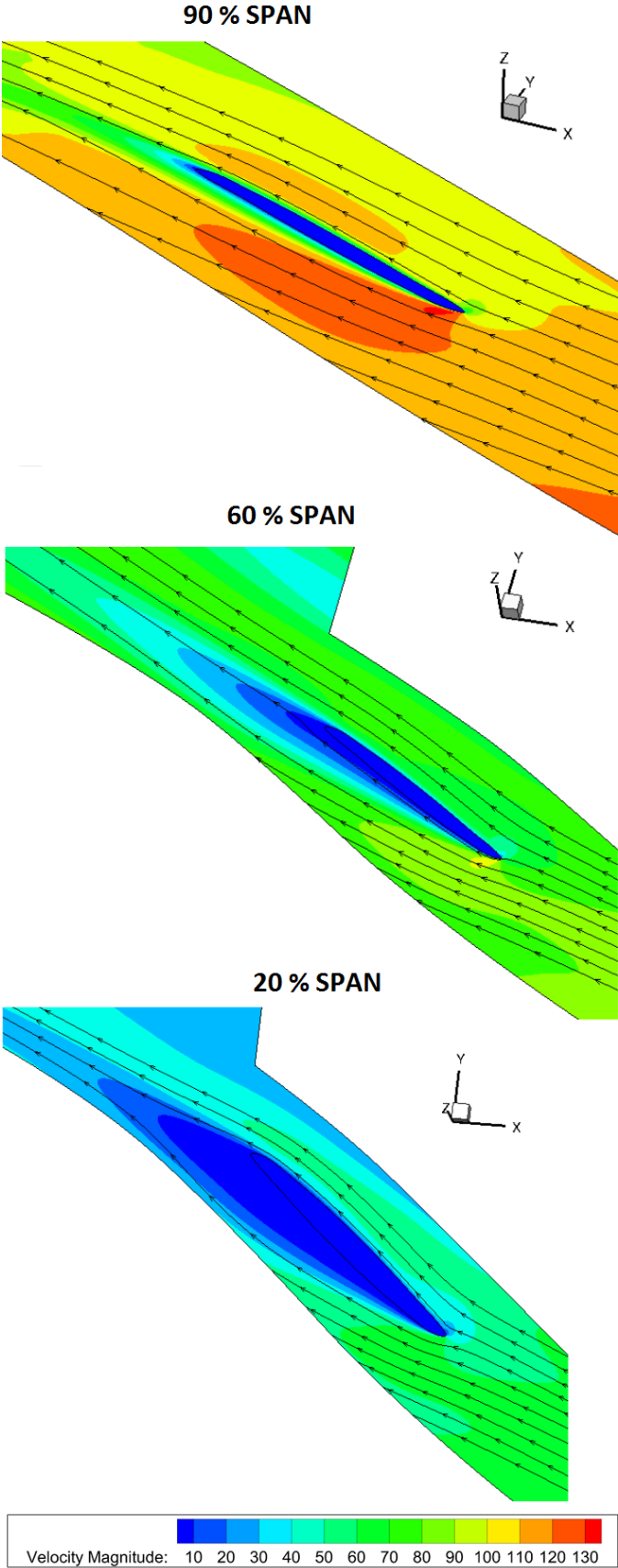
FIGURE 5.8: Velocity magnitude [m/sec] at 20 %, 60 % and 90 % of blade span
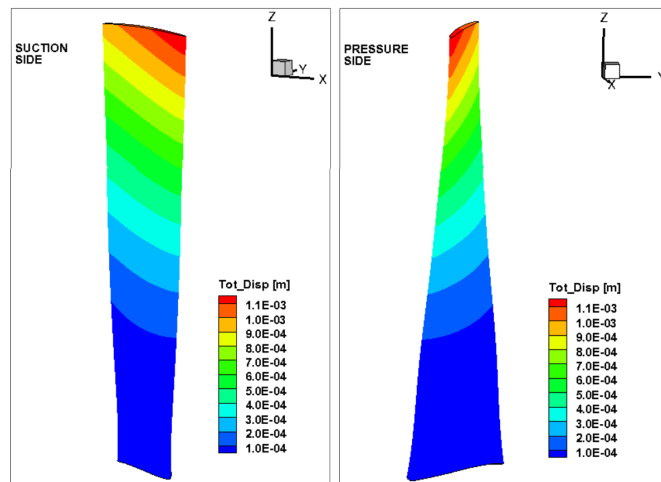
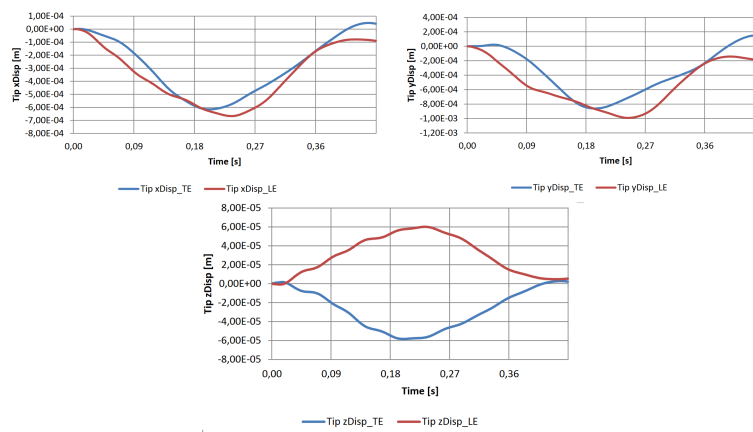FIGURE 5.9: Blade displacement magnitude.

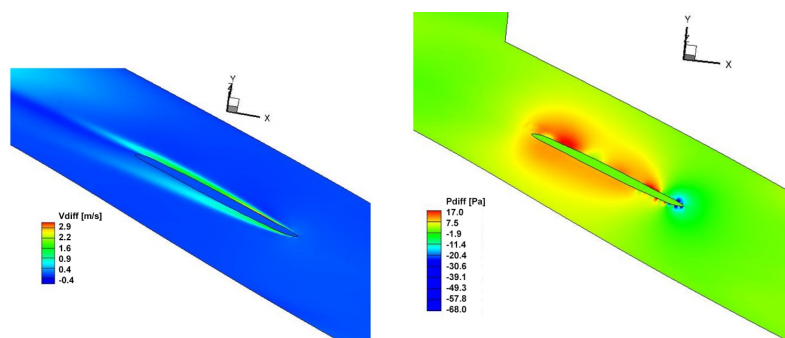FIGURE 5.10: Tip nodes displacements. top: X component; middle: Y component; bottom: Z component

FIGURE 5.11: Difference of velocity (up) and pressure (down) fields between steady CFD and FSI simulation

Chapter 6

Numerical simulation with adaptive boundary method for predicting time evolution of erosion processes

This section presents the application of the interface MaSAI algorithm, presented in Chapter 3. The algorithm connects the two codes for flow field and particle motion and deposition simulations to study with a new approach the time evolution of erosion on a target body.

This approach shows a big potential for those applications where a long time simulation is important but not possible with the classical numerical techniques. Solid particles such as dust, sands, ash particles from combustors, volcanic ashes, despite the filtering systems are often dragged by the flows evolving in turbomachinery. These particles might impact a surface of the turbomachinery (typically blade or vane surfaces) and stick to or erode it. Particle deposition and erosion (which is the focus of this work) alter the target surface geometry, which in turn affect the aerodynamic of the machine. Numerical prediction of such phenomena are usually solved adopting a one-way coupling approach since particle concentration is very small (less than 1.0E-06) [104]. This means that the flow is not affected by the particles and their effects on surface geometry, and the particles are dragged by the same flow field during the simulation. So far, a number of studies have been performed according to this approach. Tabakoff in 1970s [105] was a pioneer of numerical pre-diction of erosion process in turbomachinery applications, keeping working in this field for more than 40 years, and mostly focusing his study in turbine erosion (i.e., [106, 107]). His experiments and numerical simulations opened the way to several other scientists and researchers. For instance, just to cite some studies published in the last decades, Ghenaiet simulated the erosion process on a small radial compressor [108] and a ventilating system [109]. Suzuki and Yamamoto [110] performed a numerical prediction of sand erosion in a single-stage, axial compressor. Mazur et al. [111] numerically studied particle erosion pro-cess

in the main stop valve of a steam turbine; Mack et al. [112] uses numerical simulations to predict the erosion on guide vanes and in labyrinth seals in hydraulic turbines. In some previous works, our group adopted Tabakoff models to simulate the erosion process in several turbomachinery applications, from industrial fans to wind turbine blades (i.e., [113, 114, 115, 116, 117, 118, 119]).

In the cited studies, numerical predictions do not account for the flow field changes due to erosion caused geometry variations of the target bodies, however this aspect may be relevant, especially turbomachinery, to predict the body life, its structural integrity, the time evolution of the erosion process or the performance degradation of a given machine. In these cases, the use of a coupled solver allows to account for the effect of boy shape changes, and also increases the accuracy of prediction.

In this work, we simulate the time evolution of particle erosion using moving-mesh fluid-structure solver, coupled with a particle tracking and erosion code. The use of a run-time mesh motion technique allows to account for the time evolution of erosion effects on body shape, and in turn on flow field, avoiding to rebuild the mesh at each geometry change.

Particle erosion rate is predicted adopting the Tabackoff model reported in [8], accounting for particle impact velocity and angle, and material properties of both the particles and target surface. According to the computed erosion rate, mesh of the solid body is moved and the flow field computation repeated with the new geometry.

In order to show the potential of this approach we study the erosion process of a metal cylinder immersed in a high-Reynolds, uncompressible flow. Results will show the time evolution of erosion process and its effect on flow field.

6.1 Case in study and computational details

We define as sample case to test the algorithm, a metal cylinder in a channel flow with sand particles. The geometry of the domain is depicted in Figure 6.1. Although the geometry is three-dimensional, we force periodicity on the z direction in order to reduce the flow complexity and avoid complicated three-dimensional effects other than the ones introduced by a non-symmetric erosion. The computational domain is a structured mesh of 5.0E+04 hexahedral elements and is used for both the aerodynamic and particle clouds dynamics calculations. Figure 6.2 shows a sketch of the grid.

As we are defining a virtual application, the particular initial and boundary conditions values are not crucial until they belong to the range of applicability of the mathematical models adopted. In this sense, we choose to simulate a flow with Reynolds number of about 6.0E+05 and Mach number 0.1. The turbulence model is a so-called low-Reynolds model, so the only constraint on the computational domain is to set $y^+ = 1$ at the wall boundary. The outlet and inlet surface are far enough to avoid a bad conditioned flow at the cylinder.

The same discussion can be done for the particle cloud phase. The clouds properties are chosen to obtain a significant and physically consistent effect on the erosion shape. Therefore, we set the integration time-step and initial clouds positions and dimensions, consistently with the geometry and aerodynamic field.

Table 6.1 reports the boundary and initial conditions for both the aerodynamic and moving mesh solvers, while Table 6.2 reports the main properties of fluid and particles.

In particular, as for the solid phase we assumed that it consists of coal ash particles, and stainless steel is assumed as target material. These materials can be found in real applications, such as in the case of an induced draft fan used for exhaust extraction in coal-fired power plants. Silicon reach ash particles dragged by the exhaust are very erosive and the fan undergoes severe erosion [120].

The total amount of simulated particles is here divided into six clouds (each containing 50 M particles) uniformly distributed along an inlet line covering a cylinder diameter size (Figure 6.3). Clouds inlet velocity equals the gas velocity, and clouds enter the domain at each step of the simulation. It is worth noting that the inlet position of the clouds is not perfectly symmetric with respect to the cylinder; this is done on purpose in order not to have e perfectly symmetric erosion pattern. Within each cloud, particles have identical size and properties and are distributed following a Gaussian curve, according to Baxter [47]. Moreover, particles are assumed to be spherical, non-rotating and non-reacting.

For the operation of MaSAI algorithm we set as minimum erosion displacement $e_{lim} = 2.5mm$.
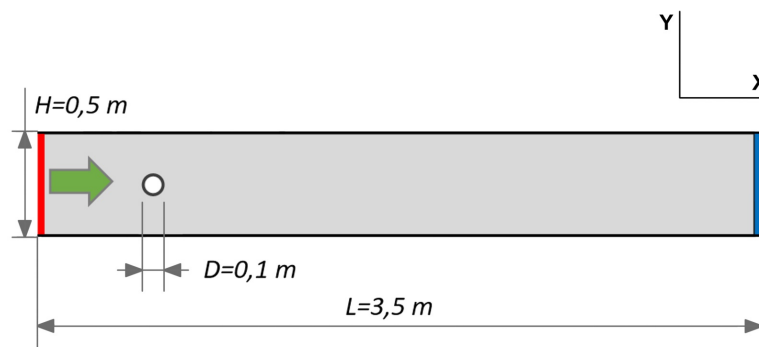
FIGURE 6.1: Geometry of the numerical domain: inlet (red line), outlet (blue line), periodic (gray surface), flow direction (green arrow).
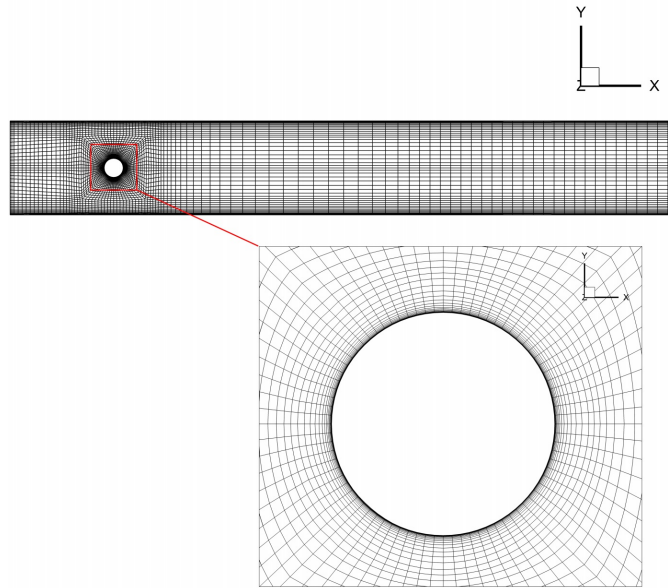
FIGURE 6.2: Grid of the numerical domain with a zoon on the cylinder region..

Aerodynamic solver		
Patch	Variable	Value
Inlet	Velocity	100 m/s
	Pressure	Zero gradient
	TI	5%
Cylinder	Velocity	No slip
	Pressure	Zero gradient
	k, ε	(0,0)
Outlet	All	Zero gradient
Periodic patches	All	Periodicity
Moving mesh solver		
Patch	Variable	Value
Inlet	All displacements	Zero
Oulet	All displacements	Zero
Channel walls	All displacements	Zero
Periodic patches	Z displacement	Zero
Cylinder	All displacements	u = ue

TABLE 6.1: Boundary and initial conditions for aerodynamic and moving mesh solvers.

Fluid phase	
Density	1.225 kg/m^3
Dynamic	viscosity 18.27 μPa s
Particles	
Particle material	Coal ash
Particle density	2000 kg/m^3
Particle diameter	5.0 μm
Cloud number	6 (per step)
Cloud initial size	0.8 m
Number of particles per cloud	50 M
Cylinder material	Stainless steel
Cylinder density	7600 kg/m^3

TABLE 6.2: Properties of fluid and particles.
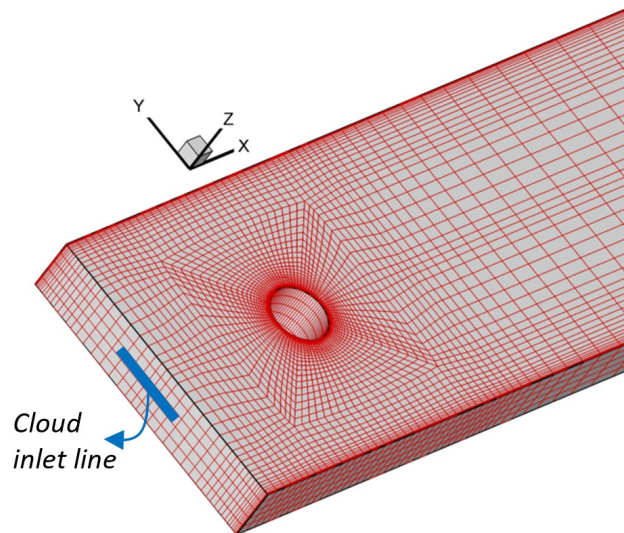
FIGURE 6.3: Cloud inlet line (blue line)..

6.2   Results and discussion

The surface of the eroded cylinder at different steps of the simulation is reported in Figure 6.4. The cylinder surface was opened and reported on a 3D diagram: z axis refers to the z direction of the numerical domain (Figure 6.3); θ is the angular position (in radiant) on the cylinder surface, being 0 the stagnation line; the third axis represent the cylinder radius and it is normalised with the diameter, thus the non-eroded cylinder radius is equal to 0.5 in these figures. As shown in the figures, at the first step the more erosive clouds are the two closer to the stagnation line, as expected. They produce a slightly asymmetrical erosion pattern on the cylinder surface, due to the non-perfectly symmetric starting positions of the clouds. This,

of course, affects the flow dynamics close to the cylinder and the motion of the successive clouds. Indeed, starting from step 2 the erosion patterns become more asymmetrical. The difference in erosion pattern at different steps is summed up by Figure 6.5. It represents the partial erosion patterns on the cylinder surface at step 0 (Figure 6.5 left) and step 6 (Figure 6.5 right): the loss of symmetry is evident. Cloud trajectories at different steps are reported in Figure 6.7. As shown, the differences are not very pronounced however, since even a small difference in the impact angle may provoke a relevant difference in erosion rate, they are enough to affect the erosion behaviour of the particles. The erosion peak in each step is equal to 2.5 mm as set in the MaSAI interface, which means about 16 months in actual time. It is worth remembering that the actual simulated time, depends on the number of clouds, the number of particles per cloud, the flow velocity, and the material properties of both the particle and the target material.
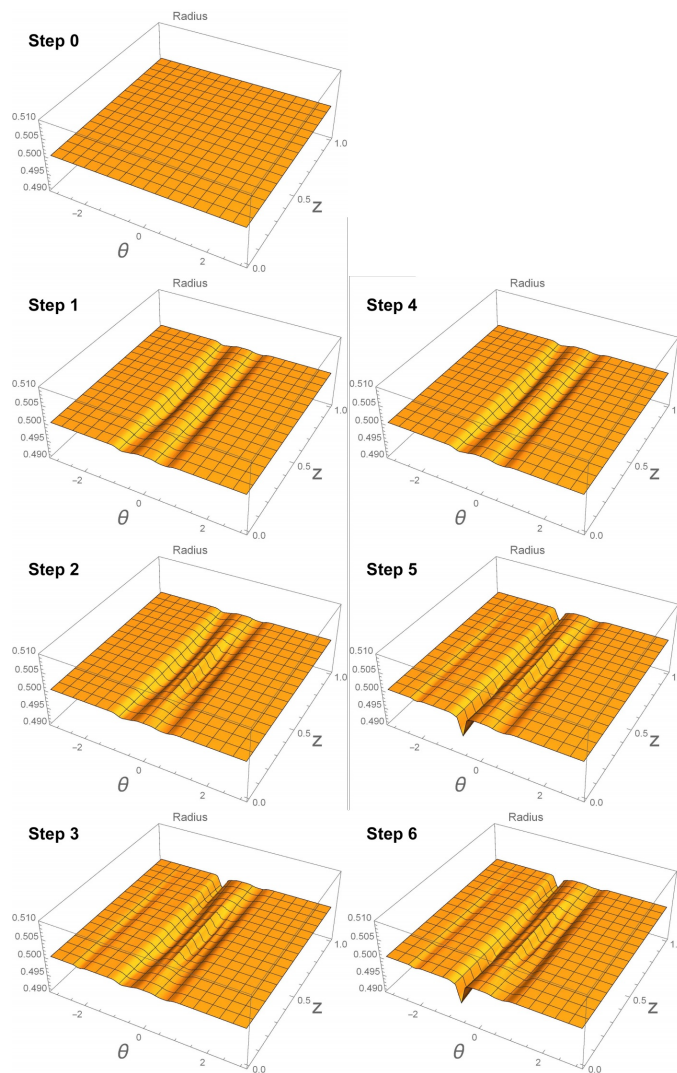

FIGURE 6.4: Erosion evolution (normalized dimensions), steps 0-6; θ=0 stagnation line.
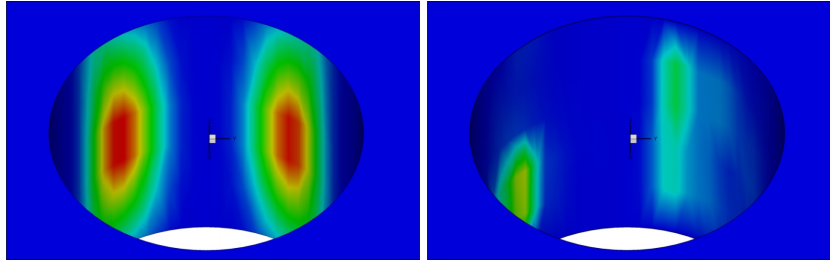
FIGURE 6.5: Normalized erosion patterns: step 0 left, step 6 right
(Blue: no erosion, 0; red: 1).
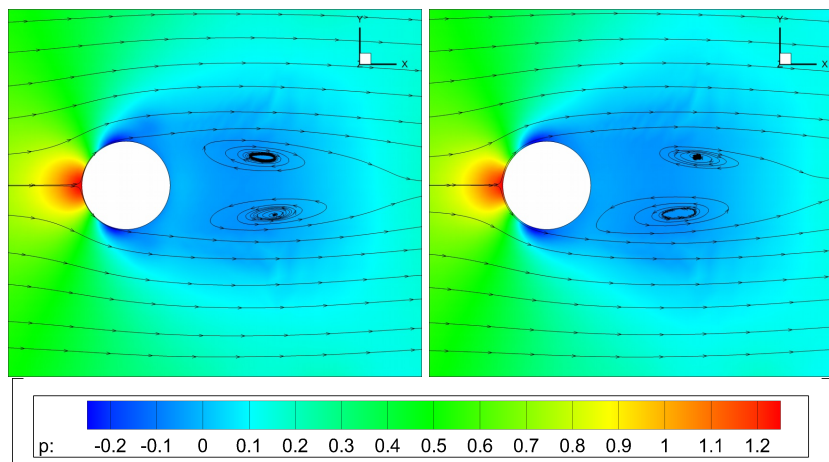
FIGURE 6.6: Pressure field and streamlines from the first (left)
and last (right) iteration.

Figure 6.6 shows a comparison between the aerodynamic field developed with the original geometry (left) and after the erosion (right). Here two very interesting and important aspects come out. First, the aerodynamic field, and in particular the pressure field, changes its shape even for a small amount of erosion. The main motivation is not related to the magnitude of the eroded material but to the shape that the erosion has. Indeed, the non-symmetry in the erosion shape plays the main role in the change of aerodynamic field, which appears, as evident from the wake streamlines, to follow the same non-symmetry.

The second consideration is automatically related to this coupling between erosion of geometry and aerodynamic field, pointing the attention on the importance of the coupling between these two aspects in order to obtain a consistent solution. As we can see from Figure 6.5, the non-symmetry of the aerodynamic field is reflected by the distribution of erosion magnitude. In particular, we can point out that as we obtain a first non-symmetry of the erosion, this will be totally non-symmetric toward all the iterations. This behaviour is due to the fact that the mutual interaction between the erosion and the resultant aerodynamic field as an amplificatory role for the geometric non-symmetries. By looking at the distribution of the pressure coefficient, it is possible to see a general reduction of its value in the rear part of our

sample with respect the initial field. This is because the eroded surfaces generally produce a higher reduction of the pressure coefficient. Indeed, since the erosion is higher in the lower part, we obtain in this part a higher reduction of the pressure coefficient starting from the first iteration.
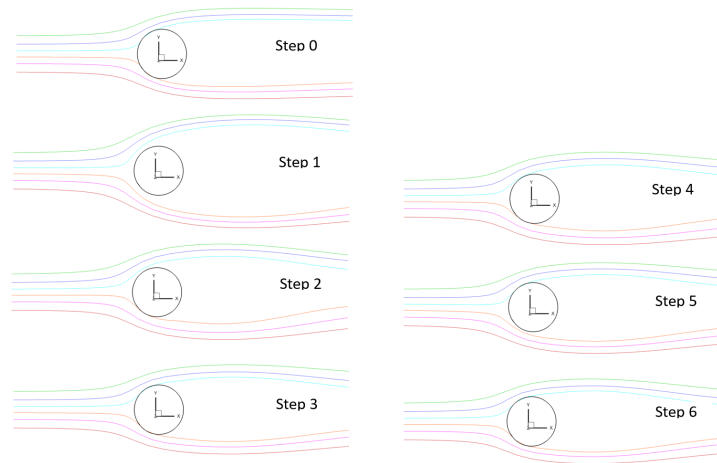
FIGURE 6.7: Cloud center trajectories evolution, steps 0-6.

6.3 Conclusions

In the present study, a new approach to simulate the time evolution of erosion on a target body is presented. In this approach the effect of the change of the body geometry due to the erosion is accounted for, and it affects both the flow and particle cloud dynamics still keeping them one-way coupled, as in the great majority of the turbomachinery applications.

This approach shows a big potential for those applications where a long-time simulation is important but is not possible with the classical numerical techniques. In particular, in all those applications, the interactions between the erosion and the change in the aerodynamic field due to the change of geometry have to be kept in consideration. As we reported in the previous paragraph, the coupling of these phenomena has an amplificatory role for the non-symmetries of all the physic quantities.

Chapter 7

Prediction and study of rain erosion on wind turbine blade with FEM-PCT

This section reports the update of the work [114], then published in [113].

Wind turbines at high latitudes or offshore are subjected to heavy rain. In large horizontal-axis wind turbines (HAWT), at normal operating conditions, the blade-tip velocity range is 90–110 m/s, resulting in rain-driven erosion that influences the turbine performance. Field studies [23, 121] show that the maximum power for a turbine with deeply eroded blades could be reduced as much as 20% of the rated nominal power. Wood [122] and 3M [121] reported that, in severe climates, serious damage to the blade leading edge can be seen within two years of operation. These findings indicate the significant role erosion could play in the wind-turbine maintenance scheduling and even in the early stages of the wind-turbine design.

As in any turbomachinery erosion analysis, the dynamics of the dispersed phase carried by the flow is determined by the inertia and drift velocity of the particles. The physical and chemical properties of both the particles and the target surface play a role in the erosion process. Therefore accurate representation of the particle-laden flow is essential in reliable computational turbomachinery analysis and design, and that needs to be complemented with case-specific erosion models [9].

In 1970s, several researchers, motivated by in-service erosion in aero-engines, started developing methods for computing the particle trajectories and related erosion in gas turbine components. For example, Tabakoff and coworkers [123, 124, 125] carried out particle-trajectory computations in axial and centrifugal turbomachinery, substantiating the interaction between the particle dynamics and the inertial forces in rotating cascades. Later computational studies [126, 127] focused on various modeling aspects of sand erosion. In particle-laden flows, Corsini et al. [128] pointed out turbulence–particle closure modeling as one of the main computational challenges. In wind-turbine erosion, most work reported focused on maintenance and technology issues related to protective coatings [129, 23, 130, 131, 132, 133, 134, 121]. While rain erosion in wings has been studied systematically in dedicated experimental test facilities [135, 130, 136], for wind turbines the

experiments have been performed on blade specimens rather than the entire blade [129, 23].

In this application, we present a method for computational analysis of rain erosion in wind-turbine blades, which is modeled as a special case of particle-laden flows in turbomachinery. The focus here is on the turbulence–particle interaction and erosion in a HAWT, which has a rated power of 6 MW [114]. The equations are solved in the rotating reference frame of the turbine rotor. Consequently, the computations are based on the version of Eq. (3.10) that includes the noninertial terms, and in the implementation of the stabilized formulations these terms are just added to the other source terms. The linear solver uses 5 outer and 5 inner GM-RES iterations, with SOR preconditioning. For more sophisticated preconditioning techniques designed for incompressible-flow computations with the SUPG/PSPG method, see [137, 138, 139, 140, 141].

7.1 Description of the wind turbine

In this study, we design and use a blade for a 6MW, 3-blade HAWT rotor. The main characteristics of the rotor are given in Table 7.1. Table 7.2 provides the airfoil cross-sections used in the chord and twist design, which is based on the Blade Element Momentum (BEM) theory with tip and root loss correction factors [142]. Specifically, we use the same airfoils as those in the 5MW NREL [81] wind turbine.

Rated wind speed (m/s)	12
Design rated power (kW)	6,000
Rotor radius (m)	61
Number of blades	3
Rated rotor speed (rpm)	15
Nominal TSR	8
Hub radius (m)	3

TABLE 7.1: Rotor characteristics, where "TSR" is the tip-speed ratio

Radial position (m)	Airfoil
10.0	DU 99-W-405
17.5	DU 99-W-350
22.5	DU 97-W-300
29.0	DU 91-W2-250
37.0	DU 93-W-210
46.0–60.0	NACA 64-618

TABLE 7.2: Airfoil cross-sections of the blade
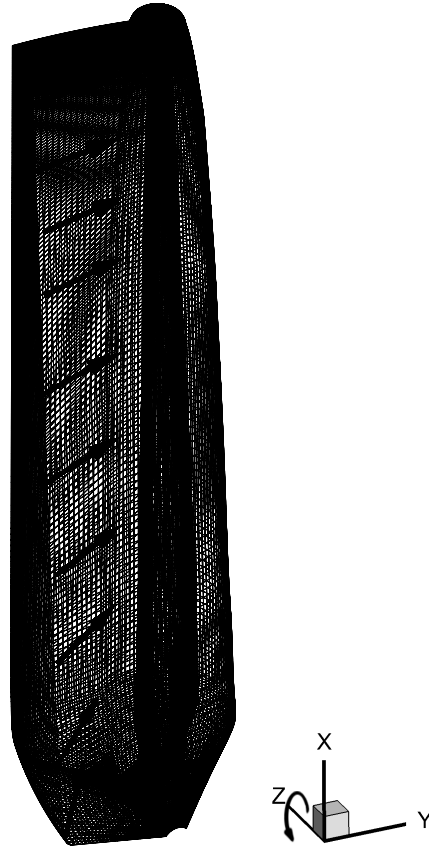
FIGURE 7.1: Mesh for the PCT computation. The arrows represent the cloud initial velocities

In the flow computation the mesh is unstructured, with 4.76 million nodes, 4.24 million hexahedral elements, 2.28 million tetrahedral elements, and 0.09 million pyramid elements. The mesh is structured in the PCT computation, with 1.24 million nodes and 1.20 million hexahedral elements. The PCT domain surrounding the blade extends 3 mean chords from the leading-edge side, and 2 mean chords from the other sides. This domain size for the PCT computation is sufficient in using a large-enough portion of the already computed flow field around the blade. Globally, 50 million droplets, each having a 2 mm diameter, enter the domain in 10 identical clouds (see Figure 7.1). Each cloud has an initial radius of 7.5 m, with the initial positions arranged in such a way that we have a uniform raindrop distribution along the blade. The initial velocity of each cloud is equal to the flow velocity at the cloud center. Droplet and target-material properties are given in Table 7.3.

7.2 Results

7.2.1 Comparison to BEM computation

We first compare, at the nominal operating point, the result from the SUPG/PSPG computation to data from a standard BEM computation with NREL FAST[1]. Table 7.4 shows the out-of-plane force and torque acting on the blade, obtained from

the SUPG/PSPG and BEM computations.

The difference between the torques predicted is less than 3%, and the difference between the out-of-plane forces is even less.

Table 7.5 shows, for the SUPG/PSPG computation, the components of the forces and moments acting on a single blade, together with the rotor thrust and power output.

Water density (kg/m^3)	1,000
Droplet diameter (mm)	2
Compressional wave speed in water (m/s)	1,490
Density of target material (kg/m^3)	1,150
Fracture toughness of target material (MPa m$^{1/2}$)	1.0
Young's modulus of target material (GPa)	3.32
Poisson's ratio of target material	0.38

TABLE 7.3: Droplet and target-material properties

	SUPG/PSPG	BEM
Out-of-plane force (kN)	280	278
Torque (kN m)	1,282	1,316

TABLE 7.4: Out-of-plane force and torque acting on a single blade, obtained from the SUPG/PSPG and BEM computations

	X	Y	Z
Pressure forces (kN)	4.3	-39.7	279.9
Pressure moments (kN m)	-38.8	-11,069.4	-1,355.4
Viscous forces (kN)	0.1	1.9	0.4
Viscous moments (kN m)	-0.4	-11.9	73.7
Rotor thrust (kN)			840.9
Rotor power output (kW)			6,039.9

TABLE 7.5: Components of the forces and moments acting on a single blade, together with the rotor thrust and power output, obtained from the SUPG/PSPG computation

7.2.2 Erosion patterns

We portray the erosion patterns in terms of the impact count (n_w) and the damage (D). The impact count depends only on the cloud dynamics. The damage depends on the number of particles impacting, raindrop impact velocity, and the mechanical properties of the blade surface. In reporting n_w and D, we normalize them by their maximum values on the blade surface.

Figures 7.2 and 7.3 show the impact count and damage distributions.
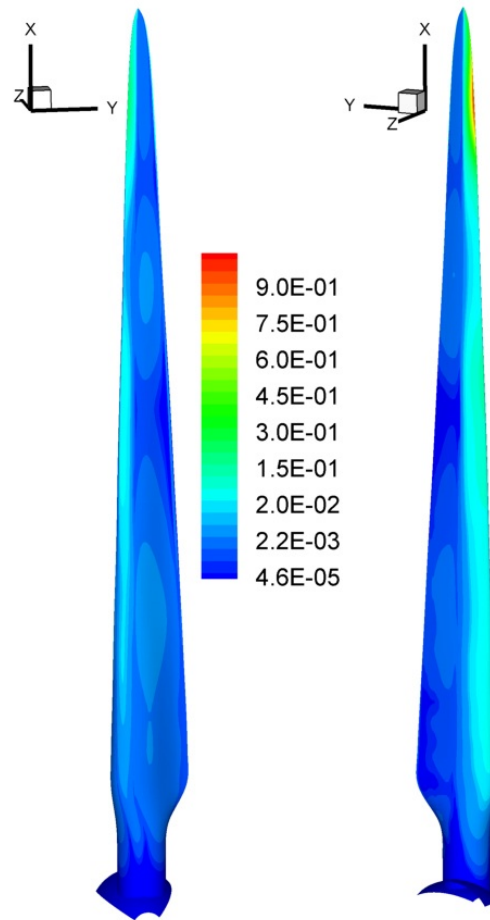
FIGURE 7.2: Normalized impact count. Pressure side (left) and
suction side (right)

The comparison of the two distributions reveals the features of the rain-induced erosion process. First, there is a clear coincidence between the peak impact count core and the corresponding damage, as can be seen at the blade tip and in the blade leading-edge regions above mid-span. This is related to the kinematics of the impact, i.e., the magnitude of the blade tip velocity and the impact angle along the leading edge. Second, the distributions from mid-span inward indicate that below a certain blade velocity, the damage no longer correlates with the impact count. Third, the blade rotation effects are evident, again from mid-span inward, in the amplification of the damage on the blade pressure side.

Figures 7.4 and 7.5 show the impact count and damage at different sections along the blade span, as a function of the distance from the leading edge.

Figure 7.4 confirms that the most critical blade area is the leading edge, irrespective of the radial position, due to the concentration of raindrop impacts. The figure also shows a lack of symmetry in the impact count distribution between the suction and pressure sides, partly due to the blade rotation and the local angle of attack. Specifically, from mid-span outward, the ratio of the peaks between the suction and pressure sides is nearly constant at 4. Moving inward, we see clear peaks

on the suction side only.

Figure 7.5 shows that the differences between the suction and pressure sides are even more evident for the damage. The effect of the number of particles impacting, combined with the raindrop impact velocity and the relative flow velocity, results in much larger damage on the suction side compared to the pressure side. The maximum damage is concentrated on the suction side of the leading edge at the tip of the blade, where the flow (and droplet) speed is maximum. These findings match those observed in the actually wind turbines, where the zone most affected is usually the leading edge, in the mid-tip region.
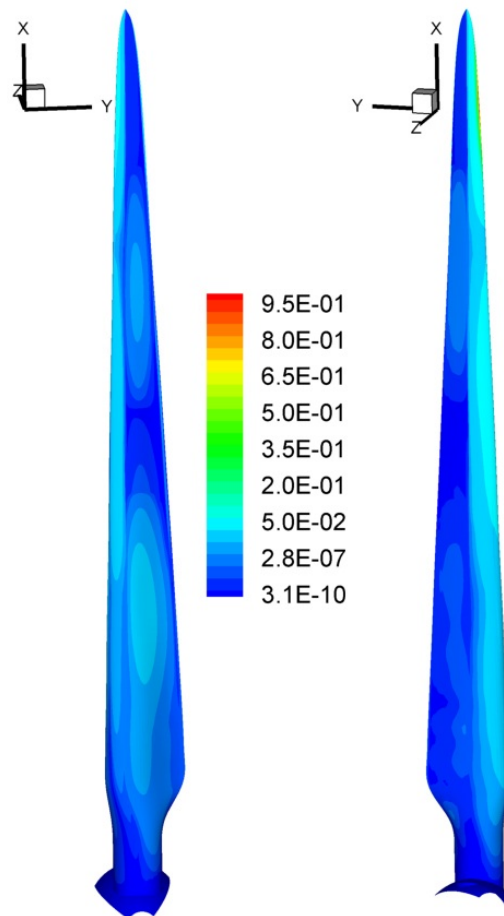
FIGURE 7.3: Normalized damage. Pressure side (left) and suction side (right)
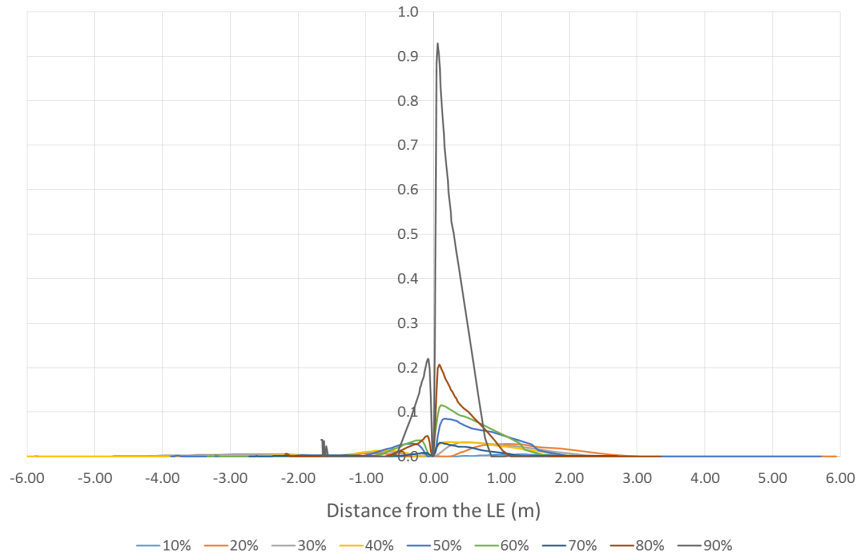
FIGURE 7.4: Normalized impact count at different sections along the blade span, as a function of the distance from the leading edge (LE). The positive and negative distance values are for the suction and pressure sides, respectively
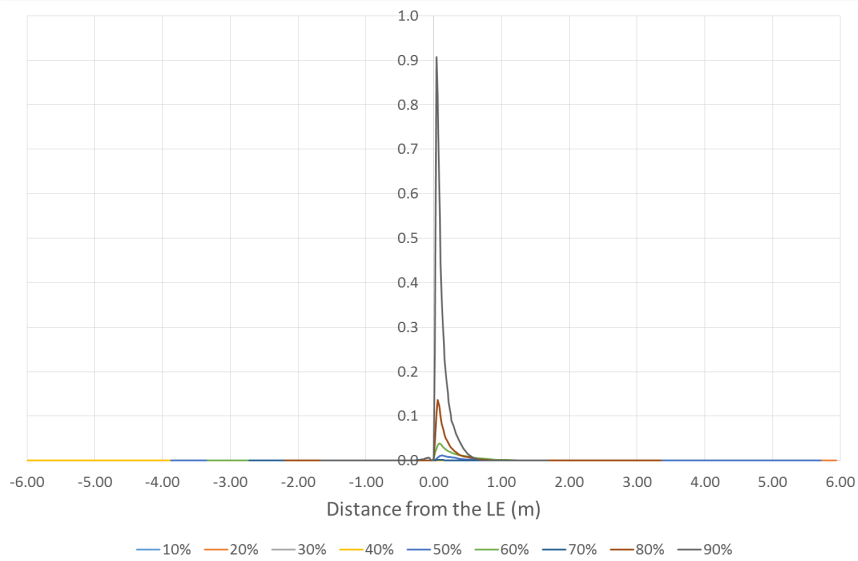
FIGURE 7.5: Normalized damage at different sections along the blade span, as a function of the distance from the leading edge (LE). The positive and negative distance values are for the suction and pressure sides, respectively

7.3 Conclusions

We have presented computational analysis of rain erosion in wind-turbine blades. Such an analysis is important because the rain erosion damage could be significant if the blades are not protected and that could degrade the aerodynamic performance and therefore the power production. The simulation of this phenomenon involves rotating turbulent flows, large number of particles carried by the flow, and turbulence–particle interaction.

On the proposed model of a 6MW HAWT blade, the erosion patterns obtained were in good agreement with those observed in the actual wind turbines.

Chapter 8

Concluding remarks

The aim of this thesis was to present a three-year research work, focused on the development and application of new numerical tools, which are able to simulate complex interaction phenomena involved in the main process of turbomachinery. Starting from a background knowledge of the most used and advanced numerical CAE tools used for the virtual prototyping in industrial production and design engineering; we found actual and interesting challenges in studying the fluid-structure interaction and the erosion of wearing material due to particle-laden flow.

To simulate both of the phenomena implies to find suitable and high fidelity models, keeping into account that the computational cost should be as low as possible.

We chose to use *URANS* models for the aerodynamics. These models produce good results in terms of surface forces and mean velocity profile, with the possibility to simulate also separated flows. The use of an *Arbitrary Lagrange-Eulerian* formulation for the aerodynamic solution allowed to move the domain following the deformation (even large) of the structure given by a three-dimensional geometrically non-linear elastic model.

RANSE models give also a statistical averaged description of the turbulence of the flow, allowing to use the *particle cloud tracking* technique to simulate the particle laden flow erosion on blades material. The simulation of the particle transport in the flow had to be coupled with erosion models to evaluate the mass and portion of wearing material eroded by the flow. Following the common practice in the state of the art, we found and implemented two empirical models ([8, 9]), as we have studied the rain erosion on composite wind turbine blades, and the coal ash erosion on a metal structure.

All the models presented have been coupled in order to solve the mutual interaction between the different dynamics. The strong coupling FSI algorithm and the erosion interface algorithm put further non-linearity to the final systems, which is added to the non-linear nature of all the equations composing the models.

To obtain stable numerical solution, each non-linearity has been treated with the proper instrument during the discretization procedure. We used the *finite element method* to discretize the equations and obtain the final matrices structures that can be solved with numerical schemes. Stabilized formulation have been used

to treat the convective and pressure terms of the Navier–Stokes equations (*SUPG* and *PSPG*). To stabilize the reactive terms of the turbulence closure model ($k - \varepsilon$ equations) we used the *DRDJ* technique.

Stability of the solution in time is achieved using the *Crank-Nicolson* scheme to produce the integration step of ALE-URANSE, while the *Generalized-α* method is used to stabilize the structure dynamics. For the particle motion the integration scheme adopted is of *predictor/multi-corrector* type.

The non-linearity introduced by the coupling between aerodynamics and structure dynamics is treated solving the non-linear step in a *partial segregated* and *iterative* way, achieving the strong coupling through a convergence loop on all the residuals. For the *flow – particle transport – erosion* interface we used a one-way coupling as the time-scales of the different dynamics are different enough to allow this kind of approach. Therefore, in this case it was not necessary to introduce a stabilization technique.

In the second part of the thesis we reports some applications of the developed tools.

The FSI solver has been applied to study a horizontal fan blade in normal operating conditions (Chapter 5), as to evaluate, for an old design done with a structure considered stiff enough to neglect the FSI coupling, the effects of the aeroelasticity. The same solver has been applied also to study the effect of elastic morphing geometries used to control the load and performance for both axial fan and wind turbine blades (Chapter 4). In this case we saw how, for little deformation and in case of active control, this kind of device could improve the section performance of the wind turbine blade. For the fan case, the solution proved that a low-stiffness device (allowing also large deformation) can reduce the load and stabilize the flow in the stall condition, but it has negative effect in the normal operating point as, the same material properties, which guarantees a good response for separating flows, making the device aeroelastically unstable.

Finally, we adapted and applied the erosion interface solver to two upcoming challenges in this field of research. Firstly, we showed the importance of considering the change in geometry (even small) due to erosion during the solution process (Chapter 6). Indeed, we observed on the sample case (cylinder eroded by coal-ash) how the flow distorts as effect for example of a non-symmetric erosion on a symmetric aerodynamic shape. This aspect can become important in the study of the performance and the erosion evolution itself on turbomachinery component subjected to particle-laden flows.

The second application (Chapter 7) focused on the rain erosion of wind turbine blades, confirming a good agreement with field observations in terms of mostly damaged area on the blade surface.

All this numerical tools can represent an important help in the design phase of

new and advanced products. The design process, but also the optimization of the components, can be done considering also effects which are usually neglected, but that are proven to acquire importance in the in-field installed working conditions of the turbomachinery. Studying and producing solutions, which accounts also for these effects in the first design phase, can help to increase the life of the components and to extend a good performance level for more time and more working conditions.

Appendix A

Validation test

A validation test of the FSI-solver was done using the benchmark proposed by Turek et al in [143]. This test consists in a 2D unsteady solution of an incompressible and laminar flow over a fixed cylinder with an elastic bar mounted downstream. Figure A.1 shows the benchmark domain.
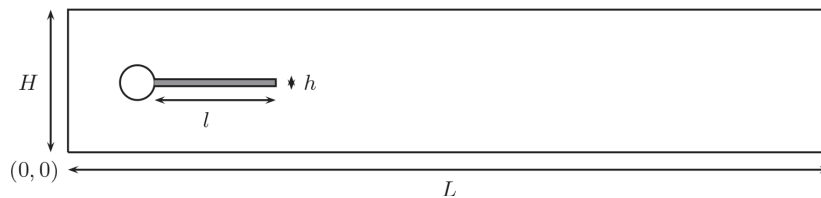
FIGURE A.1: FSI Benchmark domain [143]

Referring to the FSI test 3 [143] we obtain good agreement for the same type of algorithm as reported in Table A.1. After a start-up transient, the system tend to a stable oscillating solution as visible from Figure A.3. In Table A.1 we compare the vertical displacement of the bar tip, the overall lift value and the oscillation frequency. The firsts two quantities are reported in a form that takes into account the oscillatory nature of the solution, i.e. the mean value plus/minus the half amplitude value.
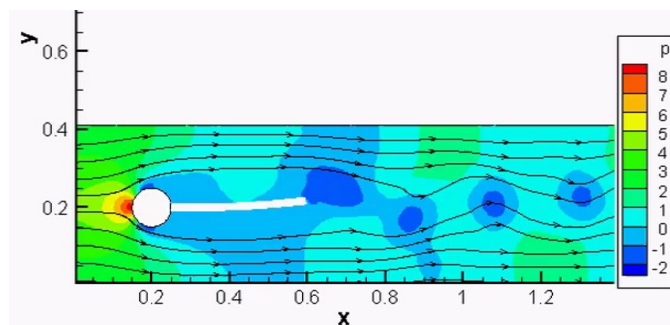
FIGURE A.2: FSI Benchmark solution, pressure field and streamlines
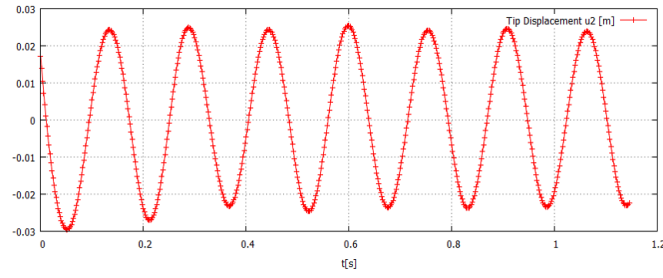
FIGURE A.3: FSI Benchmark solution, tip vertical displacement

	Turek FSI3 [143]	**XENIOS++**
$U2[mm]$	1.5 ± 25.9	1.2 ± 25.5
$Lift[N]$	-0.6 ± 106.0	-1.1 ± 103.1
$f[Hz]$	5.45	5.69

TABLE A.1: FSI benchmark, results comparison.

Bibliography

[1]   FAST user manual: https://nwtc.nrel.gov/FAST8.

[2]   L Morino et al. "Aerodynamics and aeroacoustics of wings and rotors via
      BEM-unsteady, transonic, and viscous effects". In: *Computational mechan-
      ics* 21.4-5 (1998), pp. 265–275.

[3]   T. E. Tezduyar et al. "Modeling of Fluid–Structure Interactions with the
      Space–Time Finite Elements". In: *Flow Simulation with the Finite Element
   Method*. in Japanese. Springer, 2008. Chap. 10, pp. 215–251. ISBN: 978-4-
      431-10033-1.

[4]   T.E. Tezduyar. "Finite element methods for fluid dynamics with moving
      boundaries and interfaces." In: *E. Stein, R. de Borst, and T.J.R. Hughes, ed-
      itors, Encyclopedia of Computational Mechanics, Fluids, chapter 17. Wiley*
      3 (2004).

[5]   Y Bazilevs et al. "3D simulation of wind turbine rotors at full scale. Part
      II: Fluid–structure interaction modeling with composite blades". In: *Inter-
      national Journal for Numerical Methods in Fluids* 65.1-3 (2011), pp. 236–
      253.

[6]   LL Baxter and Philip J Smith. "Turbulent dispersion of particles: the STP
      model". In: *Energy & Fuels* 7.6 (1993), pp. 852–859.

[7]   P Venturini. "Modelling of particle-wall deposition in two-phase gas-solid
      flows". PhD thesis. Sapienza University of Rome, 2008.

[8]   W Tabakoff, R Kotwal, and A Hamed. "Erosion study of different materials
      affected by coal ash particles". In: *Wear* 52.1 (1979), pp. 161–173.

[9]   M. H. Keegan, D. H. Nash, and M. M. Stack. "On erosion issues associated
      with the leading edge of wind turbine blades". In: *Journal of Physics D:
      Applied Physics* 46.38 (2013), p. 383001. URL: http://stacks.iop.
      org/0022-3727/46/i=38/a=383001.

[10] M. H. Keegan, D. H. Nash, and M. M. Stack. "Numerical modelling of
      hailstone impact on the leading edge of a wind turbine blade". In: *EWEA
      Annual Wind Energy Event*. Vienna, Austria, 2013.

[11] Giovanni Fiore, Gustavo EC Fujiwara, and Michael S Selig. "A Damage
      Assessment for Wind Turbine Blades from Heavy Atmospheric Particles".
      In: *53rd AIAA Aerospace Sciences Meeting*. 2015, p. 1495.

[12] Brian Patrick Casaday. "Investigation of Particle Deposition in Internal Cooling Cavities of a Nozzle Guide Vane". PhD thesis. The Ohio State University, 2013.

[13] Alessandro Corsini et al. "Predicting blade leading edge erosion in an axial induced draft fan". In: *Journal of Engineering for Gas Turbines and Power* 134.4 (2012), p. 042601.

[14] Björn Hübner, Elmar Walhorn, and Dieter Dinkler. "A monolithic approach to fluid–structure interaction using space–time finite elements". In: *Computer methods in applied mechanics and engineering* 193.23 (2004), pp. 2087–2104.

[15] Tayfun E Tezduyar et al. "Space–time finite element techniques for computation of fluid–structure interactions". In: *Computer methods in applied mechanics and engineering* 195.17 (2006), pp. 2002–2027.

[16] Elmar Walhorn et al. "Fluid–structure coupling within a monolithic model involving free surface flows". In: *Computers & structures* 83.25 (2005), pp. 2100–2111.

[17] Charbel Farhat and Michael Lesoinne. "Two efficient staggered algorithms for the serial and parallel solution of three-dimensional nonlinear transient aeroelastic problems". In: *Computer methods in applied mechanics and engineering* 182.3 (2000), pp. 499–515.

[18] Farid Abed-Meraim et al. "Multiphysics Simulation Environments for Shell and Spatial Structures". In: (2008).

[19] Joris Degroote, Klaus-Jürgen Bathe, and Jan Vierendeels. "Performance of a new partitioned procedure versus a monolithic procedure in fluid–structure interaction". In: *Computers & Structures* 87.11 (2009), pp. 793–801.

[20] George S Springer, Cheng-I Yang, and Poul S Larsen. "Analysis of rain erosion of coated materials". In: *Journal of Composite Materials* 8.3 (1974), pp. 229–252.

[21] Carolyn Westmark and G Wm Lawless. "A discussion of rain erosion testing at the United States Air Force rain erosion test facility". In: *Wear* 186 (1995), pp. 384–387.

[22] Thanasis K Barlas and GAM Van Kuik. "Review of state of the art in smart rotor control research for wind turbines". In: *Progress in Aerospace Sciences* 46.1 (2010), pp. 1–27.

[23] S. Powell. *3M Wind blade protection coating*. Industrial Marketing Presentation W4600. 3M, 2011.

[24] K. Hanjalic et al. *Analysis and Modelling of Physical Transport Phenomena*. Delft. 2008.

[25] J. Boussinesq. *Essai sur la theorie des eaux courantes*. Memoires presentes par divers savants a l'Academie des Sciences 23 (1): 1-680. 1877.

[26] B.E. Launder and B.I. Sharma. "Application of the Energy-Dissipation Model of Turbulence to the Calculation of Flow Near a Spinning Disc." In: *Letters in Heat and Mass Transfer* 1 (1974), pp. 131–138.

[27] E. Dick and J. Steelant. "Coupled solution of the steady compressible Navier-Stokes equations and the turbulence equations with a multigrid method". In: *Applied Numerical Mathematics* 23 (1997), pp. 49–61.

[28] D. J. Mavriplis and L. Martinelli. "Multigrid solution of compressible turbulent flow on unstructured meshes using a two-equation model". In: *International Journal for Numerical Methods in Fluids* 18.10 (1994), pp. 887–914. ISSN: 1097-0363. DOI: 10.1002/fld.1650181002. URL: http://dx.doi.org/10.1002/fld.1650181002.

[29] V. C. Patel, W. Rodi, and G. Scheuerer. "Turbulence models for near-wall and low Reynolds number flows - A review". In: *AIAA Journal* 23 (1985), pp. 1308–1319. DOI: 10.2514/3.9086.

[30] T. J. R. Hughes, W. K. Liu, and T. K. Zimmermann. "Lagrangian–Eulerian finite element formulation for incompressible viscous flows". In: *Computer Methods in Applied Mechanics and Engineering* 29 (1981), pp. 329–349.

[31] Y. Bazilevs et al. "3D Simulation of Wind Turbine Rotors at Full Scale. Part I: Geometry Modeling and Aerodynamics". In: *International Journal for Numerical Methods in Fluids* 65 (2011), pp. 207–235. DOI: 10.1002/fld.2400.

[32] Ming-Chen Hsu, I. Akkerman, and Y. Bazilevs. "Wind turbine aerodynamics using ALE-VMS: Validation and role of weakly enforced boundary conditions". In: *Computational Mechanics* 50 (2012), pp. 499–511.

[33] Ming-Chen Hsu and Y. Bazilevs. "Fluid–structure interaction modeling of wind turbines: simulating the full machine". In: *Computational Mechanics* 50 (2012), pp. 821–833.

[34] Y. Bazilevs, K. Takizawa, and T. E. Tezduyar. *Computational Fluid–Structure Interaction: Methods and Applications*. Wiley, February 2013. ISBN: 978-0470978771. DOI: 10.1002/9781118483565.

[35] Y. Bazilevs et al. "Aerodynamic and FSI Analysis of Wind Turbines with the ALE-VMS and ST-VMS Methods". In: *Archives of Computational Methods in Engineering* 21 (2014), pp. 359–398. DOI: 10.1007/s11831-014-9119-7.

[36] Y. Bazilevs et al. "FSI modeling of vertical-axis wind turbines". In: *Journal of Applied Mechanics* 81 (2014), p. 081006. DOI: 10.1115/1.4027466.

[37] Y. Bazilevs et al. "Novel structural modeling and mesh moving techniques for advanced FSI simulation of wind turbines". In: *International Journal for Numerical Methods in Engineering* 102 (2015), pp. 766–783. DOI: `10.1002/nme.4738`.

[38] Y. Bazilevs et al. "ALE–VMS Formulation for Stratified Turbulent Incompressible Flows with Applications". In: *Mathematical Models and Methods in Applied Sciences* 25 (2015), pp. 2349–2375. DOI: `10.1142/S0218202515400114`.

[39] Y. Bazilevs et al. "ALE-VMS and ST-VMS Methods for Computer Modeling of Wind-Turbine Rotor Aerodynamics and Fluid–Structure Interaction". In: *Mathematical Models and Methods in Applied Sciences* 22.supp02 (2012), p. 1230002. DOI: `10.1142/S0218202512300025`.

[40] T. J. Hughes. *The finite element method: linear static and dynamic finite element analysis*. Courier Corporation. 2012.

[41] K.Stein, T.E. Tezduyar, and R. Benney. "Automatic mesh update with the solid-extension mesh moving technique. Computer Methods in Applied Mechanics and Engineering." In: *Computer Methods in Applied Mechanics and Engineering* 193 (2004), pp. 2019–2032.

[42] T. Tezduyar et al. "Massively Parallel Finite Element Computation of 3D Flows – Mesh Update Strategies in Computation of Moving Boundaries and Interfaces". In: *Parallel Computational Fluid Dynamics – New Trends and Advances*. Ed. by A. Ecer et al. Elsevier, 1995, pp. 21–30.

[43] S. Lain and M. Sommerfeld. "Turbulence Modulation in Dispersed Two-phase Flow Laden with Solids from a Lagrangian Perspective". In: *International Journal of Heat and Fluid Flow* 24 (2003), pp. 616–625.

[44] M Sommerfeld, B van Wachem, and R Oliemans. *Best practice guidelines. ERCOFTAC Special Interest Group on "Dispersed Turbulent Multi-Phase Flow"*. Tech. rep. Version 20-08-2007, 2008.

[45] Crowe C.T., Troutt T.R., and Chung J.N. "Numerical models for two-phase turbulent flows". In: *Annual Review of Fluid Mechanics* 28.1 (1996), pp. 11–43.

[46] L. L. Baxter. "Turbulent transport of particles". PhD thesis. Brigham Young University, 1989.

[47] L. L. Baxter and P. J. Smith. "Turbulent dispersion of particles: the STP model". In: *Energy and Fuels* 7 (1993), pp. 852–859.

[48] S. K. Kaer. "Numerical investigation of ash deposition in straw-fired furnaces". PhD thesis. Aalborg University, Denmark, 2001.

[49] L. P. Wang. "On the dispersion of heavy particles by turbulent motion". PhD thesis. Washington State University, 1990.

[50]   L. J. Litchford and S. M. Jeng. "Efficient statistical transport model for turbulent particle dispersion in sprays". In: *AIAA Journal* 29 (1991), pp. 1443–1451.

[51]   S. Jain. "Three-dimensional simulation of turbulent particle dispersion". PhD thesis. University of Utah, 1995.

[52]   D. Borello et al. "Prediction of multiphase combustion and ash deposition within a biomass furnace". In: *Applied Energy* 101 (2013), pp. 413–422.

[53]   P. Venturini et al. "Modelling of multiphase combustion and deposit formation and deposit formation in a biomass-fed boiler". In: *Energy* 35 (2010), pp. 3008–3021.

[54]   V. Armenio and V. Fiorotto. "The importance of the forces acting on particles in turbulent flows". In: *Physics of Fluids* 13 (2001), pp. 2437–2440.

[55]   L. Schiller and A. Naumann. "Uber die grundlegenden Berechnungen bei der Schwekraftaubereitung". In: *Zeitschrift des Vereines Deutscher Ingenieure* 77 (1933), pp. 318–320.

[56]   P. J. Smith. *3-D Turbulent particle dispersion submodel development*. Quarterly Progress Report. Department of Energy, Pittsburgh Energy Technology Center, 1991.

[57]   A. G. Evans et al. *Impact damage in brittle materials in the elastic response regime*. Tech. rep. SC5023. Rockwell International Science Centre, 1976.

[58]   G Grant and W Tabakoff. *An experimental investigation of the erosive characteristics of 2024 aluminum alloy*. Tech. rep. DTIC Document, 1973.

[59]   Bruce A Finlayson. *The method of weighted residuals and variational principles*. Vol. 73. SIAM, 2013.

[60]   Filippo Menichini. "Sviluppo di metodi di soluzione segregata per formulazioni variazionali Petrov-Galerkin con programmazione ad oggetti per la predizione di flussi non stazionari nelle turbomacchine". PhD thesis. Sapienza University of Rome, 2008.

[61]   T. E. Tezduyar. "Stabilized Finite Element Formulations for Incompressible Flow Computations". In: *Advances in Applied Mechanics* 28 (1992), pp. 1–44. DOI: 10.1016/S0065-2156(08)70153-4.

[62]   T. J. R. Hughes, L. P. Franca, and M. Balestra. "A New Finite Element Formulation for Computational Fluid Dynamics: V. Circumventing the Babuška–Brezzi Condition: A Stable Petrov–Galerkin Formulation of the Stokes Problem Accommodating Equal-Order Interpolations". In: *Computer Methods in Applied Mechanics and Engineering* 59 (1986), pp. 85–99.

[63] T. E. Tezduyar and Y. J. Park. "Discontinuity Capturing Finite Element Formulations for Nonlinear Convection-Diffusion-Reaction Equations". In: *Computer Methods in Applied Mechanics and Engineering* 59 (1986), pp. 307–325. DOI: 10.1016/0045-7825(86)90003-4.

[64] A Corsini et al. "Improved discontinuity-capturing finite element techniques for reaction effects in turbulence computation". In: *Computational Mechanics* 38.4-5 (2006), pp. 356–364.

[65] T. E. Tezduyar et al. "Incompressible flow computations with stabilized bilinear and linear equal-order-interpolation velocity-pressure elements". In: *Computer Methods in Applied Mechanics and Engineering* 95 (1992), pp. 221–242. DOI: 10.1016/0045-7825(92)90141-6.

[66] F. Rispoli, A. Corsini, and T. E. Tezduyar. "Finite Element Computation of Turbulent Flows with the Discontinuity-Capturing Directional Dissipation (DCDD)". In: *Computers & Fluids* 36 (2007), pp. 121–126. DOI: 10.1016/j.compfluid.2005.07.004.

[67] A. Corsini, F. Rispoli, and A. Santoriello. "A Variational Multiscale high-order finite element formulation for turbomachinery flow computations". In: *Computer Methods in Applied Mechanics and Engineering* 194 (2005), pp. 4797–4823.

[68] A. Corsini et al. "A DRD Finite Element Formulation for Computing Turbulent Reacting Flows in Gas Turbine Combustors". In: *Computational Mechanics* 46 (2010), pp. 159–167. DOI: 10.1007/s00466-009-0441-0.

[69] A. Corsini et al. "Improved Discontinuity-Capturing Finite Element Techniques for Reaction Effects in Turbulence Computation". In: *Computational Mechanics* 38 (2006), pp. 356–364. DOI: 10.1007/s00466-006-0045-x.

[70] A. Corsini et al. "A Multiscale Finite Element Formulation with Discontinuity Capturing for Turbulence Models with Dominant Reactionlike Terms". In: *Journal of Applied Mechanics* 76 (2009), p. 021211. DOI: 10.1115/1.3062967.

[71] A. Corsini, F. Rispoli, and T. E. Tezduyar. "Stabilized Finite Element Computation of NOx Emission in Aero-engine Combustors". In: *International Journal for Numerical Methods in Fluids* 65 (2011), pp. 254–270. DOI: 10.1002/fld.2451.

[72] John Crank and Phyllis Nicolson. "A practical method for numerical evaluation of solutions of partial differential equations of the heat-conduction type". In: *Mathematical Proceedings of the Cambridge Philosophical Society*. Vol. 43. 01. Cambridge Univ Press. 1947, pp. 50–67.

[73]   Olgierd Cecil Zienkiewicz and Robert Leroy Taylor. *The finite element method: solid mechanics*. Vol. 2. Butterworth-heinemann, 2000.

[74]   J. Chung and G. M. Hulbert. "A time integration algorithm for structural dynamics with improved numerical dissipation: The generalized-α method". In: *Journal of Applied Mechanics* 60 (1993), pp. 371–75.

[75]   K. Stein, T. Tezduyar, and R. Benney. "Mesh Moving Techniques for Fluid–Structure Interactions with Large Displacements". In: *Journal of Applied Mechanics* 70 (2003), pp. 58–63. DOI: 10.1115/1.1530635.

[76]   T. E. Tezduyar et al. "Computation of Unsteady Incompressible Flows with the Finite Element Methods – Space–Time Formulations, Iterative Strategies and Massively Parallel Implementations". In: *New Methods in Transient Analysis*. PVP-Vol.246/AMD-Vol.143. New York: ASME, 1992, pp. 7–24.

[77]   A. Corsini et al. "Predicting blade leading edge erosion in an axial induced draft fan". In: *ASME Journal of Engineering for Gas Turbines and Power* 134 (1993).

[78]   Livier Gonzalez. "Morphing wing using shape memory alloy: a concept proposal". In: *Final research paper in* (2005).

[79]   Xavier Lachenal, Stephen Daynes, and Paul M Weaver. "Review of morphing concepts and materials for wind turbine blade applications". In: *Wind Energy* 16.2 (2013), pp. 283–307.

[80]   A Corsini et al. "Numerical study on active and passive trailing edge morphing applied to a multi-MW wind turbine section". In: *International Center for Numerical Methods in Engineering*. 2015.

[81]   J. Jonkman et al. *Definition of a 5-MW Reference Wind Turbine for Off-shore System Development*. Technical Report NREL/TP-500-38060. National Renewable Energy Laboratory, 2009.

[82]   AeroDyn user manual: https://nwtc.nrel.gov/AeroDyn.

[83]   TurbSim user manual: https://nwtc.nrel.gov/TurbSim.

[84]   International Electrotechnical Commission et al. "IEC 61400-1: Wind turbines part 1: Design requirements". In: *International Electrotechnical Commission* (2005).

[85]   HP Monner et al. "Design aspects of the adaptive wing-the elastic trailing edge and the local spoiler bump". In: *Aeronautical Journal* 104.1032 (2000), pp. 89–95.

[86]   Anna-Maria R McGowan et al. *Research activities within NASA's morphing program*. Tech. rep. DTIC Document, 2000.

[87]   Helge Aa Madsen et al. "The potentials of the controllable rubber trailing edge flap (CRTEF)". In: *Proceedings of EWEC*. 2010.

[88] Helge Aagaard Madsen, Anna Candela Garolera, and T Schettler. "Towards an industrial manufactured morphing trailing edge flap system for wind turbines". In: *Proceedings of EWEC*. 2014.

[89] Frank H Gern, Daniel J Inman, and Rakesh K Kapania. "Structural and aeroelastic modeling of general planform wings with morphing airfoils". In: *AIAA journal* 40.4 (2002), pp. 628–637.

[90] Silvestro Barbarino, Farhan Gandhi, and Steven D Webster. "Design of extendable chord sections for morphing helicopter rotor blades". In: *ASME 2010 Conference on Smart Materials, Adaptive Structures and Intelligent Systems*. American Society of Mechanical Engineers. 2010, pp. 323–336.

[91] A Castorrini et al. "Numerical Study on the Passive Control of the Aeroelastic Response in Large Axial Fans". In: *ASME Turbo Expo 2016: Turbomachinery Technical Conference and Exposition*. American Society of Mechanical Engineers. 2016, V001T09A010–V001T09A010.

[92] Domenico Borello et al. "Large-eddy simulation of a tunnel ventilation fan". In: *Journal of Fluids Engineering* 135.7 (2013), p. 071102.

[93] Cheng Xu, Ryoichi Samuel Amano, and Eng Kwong Lee. "Investigation of an axial fan-blade stress and vibration due to aerodynamic pressure field and centrifugal effects". In: *JSME International Journal Series B Fluids and Thermal Engineering* 47.1 (2004), pp. 75–90.

[94] Pieter Groth, Hans MÃĩrtensson, and Clas Andersson. "Design and experimental verification of mistuning of a supersonic turbine blisk". In: *Journal of Turbomachinery* 132.1 (2010), p. 011012.

[95] Yaoguang Zhai, Ronnie Bladh, and Göran Dyverfeldt. "Aeroelastic Stability Assessment of an Industrial Compressor Blade Including Mistuning Effects". In: *Journal of Turbomachinery* 134.6 (2012), p. 060903.

[96] Kwen Hsu and Daniel Hoyniak. "A Fast Influence Coefficient Method for Linearized Flutter and Forced-Response Analysis". In: *49th AIAA Aerospace Sciences Meeting Including the New Horizons Forum and Aerospace Exposition, Orlando, FL, January*. 2011, pp. 4–7.

[97] XQ Huang, L He, and David L Bell. "Experimental and Computational Study of Oscillating Turbine Cascade and Influence of Part-Span Shrouds". In: *Journal of Fluids Engineering* 131.5 (2009), p. 051102.

[98] Mani Sadeghi, Feng Liu, and Feng Liuy. "Investigation of non-linear flutter by a coupled aerodynamics and structural dynamics method". In: (2001).

[99] Volker Carstens and Joachim Belz. "Numerical investigation of nonlinear fluid-structure interaction in vibrating compressor blades". In: *ASME Turbo Expo 2000: Power for Land, Sea, and Air*. American Society of Mechanical Engineers. 2000, V004T03A024–V004T03A024.

[100] Mani Sadeghi and Feng Liu. "Computation of cascade flutter by uncoupled and coupled methods". In: *International Journal of Computational Fluid Dynamics* 19.8 (2005), pp. 559–569.

[101] K. Takizawa and T. E. Tezduyar. "Computational Methods for Parachute Fluid–Structure Interactions". In: *Archives of Computational Methods in Engineering* 19 (2012), pp. 125–169. DOI: 10.1007/s11831-012-9070-4.

[102] Y. Bazilevs et al. "3D simulation of wind turbine rotors at full scale. Part II: Fluid–structure interaction modeling with composite blades." In: *International Journal for Numerical Methods in Fluids, John Wiley & Sons* 65 (2011).

[103] M Sadeghi and Feng Liu. "Coupled fluid-structure simulation for turbomachinery blade rows". In: *AIAA paper* 18 (2005), p. 2005.

[104] S Balachandar and John K Eaton. "Turbulent dispersed multiphase flow". In: *Annual Review of Fluid Mechanics* 42 (2010), pp. 111–133.

[105] M Fathy Hussein and W Tabakoff. "Computation and plotting of solid particle flow in rotating cascades". In: *Computers & Fluids* 2.1 (1974), pp. 1–15.

[106] Awatef A Hamed et al. "Turbine blade surface deterioration by erosion". In: *Journal of Turbomachinery* 127.3 (2005), pp. 445–452.

[107] Awate Hamed et al. "Combined Experimental and numerical simulations of thermal barrier coated turbine blades erosion". In: (2013).

[108] A Ghenaiet. "Numerical simulations of flow and particle dynamics within a centrifugal turbomachine". In: *Compressors and Their Systems* 52 (2005).

[109] Adel Ghenaiet. "Numerical study of sand ingestion through a ventilating system". In: *Proceedings of the World Congress on Engineering*. Vol. 2. Citeseer. 2009, pp. 1–3.

[110] Masaya Suzuki and Makoto Yamamoto. "Numerical Simulation of Sand Erosion Phenomena in a Single-Stage Axial Compressor". In: *Journal of Fluid Science and Technology* 6.1 (2011), pp. 98–113.

[111] Z Mazur et al. "Numerical 3D simulation of the erosion due to solid particle impact in the main stop valve of a steam turbine". In: *Applied Thermal Engineering* 24.13 (2004), pp. 1877–1891.

[112] Reiner Mack, Peter Drtina, and Egon Lang. "Numerical prediction of erosion on guide vanes and in labyrinth seals in hydraulic turbines". In: *Wear* 233 (1999), pp. 685–691.

[113] Alessio Castorrini et al. "Computational analysis of wind-turbine blade rain erosion". In: *Computers & Fluids* 141 (2016), pp. 175–183.

[114] Alessandro Corsini et al. "Modeling of rain drop erosion in a multi-MW wind turbine". In: *ASME Turbo Expo 2015: Turbine Technical Conference and Exposition*. American Society of Mechanical Engineers. 2015, V009T46A001–V009T46A001.

[115] Alessandro Corsini et al. "Numerical simulation of coal fly-ash erosion in an induced draft fan". In: *Journal of Fluids Engineering* 135.8 (2013), p. 081303.

[116] Lucio Cardillo et al. "Predicting the performance of an industrial centrifugal fan incorporating cambered plate impeller blades". In: *Periodica Polytechnica. Engineering. Mechanical Engineering* 58.1 (2014), p. 15.

[117] Domenico Borello et al. "Unsteady cfd analysis of erosion mechanism in the coolant channels of a rotating gas turbine blade". In: *ASME Turbo Expo 2015: Turbine Technical Conference and Exposition*. American Society of Mechanical Engineers. 2015, V05AT11A028–V05AT11A028.

[118] D Anielli et al. "Prediction of particle erosion in the internal cooling channels of a turbine blade". In: *European Conference on Turbomachinery (ETC)*. 2015.

[119] Domenico Borello et al. "Modelling of Particle Transport, Erosion and Deposition in Power Plant Gas Paths". In: *ASME Turbo Expo 2016: Turbomachinery Technical Conference and Exposition*. American Society of Mechanical Engineers. 2016, V009T24A027–V009T24A027.

[120] Ilmar Kleis and Priit Kulu. *Solid particle erosion: occurrence, prediction and control*. Springer Science & Business Media, 2007.

[121] 3M. *A 3M study is the first to show the effects of erosion on wind turbine efficiency*. [Online], www.pressebox.com/pressrelease/3m-deutschland-gmbh/A-3M-Study-Is-the-First-to-Show-the-Effects-of-Erosion-on-Wind-Turbine-Efficiency/boxid/445007. 2011.

[122] K. Wood. *Blade repair: Closing the maintenance gap*. Tech. rep. Composites Technology, 2011.

[123] G. Grant and W. Tabakoff. "Erosion Prediction in Turbomachinery Resulting From Environmental Solid Particles". In: *Journal of Aircraft* 12 (1975), pp. 471–478.

[124] M. F. Hussein and W. Tabakoff. "Computation and Plotting of Solid Particle Flow in Rotating Cascades". In: *Computers and Fluids* 2 (1974), pp. 1–15.

[125] S. Elfeki and W. Tabakoff. "Erosion Study of Radial Flow Compressor With Splitters". In: *Journal of Turbomachinery* 109 (1987), pp. 62–69.

[126] A. Ghenaiet, S. C. Tan, and R. L. Elder. "Experimental Investigation of Axial Fan Erosion and Performance Degradation". In: *Proceedings of the Institution of Mechanical Engineers Part A Journal of Power and Energy*. Vol. 218. 1987, pp. 437–446.

[127] A. Ghenaiet. "Numerical Simulations of Flow and Particle Dynamics Within a Centrifugal Turbomachine". In: *Compressors and Their Systems*. Vol. 218. IMechE Paper No. C639-52. 2005.

[128] A. Corsini et al. "A variational multiscale method for particle-cloud tracking in turbomachinery flows". In: *Computational Mechanics* 54 (2014), pp. 1191–1202. DOI: 10.1007/s00466-014-1050-0.

[129] M. Haag. "Advances in leading edge protection of wind turbine blades". In: *EWEA Annual Wind Energy Event*. Vienna, Austria, 2013.

[130] W. Weigel. *Advanced rotor blade erosion protection system*. Tech. rep. Kaman Aerospace Corporation, 1996.

[131] TGM-Services. *Blade erosion*. [Online]. Available: http://tgmwind.com/bladeerosion.html# bladeerosion. 2011.

[132] Henkel. *Blade maintenance*. [Online]. Available: http://www.henkelna.com/industrial/blade-maintenance-19836.htm. 2013.

[133] Broadwind-Energy. *Blade services*. [Online]. Available: http://www.bwen.com/WindTurbineBladeServices_7777.aspx. 2012.

[134] Ropeworks. *Blade repair and maintenance services*. [Online]. Available: http://www.ropeworks.com/service_wind_blade.htm. 2011.

[135] O. Gohardani. "Impact of erosion testing aspects on current and future flight conditions". In: *Progress in Aerospace Sciences* 47 (2011), pp. 280–303.

[136] University of Dayton Research Institute. *Rain erosion test facility*. [Online]." Available: http://www.udri.udayton.edu/NONSTRUCTURALMATERIALS/COATINGS/Pages/RainErosionTestFacility.aspx. 2013.

[137] M. Manguoglu et al. "A nested iterative scheme for computation of incompressible flows in long domains". In: *Computational Mechanics* 43 (2008), pp. 73–80. DOI: 10.1007/s00466-008-0276-0.

[138] M. Manguoglu et al. "Preconditioning Techniques for Nonsymmetric Linear Systems in the Computation of Incompressible Flows". In: *Journal of Applied Mechanics* 76 (2009), p. 021204. DOI: 10.1115/1.3059576.

[139] M. Manguoglu et al. "Solution of Linear Systems in Arterial Fluid Mechanics Computations with Boundary Layer Mesh Refinement". In: *Computational Mechanics* 46 (2010), pp. 83–89. DOI: 10.1007/s00466-009-0426-z.

[140]   M. Manguoglu et al. "Nested and Parallel Sparse Algorithms for Arterial
        Fluid Mechanics Computations with Boundary Layer Mesh Refinement".
        In: *International Journal for Numerical Methods in Fluids* 65 (2011), pp. 135–
        149. DOI: `10.1002/fld.2415`.

[141]   M. Manguoglu et al. "A parallel sparse algorithm targeting arterial fluid
        mechanics computations". In: *Computational Mechanics* 48 (2011), pp. 377–
        384. DOI: `10.1007/s00466-011-0619-0`.

[142]   H. Glauert. *Windmills and Fans*. Berlin, Germany: Springer, 1935.

[143]   Stefan Turek et al. "Numerical benchmarking of fluid-structure interac-
        tion: A comparison of different discretization and solution approaches".
        In: *Fluid Structure Interaction II*. Springer, 2011, pp. 413–424.